The Earliest Fragmentation in Molecular Clouds

and its connection to Star Formation

by

Rowan Johnston Smith

Submitted for the degree of Doctor of Philosophy in Astrophysics

17th August 2009

University of St Andrews

Declaration

I, Rowan J. Smith, hereby certify that this thesis, which is approximately 30,000 words in length, has been written by me, that it is the record of work carried out by me and that it has not been submitted in any previous application for a higher degree.

Date Signature of candidate

I was admitted as a research student in September 2006 and as a candidate for the degree of PhD in September 2006; the higher study for which this is a record was carried out in the University of St Andrews between 2006 and 2009.

Date Signature of candidate

I hereby certify that the candidate has fulfilled the conditions of the Resolution and Regulations appropriate for the degree of PhD in the University of St Andrews and that the candidate is qualified to submit this thesis in application for that degree.

Date Signature of supervisor

Copyright Agreement

In submitting this thesis to the University of St Andrews we understand that we are giving permission for it to be made available for use in accordance with the regulations of the University Library for the time being in force, subject to any copyright vested in the work not being affected thereby. We also understand that the title and the abstract will be published, and that a copy of the work may be made and supplied to any bona fide library or research worker, that my thesis will be electronically accessible for personal or research use unless exempt by award of an embargo as requested below, and that the library has the right to migrate my thesis into new electronic forms as required to ensure continued access to the thesis. We have obtained any third-party copyright permissions that may be required in order to allow such access and migration, or have requested the appropriate embargo below.

The following is an agreed request by candidate and supervisor regarding the electronic publication of this thesis: Access to Printed copy and electronic publication of thesis through the University of St Andrews.

Date Signature of candidate

Date Signature of supervisor

Abstract

Stars are born from dense cores of gas within molecular clouds. The exact nature of the connection between these gas cores and the stars they form is an important issue in the field of star formation. In this thesis I use numerical simulations of molecular clouds to trace the evolution of cores into stars.

The CLUMPFIND method, commonly used to identify gas structures is tested. I find that the core boundaries it yields are unreliable, but in spite of this, the same profile is universally found for the mass function. To facilitate a more robust definition of a core, a modified clump-find algorithm which uses gravitational potential instead of density is introduced. This allows the earliest fragmentation in a simulated molecular cloud to be identified. The first bound cores have a mass function that closely resembles the stellar IMF, but there is a poor correspondence between individual core masses and the stellar masses formed from them. From this, it is postulated that environmental factors play a significant part in a core's evolution.

This is particularly true for massive stars, as massive cores are prone to further fragmentation. In these simulations, massive stars are formed simultaneously with stellar clusters, and thus the evolution of one can affect the other. In particular, the global collapse of the forming cluster aids accretion by the precursors of the massive stars. By tracing the evolution of the massive stars, I find that most of the material accreted by them comes from diffuse gas, rather than from a well-defined stellar core.

Publications

The following chapters have been published in Monthly Notices of the Royal Astronomical Society.

Chapter 5
'The Structure of Molecular Clouds and the Universality of the Clump Mass Function '
Smith, R. J., Clark, P. C. & Bonnell, I. A, 2008
MNRAS,391,1091-1099

Chapter 6
'Fragmentation in Molecular Clouds and its Connection to the IMF'
Smith, R. J., Clark, P. C. & Bonnell, I. A, 2009
MNRAS, 396, 830-841

Chapter 7
'The Simultaneous Formation of Massive Stars and Stellar Clusters'
Smith, R. J., Longmore, S. & Bonnell, I. A, 2009
submitted

Acknowledgements

My thanks must first go to my supervisor Ian Bonnell whose remarkable enthusiasm and cheerfulness in the face of all obstacles have made this PhD a pleasure. I must also thank my collaborators; Paul Clark who introduced me to CLUMPFIND then helped me pick up the pieces afterwards, and Steven Longmore who helped me connect my simulations to actual observations. I would also like to acknowledge SUPA (The Scottish Universities Physics Alliance), who funded the computer that the simulations presented here were carried out on. A huge thank-you also goes to the staff and students of the St-Andrews Astronomy department who have provided both useful help, and welcome distractions throughout this PhD.

Finally I must thank my family, without whose support and encouragement this would not have been possible. Thanks go to my mother, Joanne, my brother, Lewis, and a particularly large thank-you to my father, Robert, who actually introduced some grammar into this thesis.

Contents

Declaration i

Copyright Agreement iii

Abstract v

Publications vii

Acknowledgements ix

1 Introduction 1

1.1 The Properties of Molecular Clouds . . . 2

1.1.1 Observations . . . 2

1.1.2 Structure and Velocity Distribution . . . 3

1.1.3 Cloud Lifetimes & Magnetic Support . . . 5

1.2 Major Processes in Star Formation . . . 7

1.2.1 Fragmentation & Collapse . . . 7

1.2.2 The Phases of Star Formation . . . 9

1.2.3 The Initial Mass Function . . . 9

1.3 The Clump Mass Function . . . 10

1.3.1 Observations of Cores . . . 10

1.3.2 The Core Mass Function . . . 12

1.4 Outline of Thesis . . . 13

2 Smoothed Particle Hydrodynamics 15

2.1 The SPH Method . . . 16

2.2 The Fluid Equations . . . 18

2.3 The SPH Equations . . . 19

2.3.1 Momentum Equation . . . 19

2.3.2 Equation of State . . . 19
2.3.3 Artificial Viscosity . . . 20
2.3.4 Self Gravity . . . 21
2.3.5 The Energy Equation . . . 22
2.4 Sink Particles . . . 22
2.5 Evolution and Smoothing Lengths . . . 23

3 Initialising Decaying Turbulence 27
3.1 Turbulent Fragmentation . . . 28
3.1.1 Subsonic Incompressible Turbulence . . . 28
3.1.2 Turbulence in Molecular Clouds . . . 29
3.2 Generating a Turbulent Velocity Field . . . 31
3.2.1 Simulation Properties . . . 32
3.2.2 Periodic Boundaries . . . 33
3.2.3 Re-applying the Velocity Field . . . 34
3.2.4 A More Realistic Driving Scheme . . . 37
3.3 Decaying Turbulence . . . 39
3.4 Final Remarks . . . 41

4 Clump Finding 45
4.1 The Clump Finding Technique . . . 46
4.2 2D Clump Finding . . . 47
4.3 3D Clump Finding . . . 49
4.4 Potential Clump Finding . . . 50

5 The Universality of the Clump Mass Function 53
5.1 The Clump Mass Function . . . 54
5.2 The Simulation . . . 55
5.3 Two-dimensional (PP) Clumpfinding . . . 56
5.3.1 Orientation . . . 58
5.3.2 Resolution . . . 59
5.3.3 Density Cut . . . 62
5.4 Position-Position-Velocity (PPV) clumpfinding . . . 66

5.5 Three-dimensional (PPP/SPH) clumpfinding 68
5.6 Discussion of Global Properties 69
5.6.1 The Clumps 69
5.6.2 The Clump Mass Function 70
5.6.3 Universality of the CMF 72
5.7 Conclusions 72

6 The Earliest Fragmentation in Molecular Clouds 75
6.1 Fragmentation and the IMF 75
6.2 The Simulation 78
6.3 Clump Finding using Potential 79
6.4 Physical Properties of the Potential Cores 81
6.4.1 P-core Shapes 82
6.4.2 Masses and Sizes 86
6.4.3 Binding 86
6.4.4 The Core Mass Function with Time 89
6.5 Clump Masses & Stellar Masses 89
6.6 Discussion 96
6.7 Conclusions 100

7 The Simultaneous Formation of Massive Stars and Stellar Clusters 101
7.1 The Formation of Massive Stars 101
7.2 The Simulation 104
7.3 Massive Clump Evolution 105
7.3.1 Time Evolution 105
7.3.2 Observable Properties 113
7.3.3 Direct Comparison to Observations 115
7.4 Discussion 118
7.4.1 Collapse and Accretion 118
7.4.2 Clump-Core Interaction 124
7.4.3 Massive Star Progenitors 127
7.5 Conclusions 128

8 Conclusions **129**

8.1 The Universality of the Clump Mass Function 130

8.2 The Earliest Fragmentation in Molecular Clouds 131

8.3 Massive Stars and Stellar Clusters 132

8.4 Summary 132

Bibliography **136**

List of Figures

1.1 The IMF found by Chabrier (2002). 10

2.1 An illustration of the binary tree. SPH particles are combined hierarchically into nodes which can be substituted for their constituent particles within the gravitational force calculation. 21

3.1 The energy spectrum for a turbulent flow in log-log scales, adapted from a graph from Wilcox (1998) 29

3.2 The velocity dispersion from the centre of the SPH distribution once the velocity field has been applied. The dotted line shows the gradient of the velocity dispersion when $\beta = 0.5$ in equation 1.1. In the range $0.1 < R < 0.5$ pc the Larson relation is satisfied. 33

3.3 The positions of a test particle, originally situated at the co-ordinates $[0.89 : -0.32]$ in a uniform flow from left to right with time. 34

3.4 The decay of turbulent kinetic energy (in units of initial kinetic energy) in the absence of driving and self-gravity. 35

3.5 The column density after the turbulence has decayed for 1 t_{ff}. The colour scale denotes column densities in the range, 0.001 $\mathrm{g\,cm^{-2}}$ *(dark red)* to 0.1 $\mathrm{g\,cm^{-2}}$ *(yellow/white)*. 36

3.6 The PDF of the gas after the turbulence has decayed for 1 t_{ff}. The PDF resembles a lognormal as is expected from turbulence in an isothermal gas. 36

3.7 The PDF of the gas after 1 t_{ff} when the turbulence was continuously reimposed throughout its evolution *(solid line)*. When compared to the PDF from decaying turbulence *(dotted line)* less dense gas had been created. 37

3.8 The column density after 1 t_{ff} when the turbulence was continuously reimposed throughout the evolution. The colour scale denotes column densities in the range, 0.001 $\mathrm{g\,cm^{-2}}$ *(dark red)* to 0.1 $\mathrm{g\,cm^{-2}}$ *(yellow/white)*. 38

3.9 The column density after 1 t_{ff} when the turbulence was driven with the new scheme. The colour scale denotes column densities in the range, 0.001 $\mathrm{g\,cm^{-2}}$ *(dark red)* to 0.1 $\mathrm{g\,cm^{-2}}$ *(yellow/white)*. The density distribution is clumpy and has large scale structure. 39

3.10 The PDF of the gas after 1 t_{ff} when the turbulence was driven with the new scheme *(solid line)*. When compared to the PDF from decaying turbulence *(dotted line)* a greater range of densities have been produced. Note, that N is higher in the driven case merely because this simulation was carried out at higher resolution. 40

3.11 The decay of turbulent kinetic energy (in units of the initial kinetic energy) in a collapsing system *(solid line)*. The energy begins to rise again at 1 t_{ff} compared to the case without self-gravity *(dotted line* when the onset of star formation randomises the velocities. 41

3.12 The velocity dispersion from the centre of the molecular cloud as it collapses. The dispersions are shown at 0.25 t_{ff} *red*, 0.5 t_{ff} *green*,0.75 t_{ff} *blue* and 1 t_{ff} *black*. The dotted line shows the gradient of the velocity dispersion when $\beta = 0.5$ in equation 1.1. The velocity dispersion becomes steeper at larger radii due to collapse motions. 42

3.13 The PDF of the gas after it has collapsed for 1 t_{ff}. The solid line show the simulation which was initially driven, and the dotted line the simulation which has been allowed to decay. 42

4.1 An illustration of the CLUMPFIND algorithm. Four clumps are assigned and they contain material down to the lowest contour. 46

4.2 The use of contours to merge and destroy clumps. 48

4.3 A cartoon of the potential **clump finding** process in 1D. For the potential and contours shown, the blue regions contain material which would be assigned to p-cores. 50

5.1 The column density of the data file used for the clumpfinding comparison. The density scale is logarithmic and runs from 0.005 gcm^{-2} (black) to 1 gcm^{-2} (white). The region shown is 1 pc by 1 pc large and contains 79.5 $M_{\odot}$. 57

5.2 The standard PP clump-find projected in the xy plane, crosses denote the centre of the clumps. This clump-find used data from a 200×200 grid. The scale is shown in parsecs and the colours represent column densities in the range 0.02 gcm^{-2} (blue) to 1 gcm^{-2} (yellow) at logarithmic intervals. 58

5.3 The intrinsic 3D density profile along the z axes of the material belonging to a typical clump in the standard PP clump-find. About half the material assigned to the clump is truly at high 3D densities but the rest is contamination from material along the line of sight. 60

5.4 A clump-find with identical parameters to the standard PP clump-find carried out on the simulated data projected into the xz plane instead of the xy plane. The scale is shown in parsecs and the grayscale represent column densities in the range 0.02 gcm^{-2} (grey) to 1 gcm^{-2} (black) at logarithmic intervals. Crosses show the centre of the clumps 61

5.5 Four clumpfinds carried out on the central region where star formation will occur with varying resolution levels. *Top left* A 50×50 grid with a cell width of $4,125$ AU, *top right* a 100×100 grid with a cell width of $2,063$ AU, *bottom left* a 200×200 grid with a cell width of $1,031$ AU and *bottom right* a 400×400 grid with a cell width of 516 AU. The scale is shown in parsecs and the grayscale represent column densities in the range 0.02 gcm^{-2} (grey) to 1 gcm^{-2} (black) at logarithmic intervals. Crosses show the centre of the clumps. Note that in some cases a clump will disapear at higher resolution, this is primarily due to the shifting contours meaning that some clumps no longer meet the resolution criteria. 63

5.6 The variation of the cumulative number clump mass function with resolution. The clump-finds shown are from the *red* 50×50 grid with a cell width of $4,125$ AU, *green* 100×100 grid with a cell width of $2,063$ AU, the *black* 200×200 grid with a cell width of $1,031$ AU and the *blue* 400×400 grid with a cell width of 516 AU. Error bars depict the uncertainty from Poisson noise. Clumps from each orthogonal projection were included to improve the statistics. 64

5.7 The cumulative number clump mass functions found from PP data with three different lower column density limits; *solid line* 0.01 gcm^{-2}, *dashed line* 0.05 gcm^{-2} and *dotted line* 0.1 gcm^{-2}. Error bars depict the uncertainty from Poisson noise. 65

5.8 Clumpfinds using various data-sets.*Top left* the standard PP clump-find. *Top right* applied to a data set above an intrinsic 3D density of 10^4 cm^{-3}. *Bottom left* using the PPV data-set with 16 velocity bins, corresponding to a velocity resolution of 0.33 kms^{-1}. *Bottom right* the 3D clumpfind on the raw SPH data. The scale is shown in parsecs and the grayscale represent column densities in the range 0.02 gcm^{-2} (grey) to 1 gcm^{-2} (black) at logarithmic intervals. Crosses show the centre of the clumps. 66

5.9 A projection of the real 3D density profile of the clump shown in Fig 5.3 when found using PPV data with 16 velocity bins instead of just PP data. 68

5.10 The cumulative number clump mass functions from the previous clumpfinds. *Top left* the standard PP clump-find, *top right* high density PP data, *bottom left* the PPV clump-find and *bottom right* the PPP (SPH) method. The dashed lines are power law fits whose gradients are shown in Table 5.7. 70

6.1 The simulated Giant Molecular Cloud at one dynamical time. The colours represent column densities in the range 0.001gcm^{-2} (red) to 10 gcm^{-2} (white). Sink particles are shown as white dots and the cloud is viewed along its long axis. 79

6.2 A close up view of some of the pre-stellar pcores identified from Figure 6.1. The top panel shows a zoom of a clustered region in column density and the bottom panel shows the pre-stellar p-cores identified in it. Colours depict column density and the scale runs from 0.001 gcm^{-2} (blue) to 10 gcm^{-2} (yellow). The location of the potential peak of the twenty p-cores in this region are shown by hollow circles. The p-cores are only quasi-spherical and exhibit significant substructure. 83

6.3 The density of the sph particles assigned to a typical p-core plotted radially outward from the peak of gravitational potential. There is considerable dispersion due to substructure, but there is a clear trend showing a flattened central peak and density decreasing outwards. 84

6.4 Histograms of the masses & sizes of the bound (*solid line*) and composite (*dotted line*) p-cores. Panel (a) shows the clump mass function. Masses above 0.2 $M_\odot$ are resolved and the Saltpeter slope is denoted by a dashed line. Panel (b) shows the effective radii. Panel (c) shows the best fit values of n for the profile $\rho \propto r^{-n}$. The p-core mass function resembles the stellar IMF and the p-cores are typically small, centrally concentrated objects. 85

6.5 The binding of the composite p-cores. Panel (a) shows a histogram of the energy ratio of the cores, $E_{rat} \geq 1$ are bound, where $E_{rat} = |E_p|/E_{therm} + E_k$. Panel (b) shows the p-core masses plotted against energy ratio, blue circles denote cores with a steep $n > 1.5$ density profile, green squares intermediate $1 < n < 1.5$ profiles, and red crosses shallow profiles. Panel (c) shows the density exponent n plotted against energy ratio with error bars due to the poor fit from density substructure and non-spherical core shapes; the straight line has a gradient of two. There is no correlation between binding and mass, but there is a link to central concentration. 87

6.6 The one dimensional internal velocity dispersions of the p-cores in the bound(*solid line*) and composite (*dotted line*) datasets. The sound speed of an isothermal gas at 10K is 0.2 kms^{-1} which means the p-cores are generally subsonic 89

6.7 The cumulative mass functions from snapshots at *solid* 0.6 t_{dyn}, *dotted* 0.8 t_{dyn},*short dashed* 1 t_{dyn} and *long dashed* 1.2 t_{dyn}. The dot-dashed line shows the Salpeter slope. The mass function gets steeper with time as the high mass p-cores are formed earlier. 90

6.8 The connection between p-core masses at a snapshot in time and their sink mass when the simulation was stopped. The solid line shows a 1-1 correspondence. There is a poor correlation between p-core mass and the total sink mass formed from them. 91

6.9 The connection between clump mass and sink mass at successive dynamical times. Panel (a) $t_{dyn} = 1$, (b) $t_{dyn} = 2$, (c) $t_{dyn} = 3$, (d) $t_{dyn} = 5$. The solid line shows a 1-1 correspondence. There is now a clear connection between p-core mass and sink mass, but it still shows significant dispersion. 93

6.10 The CMF of the p-cores with mass bins denoted by different colours. 94

6.11 The initial mass functions of the sinks formed from bound cores the colours are the same as their parent p-cores shown in Figure 6.10. The IMF's are recorded at intervals of $1, 2, 3$ & 5 p-core dynamical times. The mass bins get mixed up with time, but the shape of the mass function always resembles the stellar mass function despite the inexact correspondence between core mass and sink mass. . 95

7.1 The evolution of the centre of clump Alpha *top*. The snapshots shown are at *left* 0.75 t_{dyn} (3.53×10^5 yrs), *middle* 1 t_{dyn} ($\sim 4.7 \times 10^5$ yrs) and *right* 1.25 t_{dyn} (5.9×10^5 yrs) respectively. The colour scale denotes column densities from 0.05 $g\,cm^{-2}$ to 5 $g\,cm^{-2}$. The structure becomes more compact with time, and decreases in substructure. 109

7.2 The evolution of the centre of clump Beta *middle*. The snapshots shown are at *left* 0.75 t_{dyn} (3.53×10^5 yrs), *middle* 1 t_{dyn} ($\sim 4.7 \times 10^5$ yrs) and *right* 1.25 t_{dyn} (5.9×10^5 yrs) respectively. The colour scale denotes column densities from 0.05 $g\,cm^{-2}$ to 5 $g\,cm^{-2}$. The structure becomes more compact with time. 110

7.3 The evolution of the centre of clump Gamma *bottom*. The snapshots shown are at *left* 0.75 t_{dyn} (3.53×10^5 yrs), *middle* 1 t_{dyn} ($\sim 4.7 \times 10^5$ yrs) and *right* 1.25 t_{dyn} (5.9×10^5 yrs) respectively. The colour scale denotes column densities from 0.05 $g\,cm^{-2}$ to 5 $g\,cm^{-2}$. The structure becomes more compact with time. 111

7.4 The global properties of the mass within 1 pc of the most massive sink for clumps Alpha *(solid line)*, Beta *(dotted line)* and Gamma *(dashed line)* . *Top*, the total mass and *bottom*, the mass weighted dispersion of matter plotted against the simulation dynamical time ($t_{dyn} \sim 4.7 \times 10^5$ yrs). The clump mass increases with time and becomes more concentrated. 112

7.5 The masses and column densities around the central sink in clumps Alpha *top*, Beta *middle* and Gamma *bottom* plotted against the simulation dynamical time ($t_{dyn} \sim 4.7 \times 10^5$ yrs). The dashed line shows the sink mass and the solid line the column density calculated in a 0.15 pc box centered on the sink. 114

7.6 The dust continuum emission at 230 GHz from clump Alpha at *top* 0.75 t_{dyn} (3.53×10^5 yrs), and *bottom* 1.25 t_{dyn} (5.9×10^5 yrs). The colour scale denotes emission from 0.5 mJy (dark blue) to 500 mJy (yellow). As the clump becomes more evolved the emission from its centre, where the massive stars are forming, increases. 116

7.7 The observable properties of the mass within 1 pc of the most massive sink calculated from a 2D grid with a size resolution of 0.03 pc, plotted against the simulation dynamical time ($t_{dyn} \sim 4.7 \times 10^5$ yrs). The clumps are denoted by the following lines; Alpha *(solid line)*, Beta *(dotted line)* and Gamma *(dashed line)*. The panels show: *top*, the total emission from the clump and *bottom*, the emission weighted dispersion. 117

7.8 Simulated interferometry observations of clump Alpha *top* at the same time intervals as shown in Figure 7.1. 119

7.9 Simulated interferometry observations of clump Beta *middle* at the same time intervals as shown in Figure 7.2. 120

7.10 Simulated interferometry observations of clump Gamma *bottom* at the same time intervals as shown in Figure 7.3. 121

7.11 The connection between clumps and sink masses during accretion. *Top* the growth in sink mass over a period of 0.25 t_{dyn} plotted against the average potential in code units of the mass within a pc radius of the sink. The sinks in the deepest potential well grow the most significantly. *Bottom* the mass in sinks within regions Alpha *solid line*, Beta *dotted line* and Gamma *dashed line* plotted against their dispersion. The mass in sinks grows as the clump becomes more concentrated. 122

7.12 The final fate of the mass within clump Alpha shown at 1 t_{dyn}. The green dots show the positions of gas which will eventually be accreted by the massive sink (red dot). Black dots show the position of sinks and blue dots show the location of material in cores. The gas which will be accreted by the massive sinks is well distributed throughout the clumps, and generally cores within this region will not be disrupted by the massive sink. 125

7.13 *Top* The density distribution of the material which will be accreted by the central sink in clump A (green), compared to that of the material in cores at $t_{dyn} = 1$ (blue). *Bottom* The cumulative density distribution of the entire clump (solid), material which will be accreted by the central sink (long dashed) and material in cores (short dashed). The masses have been normalised to magnitude one, to ease comparison. The material identified in cores contains mainly high density gas, whereas the material which will be accreted by the central sink contains significant amounts of low density gas. 126

List of Tables

1.1 Typical properties of clouds, clumps and cores (adapted from Bergin & Tafalla 2007.) 3

5.1 All the clump-finding presented in this paper were performed on a single SPH simulation. The initial conditions of the simulation are given here. The mass resolution is the minimum mass gravitational forces can be resolved for and is calculated via $M_{res} \sim 100 M_{total}/N_{part}$. The Jeans mass, free-fall time and sound speed are calculated from the average density of the simulation before collapse using the formulae $M_J = (4\pi\rho/3)^{-1/2}(5kT/(2G\mu))^{3/2}$, $t_{ff} = (3\pi/(32G\rho))^{1/2}$. 55

5.2 The parameters used to find the standard PP clumpfind shown in Figure 5.2. The resolutions grid cells correspond to a physical length of 1,031 AU. 59

5.3 The properties of the clumps found in different orientations. The starred case corresponds to the standard PP clump-find. 60

5.4 The recovered clumps at different resolutions for clump-find on PP data in the x-y plane. The * denotes the fiducial case and the resolution is given in grid cells. 62

5.5 The properties of the clumps using the PPV data-set compared to the standard PP clump-find. The 16 velocity bins have a width of 0.33 kms^{-1} and the 40 velocity bins a width of 0.13 kms^{-1} 67

5.6 A comparison of the clump-find results. 69

5.7 The best fit power law gradients for the cumulative CMF's shown in Figure 5.10. 71

6.1 Given below are the initial conditions of the simulation analysed in this paper. The mass resolution is the minimum mass gravitational forces can be resolved for and is calculated via $M_{res} \sim 100 M_{total}/N_{part}$. 78

6.2 The average clump properties of the p-cores in the bound and composite datasets. R_{eff} is the radius within which 68% of the mass is contained. The density profile is the best fit value of n for the profile $\rho \propto r^{-n}$ 84

6.3 A comparison to a small selection of core measurements from the literature. Authors are shown, additional velocities are from * Lada et al. (2008), **Rosolowsky et al. (2008) and show the 1D internal velocity dispersion. Simpson et al. (2008) is a re-analyses of mm observations in Ophiuchus from various published works. Note the p-cores found in this work are defined differently, as they use 3D potential rather than 2D column density. 97

7.1 Typical properties of clouds, clumps and cores (adapted from Bergin & Tafalla 2007.) 102

7.2 The massive clump properties recorded at the beginning (3.53×10^5 yrs) and end (5.9×10^5 yrs) of the analysed period. The first mass M is that found within a 1 pc radius of the central sink. The second is that within a cylindrical column of radius 1pc centered on the same sink. The mean gas density is denoted by $\bar{\rho_g}$, and max. M_s and tot. M_s represent the maximum sink mass within the clump and the total sink mass respectively. 106

7.3 The binding energy of the three clumps at the beginning (3.53×10^5 yrs) and end (5.9×10^5 yrs) of the analysed period. The average radial velocity of the sph gas particles is given by $\bar{v_r}$, where negative values show inward motion. The binding of the clumps is given by E_{rat}=E_p/E_{kin}+E_{therm}, and the absolute magnitude of the potential energy is shown by E_p. For E_{rat2}, the kinetic energy was calculated without including any inward velocities. 106

1

Introduction

Since no energy source is inexhaustible, stars cannot exist forever. Instead they are born in dense nebulae and die in either spectacular supernovae explosions or have a more lingering death as a planetary nebulae. This thesis will concentrate on the earliest stages of the birth of stars: their condensation from their parent nebulae.

Considerable work has gone into understanding star formation since the pioneering work of Jeans (1902), who first derived the criteria for a region of gas to become unstable and collapse to form a star. We now understand that stars are formed in dense nebulae, known as molecular clouds. The gas in the region collapses when it becomes gravitationally unstable and forms a hydrostatic core surrounded by an accretion disk, within which planets may be formed. The material from this disk is accreted by the actual star, which powers energetic jets.

However, there are many facets of this process as which are as yet unknown. The distribution of stars formed has a characteristic profile common to all regions of star formation. There are several explanations proposed which invoke physics such as turbulence, gravity and ther-

modynamics, but a definitive answer has not yet been reached. Moreover, the nature of the link between the dense cores of gas within molecular clouds and the stars which form from them is still unclear. An additional challenge is understanding massive star formation, since the typical fragmentation mass within molecular clouds is an order of magnitude smaller than the largest stars, and feedback from the star could prevent very high masses being reached. At the level of individual stars the mechanism for transferring angular momentum from the disk into the jet is still uncertain.

This thesis seeks to address the connection between the earliest self-gravitating fragments in molecular clouds, and the stars which form from them. Particular emphasis will be placed on the role of gravity in a clustered environment. In this introduction to the topic I will first describe the environment of molecular clouds and how they are observed in Section 1.1. Then in Section 1.2 the major processes in star formation will be outlined. Finally, in Section 1.3 the dense cores which are the progenitors of stars are described, and the similarities between the clump mass function and the stellar initial mass function discussed.

1.1 The Properties of Molecular Clouds

1.1.1 Observations

Since the first observations by Bok of dark nebulae or 'Molecular Clouds', they have been recognised as the birth places of stars (Bok & Reilly, 1947). Due to the very low densities of space (typically less than one atom per cubic centimeter), the self-gravity of gas is largely negligible. It is only in the clouds of gas where large density enhancements are seen that gravity can become a significant enough force to induce collapse. Molecular clouds are predominately situated in the spiral arms of our galaxy, and get their name from the molecular hydrogen which is their chief constituent, although they also contain dust and traces of other molecular species.

Since the discovery of molecular clouds (MC's) considerable effort has gone into determining their properties. This process is complicated by the fact that the main constituent of MC's, (molecular hydrogen) is effectively unobservable at low temperatures, due to its lack of dipole moment. However, several observational methods have been developed which cleverly get around this obstacle. A fruitful approach is to observe dust within MC's rather than the gas, and then convert this using an assumed dust to gas ratio (e.g. Lilley, 1955). Generally

Table 1.1: Typical properties of clouds, clumps and cores (adapted from Bergin & Tafalla 2007.)

	Cloud	Clump	Core
Size (pc)	$2-15$	$0.3-3$	$0.03-0.2$
Mass ($M_\odot$)	10^3-10^4	$50-500$	$0.5-5$
Mean density (cm^{-3})	$50-500$	10^3-10^4	10^4-10^5
Velocity Extent (kms^{-1})	$2-5$	$0.3-3$	$0.1-0.3$
Gas Temperature (K)	~ 10	$10-20$	$8-12$

the mean observed value of 100 is used as the gas to dust ratio, however Lilley (1955) found a range of values between 35 to 250, therefore this assumption is likely to introduce at least some error. The peak in thermal emission from dust particles is situated in the sub-mm regime allowing the dust continuum to be mapped using mm bolometer arrays such as SCUBA and MAMBO (e.g. Motte et al., 1998; Johnstone et al., 2000; Enoch et al., 2006). Another method which uses the dust component is extinction mapping. This takes advantage of the fact that the dust absorbs optical and near-IR light from the background stars. By measuring the colour excess of the background the extinction can be deduced, since short wavelengths will be preferentially absorbed. This is known as the Near Infrared Colour Excess (NICE) method (Lada et al., 1994), and also comes in an improved NICER (NICE Revisited) variant (Lombardi & Alves, 2001).

Alternatively, line emission from one of many trace molecular species can be used to trace the gas. Carbon monoxide and its isotopologues are commonly used tracers of the more diffuse gas (Pineda et al., 2008) but as CO freezes out onto dust grains above densities of 3×10^4 g cm^{-3}, nitrogen bearing molecules such as NH_3 are used to trace the dense regions.

1.1.2 Structure and Velocity Distribution

Molecular Cloud structure appears clumpy and filamentary (Williams et al., 2000), and in many ways its hierarchical structure appears scale free, which has lead some authors to use fractal models to describe it (e.g. Elmegreen, 2002). However, it is more common observationally to split the structure up into 'clouds', 'clumps' and 'cores', which can be defined as shown in Table 7.1 by Williams et al. (2000). These approaches are not incompatible: effectively clumps and cores are equivalent to the high density peaks of a fractal distribution. Unfortunately making these divisions can often be quite arbitrary.

Most of the mass in molecular clouds actually resides at low densities, for example Lombardi et al. (2006) find that only about $\sim 1\%$ of the mass measured from dust extinction in the

Pipe Nebula has $A_k > 10$. Similarly, in continuum emission from Ophiuchus, Johnstone et al. (2004) found that sub-millimetre objects represented only 2.5% of the cloud mass. Indeed, Table 7.1 shows that the range of gas densities seen in Molecular Clouds is extremely wide. Gas densities are well described by a lognormal distribution (e.g. Ridge et al., 2006), which is a characteristic of structure formed by turbulence in an adiabatic gas (Vazquez-Semadeni, 1994; Scalo et al., 1998).

Supersonic linewidths observed from Molecular Clouds have long been interpreted as evidence for said turbulence. These were described by Larson (1981) who related the velocity dispersion $\sigma(v)$ of a cloud to its size L as shown in Equation 1.1

$$\sigma(v) \propto L^{\beta} \tag{1.1}$$

where a value of $\beta \approx 0.4 \pm 0.1$ is typically observed. Larson (1981) developed this relation by analogy to classical subsonic Kolmogorov turbulence, but turbulence in MC's actually has a closer resemblance to Burgers turbulence (Brunt & Mac Low, 2004). Burgers turbulence is supersonic, compressible and most of its energy is dissipated by shocks, which causes large density enhancements. In an isothermal gas the density across a shock increases as the square of the Mach number, and therefore as Mach numbers of up to 10 are observed, density enhancements of at least two orders of magnitude are obtainable. This mechanism could produce the cores discussed above. However, as Ballesteros-Paredes (2004) point out, the majority of structures produced by turbulence should be transient.

Turbulence can also influence the lifetime of molecular clouds. The kinetic energy in turbulence is observed to be roughly equal to the cloud's self-gravity, and so turbulence could provide a supporting force against collapse. However, Mac Low (1999) showed that turbulence decays in about a crossing time in all cases. Therefore, if turbulence is the dominant support in clouds, they must either have a short lifetime, or the turbulence must be continuously driven. At small scales, turbulence cannot entirely prevent collapse, as it becomes subsonic, which increases the likelihood of gravity becoming the dominant force (Goodman et al., 1998).

Thermal motions are rarely a dominant contribution to the energy balance of molecular clouds, due to their extremely low temperatures. The dust and gas temperatures are set by the balance between heating and cooling. The dust is heated by the interstellar radiation field,

and cooled by the emission of thermal energy from the dust grains (Mathis et al., 1983). As the densities of molecular clouds are high, cooling is efficient and temperatures are low ($15-20$ K in the cloud and $10-12$ K in cores, Ward-Thompson et al. 2002). The gas is heated by cosmic rays and cooled by molecular line emission, particularly from CO (McKee et al., 1982). At high densities, such as those seen in cores, CO freezes onto dust grains. However, at these densities the dust and the gas become well thermally coupled due to collisions, which allow the gas to be efficiently cooled by the dust (Larson, 1973b). This allows molecular clouds to maintain a temperature of around 10 K across a wide range of densities (Goldsmith & Langer, 1978). This isothermal behaviour continues until the cloud becomes optically thick to dust emission at $n(H_2) > 10^{10}$ cm^{-3} (Tohline, 1982).

1.1.3 Cloud Lifetimes & Magnetic Support

It is important to know the lifetimes of molecular clouds when studying star formation as this determines whether star formation is a quick or slow process. Two useful timescales in MC's are the free fall time and the sound crossing time.

$$t_{ff} = \left(\frac{3\pi}{32G\rho}\right)^{1/2} \tag{1.2}$$

$$t_{cr} = L/c_s \tag{1.3}$$

The free fall time is defined as the time a uniform gas sphere will take to collapse from rest to an infinite density in the absence of pressure gradients. Typical free fall times for molecular clouds are of the order of 10^5 -10^6 yrs. The sound crossing time is simply the time a sound wave travelling at the sound speed c_s will take to cross the distance, L, across the cloud.

There is considerable debate as to the dynamic state of molecular clouds. Some propose that MC's are long lived equilibrium structures which evolve quasi-statically to form stars (Blitz & Shu, 1980; Tan et al., 2006). Others hold the view that MC's are short lived dynamic structures (Ballesteros-Paredes et al., 1999a; Elmegreen, 2000).

The quasistatic view was originally motivated by the low star formation rate observed in the Galaxy: for example McKee & Williams (1997) find a value of only 4 $M_\odot\ /yr$. This lead to the conclusion that star formation must be an inefficient process which takes place over long time scales. Zuckerman & Evans (1974) used the low galactic star formation rate to show that

only a few percent of the mass in MC's was converted to stars. Molecular clouds, therefore, would need to be supported against gravitational collapse throughout their lifetimes(about 10 Myr). Turbulence decays over a crossing time (Mac Low et al., 1998) so there would need to be some mechanism adding energy to sustain it. Magnetic fields could also stabilise molecular clouds due to conservation of magnetic flux. In a magnetically supported long-lived MC it is proposed that stars would condense slowly out of the surrounding medium (Shu, 1977).

Zeeman splitting can be used to measure the magnitude of the magnetic field, although this requires very high signal-to-noise observations. Using this method Crutcher et al. (1993) found the typical cloud total field strength was $16\mu G$. In a later survey they determined that static fields alone were not sufficient to balance gravity (Crutcher, 1999). However, if a contribution from MHD turbulence was included this could be enough to support the cloud (although as mentioned previously, the turbulence would soon decay). Recently Crutcher et al. (2009) measured the ratio of the mass-to-magnetic flux between four molecular cloud cores and their envelopes. The ratio was less than 1 in all cases. This was too low for them to have formed by magnetic ambipolar diffusion. Observations by Bourke et al. (2001) confirm that observed magnetic fields would be insufficient to support spherical clouds, although they may be able to support flattened sheets. Therefore at present, it is unclear whether magnetic fields are a dominant force in MC's.

In the alternative dynamic scenario, clouds are not in virial equilibrium but simply a rough energy equipartition. Molecular clouds can be thought of as transient features of the turbulent flow in the ISM, with lifetimes of between $3-5$ Myrs (Ballesteros-Paredes et al., 1999a). No additional support is needed, as it is not necessary for the cloud to achieve virial equilibrium. Moreover, if the proposal of Elmegreen (2000) that all star formation occurs within a single crossing time is true, then turbulence need not be driven. Despite this rapid star formation, overall star formation rates remain low in agreement with observations, since only a small fraction of the total GMC mass is actively involved in star formation. Effectively, the short MC lifetimes halt star-formation at low efficiencies.

1.2 Major Processes in Star Formation

1.2.1 Fragmentation & Collapse

The idea of star formation occurring through the gravitational fragmentation of Molecular Cloud structure is an old one. In 1902, Jeans showed that gravity can amplify small perturbations in a uniform medium. Short wavelength perturbations are pressure-dominated and will re-expand due to their internal thermal energy. However beyond some critical wavelength, λ_J, gravity dominates and the density perturbation will grow exponentially. For a uniform isothermal region the Jeans Length is expressed as

$$\lambda_J = \pi^{1/2} c_s (G\rho)^{-1/2}. \tag{1.4}$$

where ρ is the density and the isothermal sound speed, c_s, is given by the expression $c = (kT/m)^{1/2}$ where m is the average particle mass. The Jeans Mass is

$$M_J = \left(\frac{5kT}{2G\mu}\right)^{3/2} \left(\frac{4\pi\rho}{3}\right)^{-1/2}, \tag{1.5}$$

where k is the Boltzman constant, T is temperature, and μ is the mean atomic mass. For a typical molecular cloud with an average density around 10^{-19} g cm^{-3}, the Jeans Mass is of the order of one solar mass. At this point it should be noted that Jeans analysis is in some respects flawed, as he did not take into account the effects of the background material in which the perturbation resides (Binney & Tremaine, 1987). Nonetheless, the Jeans mass remains a valid approximation regardless of geometry (Larson, 2003).

The idealised case of a pressure bounded spherical perturbation in a self-gravitating isothermal medium was independently derived by Bonnor (1956) and Ebert (1955) who found that it would collapse if its mass exceeded,

$$M_{BE} = 2.1 \left(\frac{T}{20\,K}\right)^2 \left(\frac{P/k}{10^6\,Kcm^{-3}}\right)^{-1/2} M_\odot \tag{1.6}$$

where T is the internal temperature and P the boundary pressure, but otherwise it would remain in equilibrium. Bonnor-Ebert spheres are often used as models for the initial core stage of star formation (eg. Johnstone et al., 2000). They have a flat inner density core with density ρ_c, and a decreasing outer density profile which falls as r^{-2}. The size of the inner

core can be expressed in terms ρ_c as

$$r_c = \left(\frac{4\pi G \rho_c}{c_s^2} \right)^{1/2}, \tag{1.7}$$

and this core length can be used as a normalisation length for the entire core, $\xi_e = r_e/r_c$, where r_e is the outer radius of the Bonnor-Ebert sphere. The outer radius, r_e of the sphere is determined from the balance of internal and external pressure. For example, an increase in external pressure will cause the core to shrink and increase the importance of self gravity. However, there exist no equilibrium models above $\xi_e = 6.3$, so all Bonnor-Ebert spheres which exceed this value are unstable and will collapse.

The collapse of isothermal density spheres has been extensively studied by Larson (1969) and Penston (1969), who showed that during the collapse there is runaway growth of a central peak, which leads to the density profile approaching that of an isolated isothermal sphere, $\rho \propto r^{-2}$. As the sphere begins to collapse, there is initially no net pressure support, since the interior and exterior pressures are balanced, and so collapse can proceed freely. However, as the inner densities increase and the outer densities decrease, an outward pressure gradient is generated, which impedes collapse in the outer regions of the sphere. Additionally, as the free fall time increases with density, inner dense radii collapse more rapidly than the less dense radii outside them, which causes the central collapse to accelerate. The centre of the core reaches the densities where a protostar can be formed in advance of the rest of the envelope, so this must be subsequently accreted.

In the Larson-Penston self similarity solution describing the collapse of an isothermal sphere, in-fall velocities are supersonic and initially approach a value of $-3.3c_s$ before the central proto-star is formed. Hunter (1977) extended this model past the formation of the proto-star, and found that it would have a constant accretion rate of $46.9c^3/G$. However, when Hunter (1977) compared the predicted collapse to that shown from numerical simulations, he found that a self-similarity solution was only approached in a small central region, and that the accretion rate would actually decrease rapidly with time. A similar result was found by Foster & Chevalier (1993). Moreover, if the initial density profile of the sphere is flattened at the centre and then decreases outward (as in the case of Bonnor-Ebert spheres or Plummer spheres) this also leads to an initially high accretion rate while the central core is accreted, which then falls as the lower density envelope is accreted (Whitworth & Ward-

Thompson, 2001)

1.2.2 The Phases of Star Formation

The stages of star formation between cores and stars are now very briefly detailed (for a full treatment see Shu et al. 1987 or Andre et al. 2000). In the prestellar stage of star formation a core collapses under gravity until its centre becomes optically thick (Tohline, 1982). A hydrostatic core develops when all the molecules within it have dissociated. This core is the protostar. In the Class 0 phase the protostar accretes mass from the original core envelope, partly through direct in-fall, but mainly through a disk formed by the higher angular momentum material. In addition to accreting gas, the protostar also launches outflows. In the Class I phase, these outflows clear out the envelope along the rotational axis and accretion continues. When the class II phase is reached, the envelope has dispersed and accretion is almost negligible, although a tenuous disk remains. The protostar will now start contracting towards the main sequence. Objects in this phase are called T Tauri stars. In the Class III stage, the protostar has almost reached the main sequence and all that remains is a debris disk (and possibly some planets). In the subsequent simulations presented in this thesis, star formation can only be followed down to the resolution scale, which is typically a few thousand AU (see Section 2).

1.2.3 The Initial Mass Function

The initial mass function (IMF) of stars in our galaxy was first measured by Salpeter (1955) who showed that the number of stars $\xi(m)dm$ which have masses between m and $m + dm$ can be approximately represented by the power law,

$$\xi(m)dm \approx m^{-\alpha}dm \tag{1.8}$$

where $\alpha \approx 2.35$ for stars with mass $0.4 \leq m \leq 10$ $M_{\odot}$. However this approach is slightly simplistic, and a lognormal form has been found to be a more accurate representation (Miller & Scalo, 1979; Chabrier, 2002). The most common approach when modelling the IMF empirically is to use a three component power law, as shown below (Kroupa, 2002).

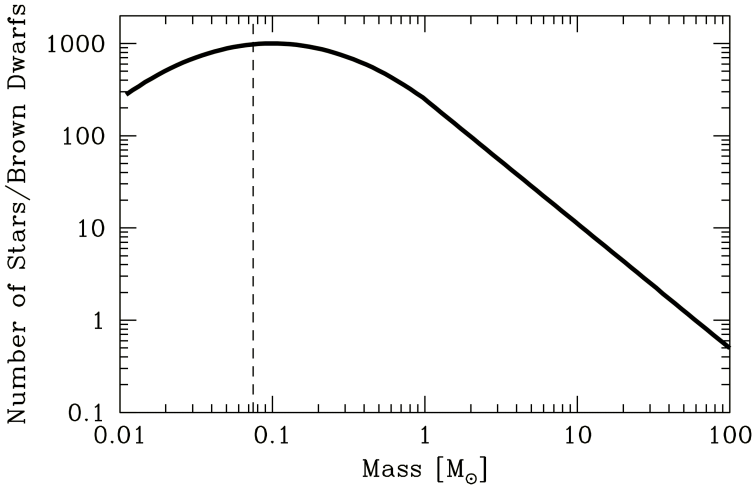

Figure 1.1: The IMF found by Chabrier (2002).

$$\xi(m) = \begin{cases} 0.26m^{-0.3} & 0.01 \leq m < 0.08 \\ 0.035m^{-1.3} & 0.08 \leq m < 0.5 \\ 0.019m^{-2.3} & 0.5 \leq m < \infty \end{cases} \tag{1.9}$$

The basic shape of the IMF is shown in Figure 1.1 in a log scale (note, that in this form the exponents of Eq. 1.9 become 0.3, -0.3 and -1.3 respectively.) The IMF appears to be common to all regions of star-formation, and therefore its shape must be explained by any theory involving the statistics of star formation.

1.3 The Clump Mass Function

So far in this Introduction we have considered the physics of molecular clouds and star formation. The dense cores of gas seen in molecular clouds are the link between these two topics. Cores represent the densest peaks of the hierarchical density distribution within molecular clouds, and it is within them that stars are formed. Further, observations of the core mass function have shown it strongly resembles the IMF (Motte et al., 1998), leading many to propose a direct link between them (eg. Alves et al., 2007). Firstly let us consider the properties of the cores:-

1.3.1 Observations of Cores

As the sites of star formation, cores have been studied in great detail; recent surveys include Motte et al. (1998); Johnstone et al. (2000, 2006); Ikeda et al. (2007); Alves et al. (2007);

Nutter & Ward-Thompson (2007); Ward-Thompson et al. (2007); Enoch et al. (2008). From these an understanding of the key features of cores is beginning to develop.

Cores are generally sub-classified into two types. Cores containing stars already have an infrared source at their centre, meaning they are actively forming proto-stars, and so are often referred to as proto-stellar cores. Star-less cores show no evidence of a proto-star at their centre and are usually referred to as pre-stellar cores.

As regards the structure of cores, Ward-Thompson et al. (1994) found that while the densities of the outer regions of cores can be well fit by the power law $\rho \propto r^{-2}$, the profile is flattened at the centre. This resembles the density profile of a Bonor-Ebert sphere which was discussed in Section 1.2.1. Observations of pre-stellar cores are generally well fit by this model (e.g. Johnstone et al., 2000). Bonnor-Ebert spheres are hydrostatic and pressure confined, so does this mean that cores also share these properties?

Lada et al. (2008) make the case that the core population of the Pipe Nebula could be pressure confined. However this may not always be the case, as Tafalla et al. (2004) have observed cores within which the thermal pressure is insufficient to balance self-gravity. More worryingly, Ballesteros-Paredes et al. (2003) have shown that dynamically collapsing cores can be well fit by stable Bonnor-Ebert spheres, therefore the usefulness of this method in determining the evolutionary state of cores is as yet uncertain. Moreover, even the simple assumption of sphericity is not entirely valid. Myers et al. (1991) found cores to be elongated structures better represented as prolate or oblate spheroids, as a consequence of which their internal energy equilibrium must be imperfect.

Pre-stellar cores have temperatures of around 10K, similar to their parent molecular clouds. Temperatures will only rise above this if the core becomes unstable and begins to collapse. When densities become so high that the gas is opaque to its own cooling radiation the core will be heated. Larson (2005) proposed a simple polytropic heating and cooling law to model gas temperatures during the early stages of star formation. This will be discussed further in Chapter 2.

Unlike the velocities of the larger cloud, core velocities are generally close to thermal (Myers, 1983; Goodman et al., 1998). These largely sonic motions seem chiefly due to turbulence, as the contribution from rotation seems small (Goodman et al., 1993). Additionally in-fall motions are often observed; for instance Lee et al. (1999) found an overabundance of

inward velocities of $0.05 - 0.1$ kms^{-1} in a sample of 220 starless cores. At least some cores, therefore, must be in a state of dynamic collapse.

1.3.2 The Core Mass Function

Since the seminal observations of Motte et al. (1998) a clear resemblance has been recognised between the core (and clump) mass functions and the stellar initial mass function (IMF). Motte et al. (1998) have shown that the core mass function (CMF) in ρ Oph can be described by a similar power-law fit as the IMF. Above ~ 0.5 M$_\odot$ they find $dn/dm \propto m^{-\alpha}$ is well-fitted by an exponent value of $\alpha = 2.5$, while at lower masses they see a turn-over that can be fitted with $\alpha = 1.5$. These values for α are broadly consistent with the usual fits to the (Kroupa, 2002) IMF shown in Section 1.2. Similar results have been confirmed by a number of authors for a variety of nearby star-forming regions, although the range of core masses found and the break mass of the power law fit can vary (Johnstone et al., 2000, 2006; Nutter & Ward-Thompson, 2007; Alves et al., 2007; Testi & Sargent, 1998). Clumps and cores appear to have slightly different mass functions. Larger clump measurements using CO tend to find a shallower value of the exponent $\alpha = 1.4 - 1.8$ (Blitz, 1993; Kramer et al., 1998). This is perhaps due to gravity steepening the slope on smaller scales where structures are more bound. A more detailed account of the clump/core mass distribution can be found in Ward-Thompson et al. (2007).

There are various theories as to how a power-law CMF could be formed. Gravity, causing successive fragmentation in a collapsing gas cloud will naturally lead to a power law distribution (Larson, 1973a; Elmegreen & Mathieu, 1983). Alternatively, as discussed earlier, supersonic turbulence produces a clumpy, hierarchical density structure, the density peaks of which are cores. Padoan & Nordlund (2002) have argued that a CMF with a power law resembling that of the IMF is a natural consequence of turbulence with a power spectrum consistent with the Larson velocity dispersion law. Recently, Hennebelle & Chabrier (2008) proposed that the CMF is a combination of a power law caused by turbulence, and a lognormal cutoff centered around the characteristic mass of gravitational mass for gravitational collapse. The Jeans mass (Jeans, 1902) at the point of fragmentation has been shown to be only weakly dependent on temperature, density, metallicity and radiation field in the environments in which stars form (Larson, 2005; Elmegreen et al., 2008), which means that the characteristic mass of a Jeans unstable fragment should be similar in all molecular clouds.

The similarity of the CMF and IMF naturally leads to the conclusion that they are linked. However, it is unclear how best to get to the IMF from the clump mass function. Many assume a direct $1-1$ link between the masses (Motte et al., 1998; Padoan & Nordlund, 2002), while others include the effects of multiplicity (Goodwin et al., 2008). Alves et al. (2007) find that an efficiency of one third is needed for there to be a direct correspondence between core masses and stellar system masses in the Pipe nebula. Simpson et al. (2008) find that an efficiency factor of 0.2 would be needed in Ophiuchus to obtain the IMF from the CMF if every core formed a single star. However, when they used the multiplicity model of Goodwin et al. (2008) an efficiency of 0.4 was required.

It is worth noting that there are many complicating factors during core collapse, such as feedback from winds and outflows (Shu et al., 1988; Silk, 1995; Myers, 2008; Dale & Bonnell, 2008), supporting magnetic fields (Heitsch et al., 2001; Tilley & Pudritz, 2007) and competitive accretion (Zinnecker, 1982; Bonnell et al., 1997, 2001). All of these processes may be involved in the collapse of a fragment to a star, and all could vary locally. Additionally, Swift & Williams (2008) have shown that when a core mass function is evolved into a stellar IMF, a Salpeter like distribution was found regardless of whether the core-to-star efficiency was constant, variable or included multiplicity. Clark et al. (2007) have argued that since lower mass cores should have higher densities, they will collapse more rapidly, and hence if there was an exact correspondence between cores and stars, a steeper IMF would be produced than that observed. Hatchell & Fuller (2008) on the other hand, have shown that the fraction of proto-stellar cores increases with mass. They suggest this can be explained if massive cores actually have short evolutionary time-scales and there is continuing accretion onto the core during the evolution.

Moreover, under the competitive accretion theory of star formation there is no need for a direct correlation between core masses and stellar masses at all, since the cores can be thought of as 'seeds' from which accretion will build up the future IMF (Clark & Bonnell, 2005). The evolution of a core mass function into a stellar population will be a major topic of this thesis.

1.4 Outline of Thesis

In Chapter 2 I will review the SPH method which is used to simulate the MC's, and in Chapter 3 I discuss how decaying turbulence has been implemented. Clump-finding algorithms are

discussed in Chapter 4, and a new method of using gravitational potential to find cores is introduced. Chapter 5 investigates the reliability of clump-finding algorithms, and finds evidence that the core-mass function profile is universal. In Chapter 6 the first bound structures in a simulated molecular cloud are identified using the potential clump-finding routine, and their properties compared to observations. Following this, the cores are linked to the stellar mass formed from them in order to probe the connection between the core mass function and the IMF. Penultimately, in Chapter 7 the effect of the wider environment upon subsequent accretion is investigated, with particular reference to massive stars. Chapter 8 outlines my conclusions.

2

Smoothed Particle Hydrodynamics

This begins the first of three chapters on methodology. This chapter will focus on the Smoothed Particle Hydrodynamics (SPH) Method. Chapter 3 will outline the implementation of Turbulence into the simulations and finally Chapter 4 focuses on the Clumpfinding Method.

SPH is a Lagrangian hydrodynamics code. It is particle based and therefore requires no grids. This proves to be both the main advantage and disadvantage of the method. Unlike many grid codes, which must specify in advance where high resolution will be required, SPH will automatically vary its spatial resolution so that high density regions are resolved, as this is where the particles concentrate. This makes the method extremely flexible. Moreover, the simplicity of the algorithm means it is easier to implement than grid codes and generally requires less computational resources. For the work presented in this thesis the Lagrangian nature of SPH is particularly useful, as it allows the gas involved in star-formation to be directly traced.

However, the particle nature of the method can cause difficulties at fluid boundaries,

such as shocks, as will be discussed in this chapter. Also Agertz et al. (2007) showed that some dynamical instabilities such as the Kelvin-Helmholtz and Rayleigh-Taylor instabilities are poorly represented in SPH, although recently Price (2008) has presented a method of correcting this for the Kelvin-Helmholtz case.

The SPH method was first proposed by Lucy (1977) and has been utilised in many applications since. Notable contributions to its development include Gingold & Monaghan (1977); Larson (1978); Bate et al. (1995) The code used in this work was originally created by Benz (1990) but has since been considerably updated since (Bate & Bonnell, 2005). In recent years magnetic fields and radiative transfer have begun to be implemented into SPH codes (Stamatellos et al., 2007; Price & Bate, 2008; Bate, 2009), but these are outside the scope of this work.

2.1 The SPH Method

The basic concept of Smoothed Particle Hydrodynamics is that each particle represents a smoothed distribution of density which allows the fluid equations to be applied in a discretised form. A function, $f(\mathbf{r})$, defined over a space, $V(\mathbf{r})$, is smoothed via a kernel ,$W(\mathbf{r},h)$, as shown below.

$$< f(\mathbf{r}) >= \int_V f(\mathbf{r}')W(\mathbf{r}-\mathbf{r}',h)d\mathbf{r}' \tag{2.1}$$

where the kernel is parameterised by the smoothing length h and satisfies

$$\int_V W(\mathbf{r},h)d\mathbf{r}' = 1 \quad \text{and} \tag{2.2}$$

$$W(\mathbf{r}-\mathbf{r}',h) \rightarrow \delta(\mathbf{r}-\mathbf{r}') \quad \text{as} \quad \mathbf{h} \rightarrow 0. \tag{2.3}$$

Typically a sharply peaked function such as a Gaussian is used as the kernel. In this version of the code a spline kernel is used (Monaghan & Lattanzio, 1985), Eq. 2.4. This kernel has several advantages. Firstly, it is spherically symmetric, which is necessary for calculating the gravitational and pressure forces. Secondly, it is continuous up to its second derivative which allows the gradient of the fluid properties to be calculated. Finally, the kernel is zero when

$r/h > 2$ which limits the number of particles which contribute to local properties.

$$W(\mathbf{r},h) = \frac{\sigma}{h^\nu}\left(1 - \frac{3}{2}q^2 + \frac{3}{4}q^3\right) \quad \text{if} \quad 0 \le q = r/h \le 1 \tag{2.4}$$

$$= \frac{\sigma}{h^\nu}\left(\frac{1}{4}(2-q)^3\right) \quad \text{if} \quad 1 \le q = r/h \le 2 \tag{2.5}$$

$$= 0 \quad \text{otherwise.} \tag{2.6}$$

As the kernel is strongly peaked and spherical, the function $f(\mathbf{r})$ can be Taylor expanded to show that

$$< f(\mathbf{r}) >= f(\mathbf{r}) + c(\nabla^2 f)h^2 + O(h^3) \tag{2.7}$$

which means that $< f(\mathbf{r}) >$ can be replaced with $f(\mathbf{r})$ with the same accuracy as the smoothing length. This means the identity below must be true.

$$\left\langle \frac{A(\mathbf{r})}{B(\mathbf{r})} \right\rangle = \frac{< A(\mathbf{r}) >}{< B(\mathbf{r}) >} + O(h^2) \tag{2.8}$$

The function $f(\mathbf{r})$ is only known at N discrete points which are distributed as

$$n(\mathbf{r}) = \sum_{j=1}^{N} \delta(\mathbf{r} - \mathbf{r_j}). \tag{2.9}$$

Equation 2.1 can then be multiplied by $n(\mathbf{r}')/ < n(\mathbf{r}') >$ using Eq. 2.8, and then integrated to derive

$$< f(\mathbf{r}) >= \sum_{j=1}^{N} \frac{f(\mathbf{r}_j)}{< n(\mathbf{r}') >} W(\mathbf{r} - \mathbf{r_j}, h). \tag{2.10}$$

By noting that the number density is

$$< n(\mathbf{r_j}) >= \frac{\rho(\mathbf{r_j})}{m_j} \tag{2.11}$$

where $\rho(r_j)$ is the density of the j'th particle and m_j is its mass, equation 2.10 becomes

$$< f(\mathbf{r}) >= \sum_{j=1}^{N} \frac{m_j}{< \rho(\mathbf{r}') >} f(\mathbf{r_j}) W(\mathbf{r} - \mathbf{r_j}, h). \tag{2.12}$$

The above equation is the key concept of the SPH method, as the function $f(\mathbf{r})$ can be replaced with any variable which varies smoothly over space. For instance, the smoothed density will

be

$$< \rho(\mathbf{r}) >= \sum_{j=1}^{N} m_j W(\mathbf{r} - \mathbf{r_j}, h). \tag{2.13}$$

This is the mathematical expression of the basic concept of SPH discussed earlier. It also satisfies the hydrodynamic continuity equation, provided the particle mass remains constant.

The gradient of a quantity can also be formulated in a smoothed manner by differentiating Eq. 2.1 by parts and neglecting surface terms to give

$$< \nabla f(\mathbf{r}) >= \int f(\mathbf{r}')\nabla W(\mathbf{r} - \mathbf{r}', h) dr' \tag{2.14}$$

which, when discretised becomes

$$< \nabla f(\mathbf{r}) >= \sum_{j=1}^{N} \frac{m_j}{\rho(\mathbf{r}')} f(\mathbf{r_j})\nabla W(\mathbf{r} - \mathbf{r_j}, h). \tag{2.15}$$

Equation 2.15 has the advantage that for any given quantity, it is only the kernel which ever needs to be differentiated, and so these values can be tabulated to save computer time.

2.2 The Fluid Equations

In the SPH method the mass distribution is treated as a fluid, and each SPH particle represents a fluid element within the flow. Therefore the fluid equations form the basis of the SPH equations. The fluid equations can be formulated in two ways. In the Eulerian form the fluid properties are expressed at a fixed position, whereas in the Lagrangian form the position can vary. In effect the Eulerian form details the conditions at a spatial position and the Lagrangian form gives the conditions within an individual fluid element. Hydrodynamic grid codes are Eulerian but SPH is Lagrangian. To convert between these two formulations the relationship below can be used.

$$\frac{dQ}{dt} = \frac{\partial Q}{\partial t} + \mathbf{u}.\nabla Q \tag{2.16}$$

The first fluid equation in Eulerian form is conservation of mass.

$$\frac{\partial \rho}{\partial t} + \nabla(\rho \mathbf{u}) = 0 \tag{2.17}$$

This is automatically included in the SPH formalism as shown in Eq. 2.13. It is easy to satisfy this condition within SPH as each particle represents a fixed amount of mass, and as long as no particles are added or removed from the simulation mass is conserved. The momentum equation is

$$\frac{\partial \mathbf{v}}{\partial t} + (\mathbf{v}.\nabla)\mathbf{v} = -\frac{\nabla P}{\rho} \tag{2.18}$$

and the energy equation for an adiabatic equation of state is

$$\frac{\partial u}{\partial t} + (\mathbf{v}.\nabla)u = -\frac{P}{\rho}\nabla.\mathbf{v}. \tag{2.19}$$

2.3 The SPH Equations

2.3.1 Momentum Equation

The expression for conservation of mass has been derived in Eq. 2.13, and so the momentum will be found next. The momentum equation can be found by applying Eq. 2.1 to the Eulerian momentum equation and then placing the result into a discrete form, as shown in Benz (1990), to get

$$\frac{dv_i}{dt} = -\sum_{j=1}^{N} m_j \left(\frac{P_i}{\rho_i^2} + \frac{P_j}{\rho_j^2} + \Pi_{ij} \right) \nabla_i W_{r_{ij}h_{ij}} \tag{2.20}$$

for a particle pair i and j, where P is the pressure and Π is the artificial viscosity . The equation is formulated in this symmetrical manner so that the momentum is explicitly conserved for every pair of particles.

2.3.2 Equation of State

The equation of state used here is occasionally the simple isothermal equation

$$P = c_s^2 \rho \tag{2.21}$$

where c_s is the sound speed of the gas, but more commonly a more complex barotropic equation is used to mimic the behaviour of gas in a molecular cloud (Larson, 2005). This equation of state ensures that the Jeans mass at the point of fragmentation in a molecular cloud matches the characteristic stellar mass.

$$P = k\rho^{\gamma} \tag{2.22}$$

where k is a constant set by the entropy of the gas and γ is given by

$$\begin{aligned} \gamma = 0.75: &\quad \rho \leq \rho_1 &&\text{line cooling} \\ \gamma = 1.0: &\quad \rho_1 \leq \rho \leq \rho_2 &&\text{dust cooling} \\ \gamma = 1.4: &\quad \rho_2 \leq \rho \leq \rho_3 &&\text{optically thick to IR} \\ \gamma = 1.0: &\quad \rho \geq \rho_3 &&\text{allow sink formation} \end{aligned} \tag{2.23}$$

where $\rho_1 = 5.5 \times 10^{-19}$ gcm^{-3}, $\rho_2 = 5.5 \times 10^{-15}$ gcm^{-3} and $\rho_3 = 2 \times 10^{-13}$ gcm^{-3}.

This equation of state mimics the effects of line cooling (Larson, 2005; Jappsen et al., 2005) and then dust cooling when the dust is coupled to the gas (Masunaga & Inutsuka, 2000). When the gas becomes optically thick to IR radiation the gas will heat again. This heating is invoked at a somewhat earlier stage in the collapse than is typically the case to ensure the Jeans mass of a fragment is always resolved.

2.3.3 Artificial Viscosity

The treatment of shocks is one of the major challenges in SPH. In the SPH equations no dissipative term to model the conversion of kinetic energy to thermal energy in shocks has been included. This allows particle penetration, which occurs when streams of colliding particles are unable to dissipate their energy quickly enough, leading to an excess of kinetic energy allowing them to continue through each other. Additionally, as shocks are abrupt discontinuities, they are generally smaller than a smoothing length, and hence not resolved. To avoid this an artificial viscosity term is introduced which acts like a pressure term, and smoothes the shock over $3h$, allowing the shock to be resolved and the energy dissipated. The two artificial viscosity terms are

$$P_\alpha = \Pi_\alpha \rho^2 = -\alpha \rho l c_s \nabla.\mathbf{v}, \tag{2.24}$$

and

$$P_\beta = \Pi_\beta \rho^2 = \beta \rho l^2 (\nabla.\mathbf{v})^2, \tag{2.25}$$

where l represents the typical length scale over which the shock is spread and α and β control the strengths of the shocks. Eq. 2.24 is a bulk velocity term for the subsonic regime and Eq. 2.25 is a second-order von Neumann-Richtmyer viscosity for the supersonic case. The free parameters α and β typically have values of 1 and 2 respectively (Monaghan & Gingold,

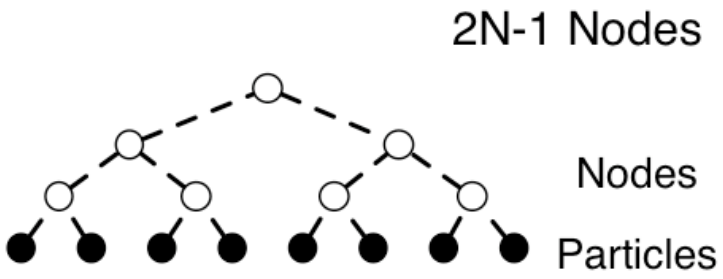

Figure 2.1: An illustration of the binary tree. SPH particles are combined hierarchically into nodes which can be substituted for their constituent particles within the gravitational force calculation.

1983). The artificial viscosity, Π_{ij}, is a combination of the above,

$$\Pi_{ij} = (-\alpha c_s \mu_{ij} + \beta \mu_{ij}^2)/\rho_{ij} \qquad \text{if} \quad \mathbf{v_{ij}}.\mathbf{r_{ij}} \leq 0, \tag{2.26}$$

$$= 0 \qquad \text{if} \quad \mathbf{v_{ij}}.\mathbf{r_{ij}} \geq 0 \tag{2.27}$$

where

$$\mu_{ij} = \frac{h\mathbf{v_{ij}}.\mathbf{r_{ij}}}{\mathbf{r_{ij}}^2 + \eta^2} \tag{2.28}$$

given that $\mathbf{v_{ij}} = \mathbf{v_i} - \mathbf{v_j}$, $\rho_{ij} = (\rho_i + \rho j)/2$ and $\eta^2 = 0.01h^2$ to avoid divergence at small separations. Shock tube tests showing the effects of artificial viscosity and particle penetration can be found in Dobbs (2006).

2.3.4 Self Gravity

Gravity is included simply by reformulating the Poisson equation. Benz (1990) showed that the total gravitational force felt on a particle i is given by

$$-\nabla\phi_i = -G\sum_{j=1}^{N} \frac{M(r_{ij})}{r_{ij}^2}\frac{\mathbf{r_{ij}}}{r_{ij}}. \tag{2.29}$$

This term is added to the momentum equation, Eq. 2.20 to represent the self-gravity of the gas. Unfortunately this calculation scales as $N^2/2$ when summed over all the particles. To speed up the calculation an inverted hierarchical tree is used to form 'nodes' of several particles, which allows the force calculation to scale as $NlogN$. A graphical representation of the binary tree is shown in Figure 2.1.

Nodes are formed from two SPH particles or existing nodes and located at their centre of

mass. The quadrupole moment of the new node is calculated from its constituents and a node radius is calculated within which all its constituents are found. The smoothing length of the new node is set as the maximum value of its constituents smoothing lengths. Nodes distant from the point whose gravitational force is being calculated can be used directly instead of their constituent particles, by using their position and quadrupole moment. When computing the force on a particle a distance R from a particle with radius r, the node need only be expanded to its constituent particles if

$$\frac{R}{r} < \theta \tag{2.30}$$

where θ is the opening angle. The wider the opening angle, the more nodes must be opened; for example when $\theta = 0$ all the nodes are opened. Bate (1995) found that a value of $\theta = 0.5$ gives good efficiency with negligible errors.

2.3.5 The Energy Equation

For an isothermal equation of state the SPH energy equation can be found in a similar manner to the momentum equation by applying by applying Eq. 2.1 to the Lagrangian energy equation in terms of internal energy per unit mass to get

$$\frac{du_i}{dt} = \frac{P_i}{\rho_i^2} \sum_{j=1}^{N} m_j \mathbf{v_{ij}} \nabla_i W(r_{ij} h_{ij}) + \frac{1}{2} \sum_{j=1}^{N} m_j \Pi_{ij} \mathbf{v_{ij}} \nabla_i W(r_{ij} h_{ij}) \tag{2.31}$$

For the barotropic equation of state it is assumed that energy is conserved when including the heating and cooling within the equation of state.

2.4 Sink Particles

In order to represent star formation Bate et al. (1995) introduced non-gaseous, accreting particles, known as sink particles, into the code. Sink particles interact with gas particles only through gravity, and will accrete any bound particles which come within its accretion radius. They represent regions of star formation and prevent the simulation from slowing to a standstill, as the number of time-steps required to evolve the simulation increases with density. When an SPH particle reaches a critical density, it will be transformed into a sink along with its surrounding neighbours if it meets all the criteria below.

- the particle's density is above critical threshold, ρ_{crit}

- the particle's smoothing length is less than half the accretion radius of the sink which will replace it.
- the particle and its neighbours are bound
- the particle and its neighbours are collapsing
- there is no existing sink particle within the smoothing length of the new sink

To ensure the last of the above tests can be carried out, only one sink can be created at a time. If all these tests are satisfied, the densest particle will then be converted into a sink by combining its properties with its neighbours and then moving it to their centre of mass.

Particles are accreted by the sink particle if all of the following are true :

- the particle is bound to the sink
- the particle is within a specified outer accretion radius, r_{acc}
- the particle's specific angular momentum is lower than that needed to form a circular orbit
- the particle is more bound to the sink than any other sinks in the locality.

However, there also exists an inner accretion radius, usually set to be ten times smaller than the outer one, within which particles are accreted regardless of whether they satisfy the above. This is done to prevent sph particles being artificially accelerated by a close encounter with a sink particle. When the particle is accreted its mass, momentum and angular momentum are added to the sink, and the sink is moved to their joint centre of mass.

2.5 Evolution and Smoothing Lengths

The code is evolved using a leapfrog integrator and with individual time-steps. The time step will be either the Courant condition or the force resolution condition, whichever is smaller. The Courant condition is given by,

$$\delta t_C = C_{cour} min\left(\frac{h}{v_{sig}}\right) \tag{2.32}$$

where $C_{cour} = 0.4$ is the Courant number and v_{sig} is the maximum signal velocity between the particle pair, a b, given by

$$v_{sig} = 1/2(v_a + v_b + \beta|\mathbf{v_{ab}}.\mathbf{j}|) \tag{2.33}$$

with $\beta = 1$ when $\mathbf{v_{ab}}.\mathbf{j} > 0$. The force resolution condition was derived in Monaghan (1992) to be

$$\delta t_f = 0.3\sqrt{\frac{h}{|F|}}. \tag{2.34}$$

The time-step is then rounded to an integer multiple of two of a specified minimum time-step so that the particle evolutions are synchronised at a set synchronisation time. At this point all the particles are updated and generally printed to a data dump. Particles can have their time-step moved to a lower level at any point in the simulation as required. Time-steps can only be increased if this still allows them to be evaluated at the synchronisation time. Variable time-steps allow the simulation to be evolved without wasting computer time by integrating particles to a greater accuracy than needed.

The smoothing lengths are allowed to vary to maintain a roughly constant number of neighbours (usually 50, but it can be as much as 70 or as little as 30) when computing forces, and thereby improve the efficiency of the code. The new smoothing length of a particle should be,

$$h = h_0\left(\frac{\rho_0}{\rho}\right)^{1/3}. \tag{2.35}$$

where h_0 and ρ_0 are the original smoothing length and density of the particle. However, the smoothing length is itself needed to calculate the density. Benz (1990) showed that this can be avoided by using the derivative of Eq. 2.35,

$$\frac{dh}{dt} = \frac{1}{3}\frac{h}{\rho}\frac{d\rho}{dt} \tag{2.36}$$

which by applying the continuity equation becomes,

$$\frac{dh_i}{dt} = \frac{1}{3}h\nabla.\mathbf{v_i}. \tag{2.37}$$

This quantity is then integrated along with the other SPH equations to give each particles smoothing length at any time.

This means that the smoothing length is lowest at high densities. Therefore high density regions are the most resolved. This is a real strength of using the SPH method for star formation because most computer time is automatically spent on the regions where the stars will form. In order to keep the forces on a particle balanced and ensure momentum is conserved, the smoothing length is generally symmetrised as

$$h = h_{ij} = \frac{h_i + h_j}{2}. \tag{2.38}$$

3

Initialising Decaying Turbulence

Chapter 3 continues to discuss methodology, in this case the implementation of turbulent velocities into an SPH simulation.

A key feature of the Molecular Clouds within which stars form is wide line-widths indicating supersonic turbulence. As discussed in Chapter 1, turbulence supports the cloud globally, but the high ram pressure gradients that are a feature of a turbulent flow create strong density enhancements. The high density of these regions lowers the Jeans Mass, allowing the overdensities to collapse, and potentially form stars. It has been suggested by several authors (e.g. Padoan & Nordlund, 2002; Klessen, 2001) that as these density perturbations are formed from turbulence their Salpeter like mass function is likewise a direct consequence of turbulence. It is therefore essential that turbulence is modelled correctly for an accurate depiction of protostellar cores. In this chapter I outline the properties of supersonic turbulence, describe how it is initialized in the SPH simulations and test its implementation.

3.1 Turbulent Fragmentation

3.1.1 Subsonic Incompressible Turbulence

The most studied form of turbulence is the subsonic incompressible turbulence found on Earth. Turbulence was defined by Hinze (1975) as

> Turbulent fluid motion is an irregular condition of flow in which the various quantities show a random variation with time and space co-ordinates, so that statistically distinct average values can be discerned.

In addition to this, turbulence also spans a wide range of scales.

The wavelengths at which there is turbulence range from a minimum value set by viscous dissipation at the molecular level, up to the length scale of the turbulent region. Kinetic energy cascades down the scales due to vortex stretching. Turbulence can be thought of as a series of eddies, each eddy being a local swirling motion where there is intense vorticity. A vortex will be stretched if it is aligned in such a way that mean velocity gradients will amplify it. Most of the turbulent energy is contained in the large scale eddies, but most of the vorticity is in the small eddies. Note that eddies overlap in space with small eddies being carried within larger ones.

Turbulence is a dissipative process; it will decay and as it does so the energy transfers from larger eddies to smaller energies. Finally, on the smallest scales, energy will be dissipated as heat due to molecular viscosity. An introduction to turbulence is found at the beginning of Wilcox (1998).

Kolmogorov was one of the trail breakers in the field of turbulence, and was among the first to analyse turbulence in terms of its spectral distribution of energy. A spectral representation is a Fourier decomposition into wavenumbers κ. Here the wavenumber physically represents the reciprocal of the eddy size. Kolmolgorov concluded that there is a range of wave-numbers intermediate between the largest and smallest scales where energy is transferred only by inertial effects and the energy spectral density, $E(\kappa)$, can be represented as the power law

$$E(\kappa) = C_K \epsilon^{2/3} \kappa^{-5/3} \qquad 1/l << \kappa << 1/\eta \tag{3.1}$$

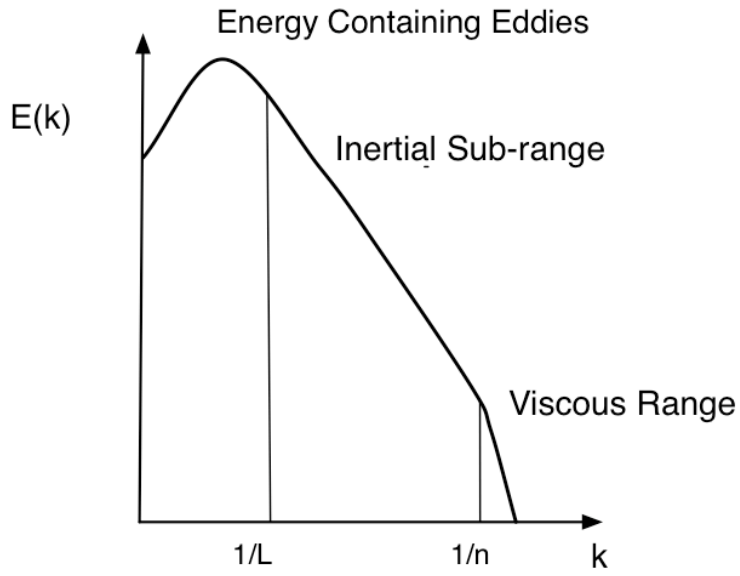

Figure 3.1: The energy spectrum for a turbulent flow in log-log scales, adapted from a graph from Wilcox (1998)

where C_K is the Kolmogorov constant, ϵ is the rate at which larger eddies supply energy, l is the length scale of the region and η is the Kolmogorov length scale. Figure 3.1 shows the typical energy of a turbulent flow.

3.1.2 Turbulence in Molecular Clouds

While the turbulence in molecular clouds differs from the conventional case as it is supersonic and in a compressible self-gravitating medium, nonetheless there are many similarities. The picture of a cascade of energy transferred by eddy motions is still basically correct. However, in addition to eddies, there are also shocks which mean that densities can increase more rapidly than the subsonic case. Across an isothermal shock the jump condition is

$$\frac{\rho_1}{\rho_0} \approx M^2, \tag{3.2}$$

where ρ_0 and ρ_1 are the gas densities before and after the shock, and M is the Mach number, $M = v_{rms}/c_s$. Extremely large density enhancements can be generated by shocks as typical Mach numbers in MC's are of the order $M \approx 10$.

Turbulence in a molecular cloud can also be described by a power spectrum:

$$E(\kappa) \propto \kappa^{-n}. \tag{3.3}$$

The most commonly used value for the exponent is $n = 2$. This is the Burgers spectrum for pressureless turbulence (Gotoh & Kraichnan, 1993). This value is expected for shock dominated flows, as the Fourier transform of a velocity jump has a -2 energy power law (Passot et al., 1988). The connection between the n and the exponent in the Larson velocity dispersion relationship ($\sigma(v) \propto L^{\beta}$) is;

$$\beta = -(n+1)/2 \tag{3.4}$$

This means that a value of $\beta = 0.5$ follows naturally from a series of turbulent shocks. Therefore the Larson relation may have nothing to do with virial equilibrium.

The decay of turbulence in molecular clouds can be characterised by;

$$E_k \propto t^{-\eta} \tag{3.5}$$

where E_k is kinetic energy and t is time. The exponent η typically takes values around unity, Mac Low et al. (1998). It was originally thought that supersonic turbulence would decay more rapidly than the subsonic case, but they are now known to decay at similar rates. Magnetic fields were once thought to slow the decay of turbulence by transforming dissipative shocks into non-dissipative Alfven waves. However, Stone et al. (1998) showed that these Alven waves generate a spectrum of magneto-hydrodynamic waves that dissipate energy in a similar manner to the hydrodynamic case. All turbulence decays in a crossing time.

There are several mechanisms which could generate turbulence; many of which also create the molecular cloud in the first place, explaining why turbulence is a ubiquitous phenomenon. Gas density can be enhanced due to gravitational instability. In our galaxy this would equate to gas being compressed as it passes through the spiral arms. Here shocks will both further increase the density and generate the turbulence, (eg Roberts, 1969; Dobbs & Bonnell, 2007). Alternatively, the ram pressure from supersonic flows from supernovae could compress the gas and generate the turbulence (eg Mac Low et al., 2005). Silk (1985) propose that turbulence is generated by stellar winds and outflows.

3.2 Generating a Turbulent Velocity Field

In order to include turbulence in the SPH simulations, a turbulent velocity field must first be generated. Turbulent velocities are generated from a Gaussian random field using the power spectrum, shown in Figure 3.1. The program VELFIELD is used to generate the initial turbulent velocity distribution. VELFIELD follows the scheme outlined in Dubinski et al. (1995), is based on a code by Volker Bromm for the Zeldovich shift, and was written in its current form by Mathew Bate. This algorithm expresses the velocity field in terms of a vector potential, A, such that $v = \nabla \times A$ by making the assumption that the flow is divergence free. The components of A are randomly sampled in the Fourier plane and their amplitudes are taken from a Rayleigh distribution which has a dispersion given by the power spectrum, and phases uniformly sampled between $[-\pi : \pi]$. Components are sampled over a cubic grid and the Fourier transform of the curl of A is then taken to arrive at the velocity field. VELFIELD generates velocity grids in each of the x, y and z directions, with each being independent. As this is a random process, different realisations (using different seeds) of the velocity field look very different.

One potential problem with this method is that the velocity dispersion relation obtained from a realisation of a power law that is constant is different from that in which the realisation is always changing. Myers & Gammie (1999) showed that when the velocity field realisation is constant with time a power law exponent of $n = -3.5$ is more appropriate in Eq. 3.3 in order to give the desired velocity dispersion relationship. This value and a more or less constant realisation will be used for the majority of this chapter. This allows the observed velocity dispersion relation to be generated in a minimum amount of computer time, and has the additional advantage that the velocity field will not jump discontinuously between one value and another. Another method of generating the correct power spectrum while avoiding unphysical jumps in the velocity field would be to take the average field from a large number of realisations (Klessen & Burkert, 2000). However since the work outlined here uses high resolution velocity grids of size 128^3 which take at least a day to generate, this was thought impractical.

3.2.1 Simulation Properties

The above method for generating turbulence is now applied to an SPH simulation to investigate its effectiveness. Although several simulations are presented here they are all generated from the same initial SPH setup. The initial model of the molecular cloud consists of 5 million particles distributed randomly in a box 2 pc wide, which is a typical size scale for a large clump of star formation in an molecular cloud. The optimum SPH setup from this Chapter will be used in Chapter 5.

The simulated box has a mass of 118.2 $M_\odot$ which corresponds to a density of 10^{-21} g cm^{-3}, which is at the lower end of the density range within which molecular hydrogen can exist. The mass resolution of the simulation is 1.18×10^{-3} $M_\odot$ (about a Jupiter mass), which allows the entire brown dwarf regime to be resolved. The mass resolution here is equivalent to the mass of 100 SPH particles. The Jeans mass is 5.7 $M_\odot$ which results in a Jean number of 20.6. The Jeans number, J, is the ratio of gravitational energy to thermal energy. It is a useful quantity to know since the number of Jeans masses within in a cloud is equal to $J^{3/2}$. The simulated MC has a free fall time of 2.1×10^6 yrs and a sound speed of 0.18 kms^{-1}.

Some preliminary runs at lower resolution were tested before the modifications to the SPH code were applied to the high resolution molecular cloud simulation. Runs were carried out on either the SUPA altix computer at St-Andrews or on the UKAFF computer (UK Astrophysical Fluids Facility) at Leicester University, depending on which was available at the time.

In order to impose the velocity field onto the SPH particles, the velocity field grid is scaled to match the size of the 2 pc box being simulated. The velocity of the SPH particle in each dimension is interpolated from the surrounding grid points. The magnitude of the velocity field is normalised to ensure that the kinetic energy of the region is equal to its potential energy, which in this case corresponds to a Mach number of 4.25.

The velocity dispersion with increasing radius from the centre of the box is shown in Figure 3.2. The velocity dispersion satisfies the Larson dispersion relation in the range $0.1 < R < 0.5$ pc. Below this the gradient is steeper, as there is a finite length between grid points, below which the turbulence cannot be applied. Above this range the gradient flattens, which is inevitable when the volume over which the dispersion is calculated nears the driving scale of the turbulence. In reality the driving scale of the turbulence would be much larger than the

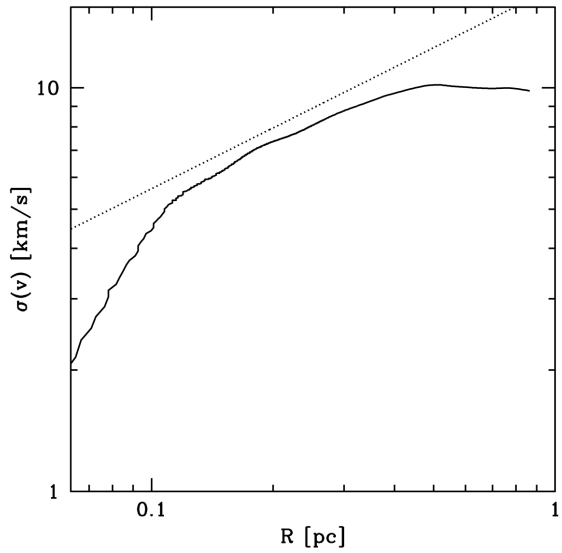

Figure 3.2: The velocity dispersion from the centre of the SPH distribution once the velocity field has been applied. The dotted line shows the gradient of the velocity dispersion when $\beta = 0.5$ in equation 1.1. In the range $0.1 < R < 0.5$ pc the Larson relation is satisfied.

box, but computational limitations mean that the width of the box is the largest scale at which turbulence can be driven. In observational studies, the Larson relation is generally found by plotting the velocity dispersion of individual clumps and MC's, and would not be found by sampling from an individual object. However the principle is the same, and Figure 3.2 shows that the generated velocity field is consistent with the observed velocity dispersion relation. The total velocity dispersion of the region measured from the centre is about 10 kms^{-1}.

3.2.2 Periodic Boundaries

To generate the structure from turbulence the simulation is initially evolved without self gravity. However, the high velocities and pressure from the turbulence will cause the region to expand, and a significant proportion of the original gas will be lost. One method of avoiding this is to confine the mass to the box via pressure from external ghost particles. Ghost particles are virtual SPH particles which exist outside the boundary of the simulation and interact with the particles near the boundary. They act as a confining force on the material being simulated. If an SPH particle does manage to cross over the boundary it should be put back inside the box so that mass, energy and momentum are conserved. The SPH subroutine Periodic Boundaries was first parallelised to increase speed and then used for this purpose. If a particle exits the box on one side, it will be put back on the opposite side, but with its velocity still oriented

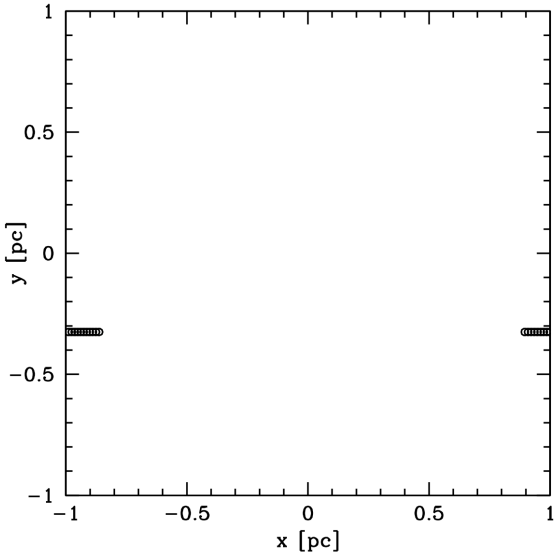

Figure 3.3: The positions of a test particle, originally situated at the co-ordinates $[0.89 : -0.32]$ in a uniform flow from left to right with time.

in the original direction. This is not too physically unrealistic as in reality mass would flow both in and out of a dynamical region, and additionally the velocity field is generated in such a way that it joins smoothly on to the other side of the field at the edges.

Since the velocities being considered here are supersonic, it is likely that at least some of the particles will manage to escape the boundaries, therefore this feature of the code is now tested. An SPH particle distribution of 10^4 particles is set up in a 2 pc wide cubic box in a cubic lattice distribution with a mass of $100M_{\odot}$. The particles are given a velocity equal to the sound speed in the positive x-direction and the region left to evolve for twenty timesteps. Figure 3.3 shows the position of a test particle in the SPH distribution at each timestep. It can be seen that as the particles reach the boundary at the right hand side they successfully re-enter on the left hand side with their original velocity.

3.2.3 Re-applying the Velocity Field

To generate the initial conditions for Chapter 5 the SPH particles are left to develop structure by moving under the influence of the velocity field without self-gravity. The resulting structure is due purely to hydrodynamics. However, by the time the density distribution is consistent with observations the turbulence will have decayed. If star formation is simulated from these conditions then power may have been lost from the turbulent energy spectrum. Figure 3.4 shows the decay of energy in the absence of driven turbulence in a simulation with the same

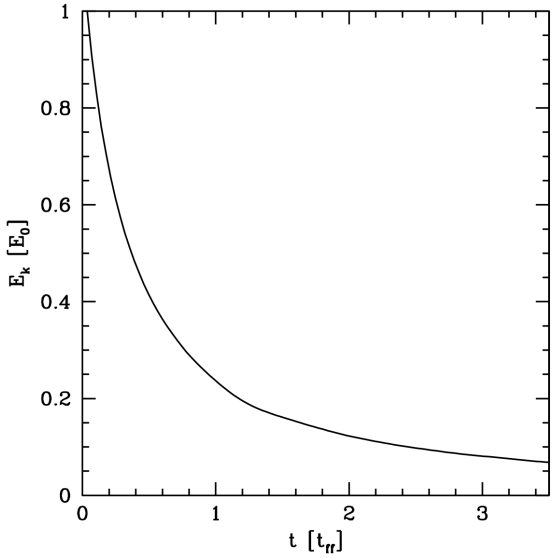

Figure 3.4: The decay of turbulent kinetic energy (in units of initial kinetic energy) in the absence of driving and self-gravity.

physical properties as earlier discussed, but with a lower resolution (10^6 particles).

After half a free fall time, the kinetic energy in turbulence is 0.4 times its original value, and by 2.5 free fall times it has decayed below an order of magnitude of its original value and is still decaying. Dissipation of energy is primarily through shocks as there is no self-gravity. Figure 3.5 shows a projection of the column density of the region after the turbulence has decayed for 1 t_{ff}. The structure is filamentary and has clear shock fronts. The probability density function (PDF) of the model at 1 t_{ff} is shown in Figure 3.6. The PDF resembles a lognormal, which is characteristic of structure resulting from turbulence in an isothermal gas (Scalo et al., 1998). Therefore the generated structure resembles molecular cloud conditions.

However, although the structure generated is a good representation of a molecular cloud, some of the energy from shocks will have been dissipated, particularly from small scales. In an effort to avoid this, the turbulence shall now be 'driven' throughout the evolution without self-gravity. To drive the turbulence, the turbulent velocity field is re-imposed at intervals throughout the evolution. To do this, the SPH code was altered so that after a synchronisation time the velocities of all the particles were replaced by the velocity obtained by interpolating from the velocity field grid. Once again the kinetic energy in turbulence was kept equal to the potential energy of the region, which corresponds to a Mach number of 4.25.

The cloud was left to evolve for a free fall time until the PDF shown in Figure 3.7 had

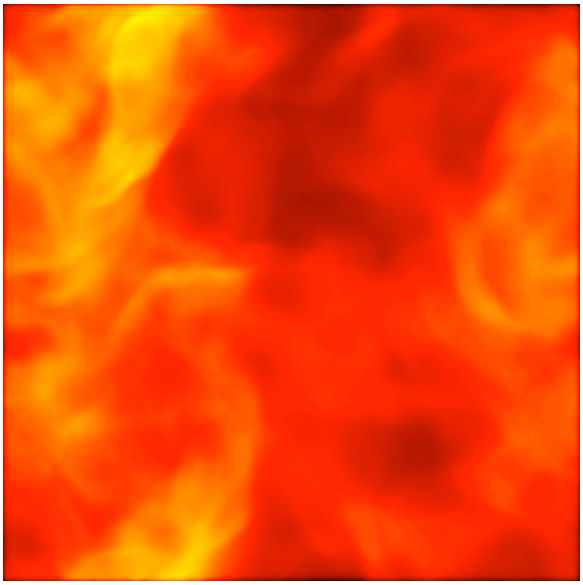

Figure 3.5: The column density after the turbulence has decayed for 1 t_{ff}. The colour scale denotes column densities in the range, 0.001 $g\,cm^{-2}$ *(dark red)* to 0.1 $g\,cm^{-2}$ *(yellow/white)*.

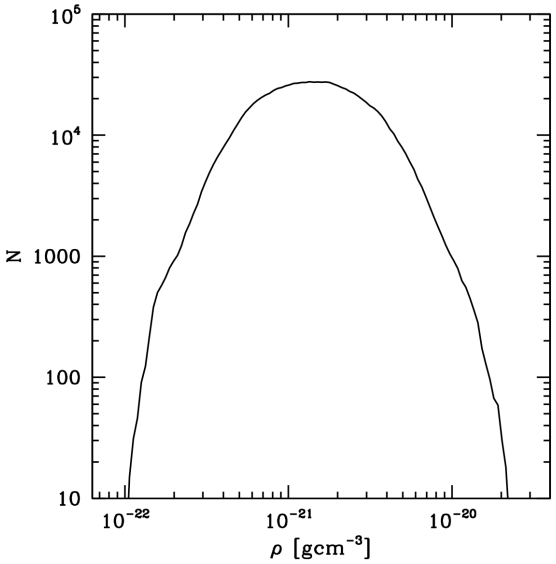

Figure 3.6: The PDF of the gas after the turbulence has decayed for 1 t_{ff}. The PDF resembles a lognormal as is expected from turbulence in an isothermal gas.

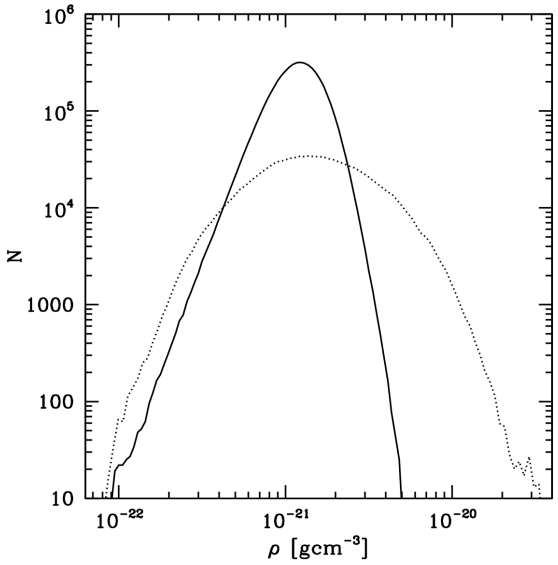

Figure 3.7: The PDF of the gas after 1 t_{ff} when the turbulence was continuously re-imposed throughout its evolution *(solid line)*. When compared to the PDF from decaying turbulence *(dotted line)* less dense gas had been created.

developed. The PDF is not as close to lognormal as in the decaying case. While the low density side and the peak of the distribution (at just over 10^{-21} gcm^{-3}) are in the same places as Figure 3.6, less high density gas has been generated. Figure 3.8 shows the column density projection at the end of the evolution with the same scale as Figure 3.5. It is immediately clear that the density has been less enhanced, and less large-scale structure has been formed. The new initial conditions, therefore, are not as good a representation of structure in molecular clouds as the case without driving. However, the velocity field has not decayed in any way, and the density field is necessarily consistent with it since it evolved from the velocity field. The densities were probably less enhanced because the velocities were set back to their original values, allowing high density regions to re-expand.

3.2.4 A More Realistic Driving Scheme

The previous attempt at driving turbulence suffered from the fact that the same velocity field was re-applied every time, meaning that there were no real bulk motions in the gas. The velocity field will now be altered over time by generating two realisations (A & B) from different seeds and interpolating between them so that at $t = 0$ velocity field A is applied, at $t = 1$ field B is applied and a mixture of the two between times. The velocity field V(t) was given by Eq.

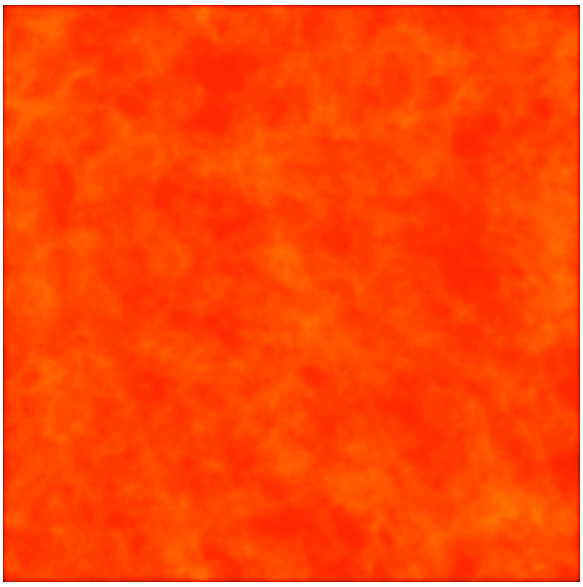

Figure 3.8: The column density after 1 t_{ff} when the turbulence was continuously re-imposed throughout the evolution. The colour scale denotes column densities in the range, 0.001 $\mathrm{g\,cm^{-2}}$ *(dark red)* to 0.1 $\mathrm{g\,cm^{-2}}$ *(yellow/white)*.

3.6 where t is in units of the free fall time.

$$V(t) = A(1-t) + Bt \qquad 0 \leq t < 1 \tag{3.6}$$

An additional realisation, C, was generated so that if the time is greater than one free fall time the velocity is

$$V(t) = B(2-t) + C(t-1) \qquad 1 \leq t < 2 \tag{3.7}$$

and so on.

In Section 3.2.3 no knowledge of the previous velocities of the gas particles is retained, as the particles velocity is overwritten each time the velocity field is re-imposed. This is perhaps unrealistic, so to correct this the relationships in Eqs. 3.8 & 3.9 are used.

$$\delta v = \zeta(V_i - u_i) \tag{3.8}$$

$$v_i = u_i + \delta v \tag{3.9}$$

where u_i is the old velocity of the particle, v_i the new velocity and V_i the value of the velocity field at that point. The parameter ζ is a constant that can be adjusted so that the energy injected by turbulence is constant with time. It was found through trial and error that a value

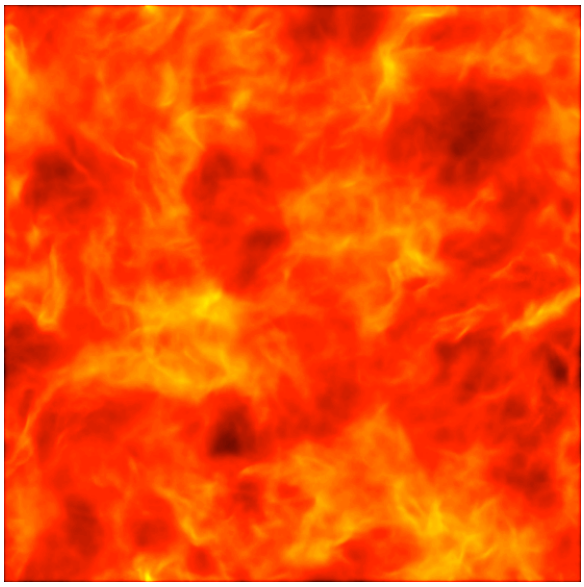

Figure 3.9: The column density after 1 t_{ff} when the turbulence was driven with the new scheme. The colour scale denotes column densities in the range, 0.001 $\mathrm{g\,cm^{-2}}$ *(dark red)* to 0.1 $\mathrm{g\,cm^{-2}}$ *(yellow/white)*. The density distribution is clumpy and has large scale structure.

of $\zeta = 0.5$ roughly achieves this.

With these modifications the initial conditions were once again simulated by evolving the gas for 1 t_{ff} without self-gravity. Figure 3.9 shows the resulting column density, and Figure 3.10 the density PDF. The column density projection shows that the new driving method has been more efficient at generating clumpy, filamentary structure, and is more reminiscent of actual molecular cloud structure than Figure 3.8. The PDF of the region is not a perfect lognormal, as one side is definitely longer than the other, but a wider range of densities are produced than in the decaying case. Again, by definition, this density distribution is consistent with the turbulent velocity field, so when combined with the improvement in physical structure, it is safe to say that these initial conditions are better than the previous case.

3.3 Decaying Turbulence

In the subsequent simulations the turbulence will be driven without self gravity to create the initial conditions, but once self-gravity is turned on to allow star formation, the turbulence will no longer be driven. If the turbulence was continued to be driven when self-gravity was switched on, the gas would have a succession of unphysical velocities applied to it as it collapsed through the velocity field. Some authors avoid this problem by using a periodic gravity scheme, which replicates the effect of the simulated region being surrounded on all

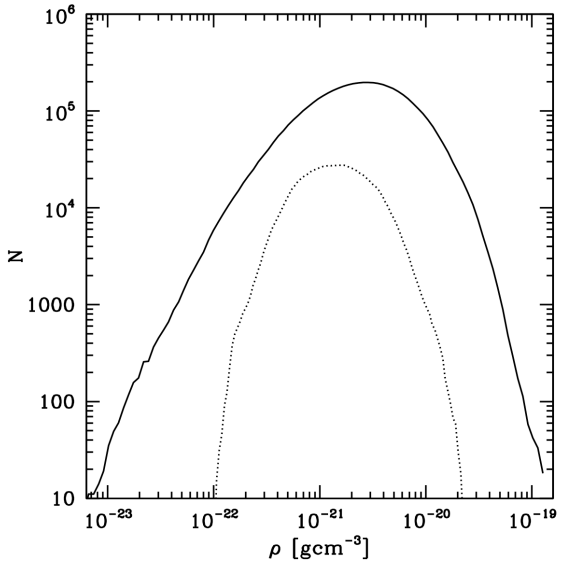

Figure 3.10: The PDF of the gas after 1 t_{ff} when the turbulence was driven with the new scheme *(solid line)*. When compared to the PDF from decaying turbulence *(dotted line)* a greater range of densities have been produced. Note, that N is higher in the driven case merely because this simulation was carried out at higher resolution.

sides by an infinite gas cloud, and so there is no net collapse and hence the gas can continue to be driven.

However, by applying arbitrary velocity kicks, structures may be destroyed simply due to their location relative to the velocity field. The actual mechanism for driving turbulence in molecular clouds is as yet unproven, so this may or may-not be a valid approach. In this thesis the assumption is that the turbulence was created as a by-product of forming the molecular cloud (Heitsch et al., 2006; Dobbs & Bonnell, 2007) and after this point it decays.

However, the process of gravitational collapse does itself release kinetic energy as the gravitational potential deepens, which produces velocities which resemble turbulence. If the mass distribution was purely symmetric then these would all be directed radially inward, but since the distribution is asymmetric with originally disordered velocities, conservation of angular momentum will ensure that transverse velocities are also generated. Figure 3.11 shows the decaying kinetic energy of the gas as the cloud collapses compared to decay without self-gravity. At 1 t_{ff} the kinetic energy begins to rise again when the onset of star formation randomises the central velocities. Figure 3.12 shows the velocity dispersion from the centre of the molecular cloud as it collapses. As the collapse proceeds, the velocity dispersion becomes steeper than the Larson case at radii larger than 0.1 pc. This appears to be due to

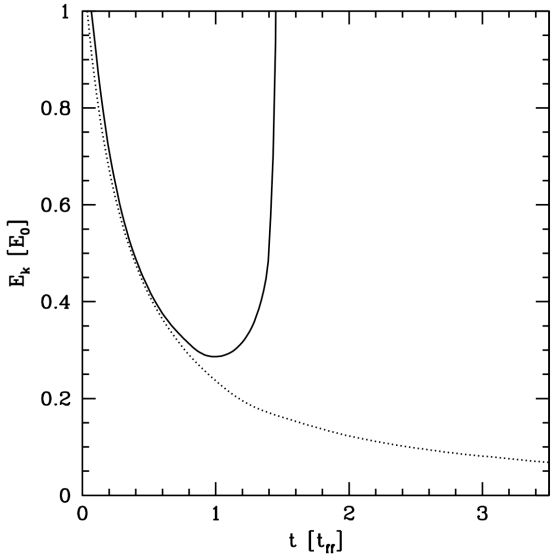

Figure 3.11: The decay of turbulent kinetic energy (in units of the initial kinetic energy) in a collapsing system *(solid line)*. The energy begins to rise again at 1 t_{ff} compared to the case without self-gravity *(dotted line* when the onset of star formation randomises the velocities.

the additional contribution to the velocity dispersion from in-fall motions. Below 0.1 pc the dispersions are in reasonable agreement with the Larson relationship. This is due to gas previously at larger radii collapsing to the centre and carrying the velocity field with it. Finally, the velocity dispersion becomes increasingly flattened in the outer regions of the box, where there is no longer much gas. Importantly, the velocity dispersion is still significantly supersonic at all points.

The initial driving of the structure has had a significant effect on the final PDF of the gas. Figure 3.13 shows that at 1 t_{ff} when the driven simulation has collapsed and will shortly form stars, the gas densities span 14 orders of magnitude, and reach a maximum value of 10^{-10} g cm^{-3}. If the decaying simulation is left to collapse similarly under self-gravity it is only able to reach densities of 10^{-17} g cm^{-3}. This difference is most likely due to the driven simulation having achieved greater density enhancements before its collapse, and therefore reaching higher densities more quickly. Therefore more of the substructure is due to turbulence than in previous cases.

3.4 Final Remarks

The final driving scheme discussed here has turbulent energies at small scales and high density enhancements. This scheme will be used to drive the turbulence in order to create the

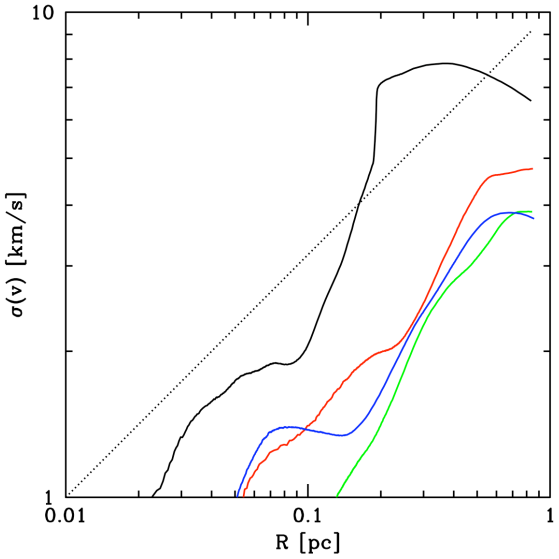

Figure 3.12: The velocity dispersion from the centre of the molecular cloud as it collapses. The dispersions are shown at 0.25 t_{ff} *red*, 0.5 t_{ff} *green*,0.75 t_{ff} *blue* and 1 t_{ff} *black*. The dotted line shows the gradient of the velocity dispersion when $\beta = 0.5$ in equation 1.1. The velocity dispersion becomes steeper at larger radii due to collapse motions.

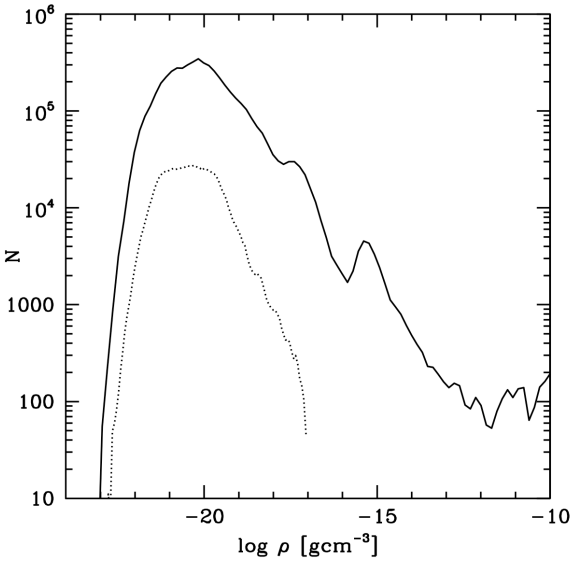

Figure 3.13: The PDF of the gas after it has collapsed for 1 t_{ff}. The solid line show the simulation which was initially driven, and the dotted line the simulation which has been allowed to decay.

initial conditions in Chapter 5, where the small scale structures created by a combination of turbulence and gravity will be identified.

4

Clump Finding

This Chapter describes the clump finding algorithms used in this work. Following this in Chapter 5 the application of clump finding to molecular clouds will be investigated. In Chapter 6 a new version of the clump finding algorithm using gravitational potential will be used to link pre-stellar cores to subsequent star formation.

The CLUMPFIND algorithm was introduced by Williams et al. (1994) as a method of detecting clumpy structures in observations of molecular clouds. This followed work by Stutzki & Guesten (1990) which identified clumps by fitting tri-axial gaussians to the observed emission. The CLUMPFIND algorithm had the advantages that it closely mimicked what was already being done by eye and it required no assumptions to be made regarding the clump geometry.

In Chapter 1 a clump was defined as being a region $0.3 - 3$ pc across which contained $50 - 500$ $M_{\odot}$. However the CLUMPFIND routine merely finds peaks in emission or density, so there is no intrinsic requirement for its outputs to be of a particular size. The structures

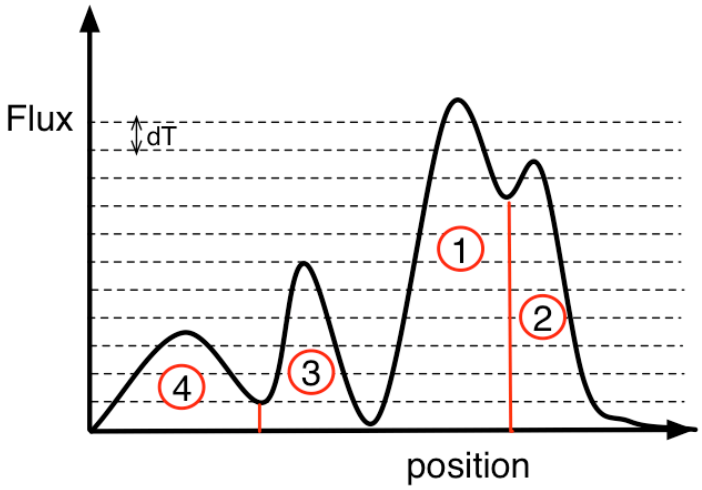

Figure 4.1: An illustration of the CLUMPFIND algorithm. Four clumps are assigned and they contain material down to the lowest contour.

identified from clump finding routines can therefore either be clumps or cores. This can cause considerable confusion. For the purposes of this and the following chapter, which both discuss the general clump-finding method, the term 'clump' shall be simply be used to denote any structure identified from a clump-finding routine.

4.1 The Clump Finding Technique

The algorithm introduced by Williams et al. (1994) works by contouring the emission in multiples of the rms noise ,T_{rms} and then searching for peaks in emission, T. Figure 4.1 shows a one dimensional illustration of how CLUMPFIND works. Starting with the highest contour, pixels are connected if they are within one grid cell of each other, either along the faces of the grid cell or along the vertices. Once all the pixels at a contour level are assigned, the analysis progresses to the next level down. If the pixels have neighbours at a higher level, they are assigned to the same clump, but if they are isolated then a new clump is formed. Contours which surround more than the one peak are assigned to the clump to which most of their neighbours belong using a 'friends-of-friends' algorithm. A neighbour is defined as being a pixel within a resolution element along two axes. This continues all the way down to the level of the background noise. Williams et al. (1994) showed that the contours are optimally spaced at $\triangle T/T_{rms} = 2$ to avoid identifying noise spikes as clumps.

Basically in CLUMPFIND the number of density peaks will correspond to the number of

clumps, which as shall be discussed later, can cause some problems when interpreting the results. However, when applied to an observational data-set, the clumps are considered complete above the level where there will be more than one pixel with $T > 2\triangle T$. In practice this will equate to at least 4 resolution elements.

4.2 2D Clump Finding

The above method was developed for observational data, but in this thesis simulated SPH data will be used instead. In order to do a fair comparison between the two, a version of the CLUMPFIND algorithm has been developed by Paul Clark which identifies clumps in SPH data as if the simulated data was from a two dimensional observation of column density.

There are two types data which can be obtained observationally: position-position (PP) and position-position-velocity (PPV) data. The column density projected along the line of sight is used to perform the clump-find in the PP case. In the PPV case, the column density per velocity channel is used. We generate these data-sets by interpolating the SPH particles to a grid of given resolution. Rather than interpolating to a full PPP grid and then integrating along the required line of sight, it is more efficient to integrate the spherically symmetric SPH smoothing kernel along the line of sight, and use the resulting 2D kernel to perform the interpolation.

Density contour levels are assigned to decide which density structures are significant. Classically a contour separation of two times the noise level is used, but as we have no noise in the simulated data we have to arbitrarily assign contours. After examining this repeatedly, a logarithmic contour separation of 5 contours per magnitude increase was generally used. Each grid cell is assigned an integer corresponding to its closest contour level. This is the quantity which will be used for the subsequent clump find. Upper and lower density values can be set at this point by defining an upper and lower contour level. As Pineda et al. (2009) have shown, clump-finding routines are very sensitive to the positions and number of contour levels. In this study the contour levels were kept static when other variables were considered.

The clumpfind itself is carried out in a similar manner to that of Williams et al. (1994). Grid cells are sorted in descending density order. Working down the list, if one of the cell's neighbours has been assigned to a clump then the cell is assigned to the same clump. If the cells neighbours are assigned to more than one clump, then the clump to which the greatest

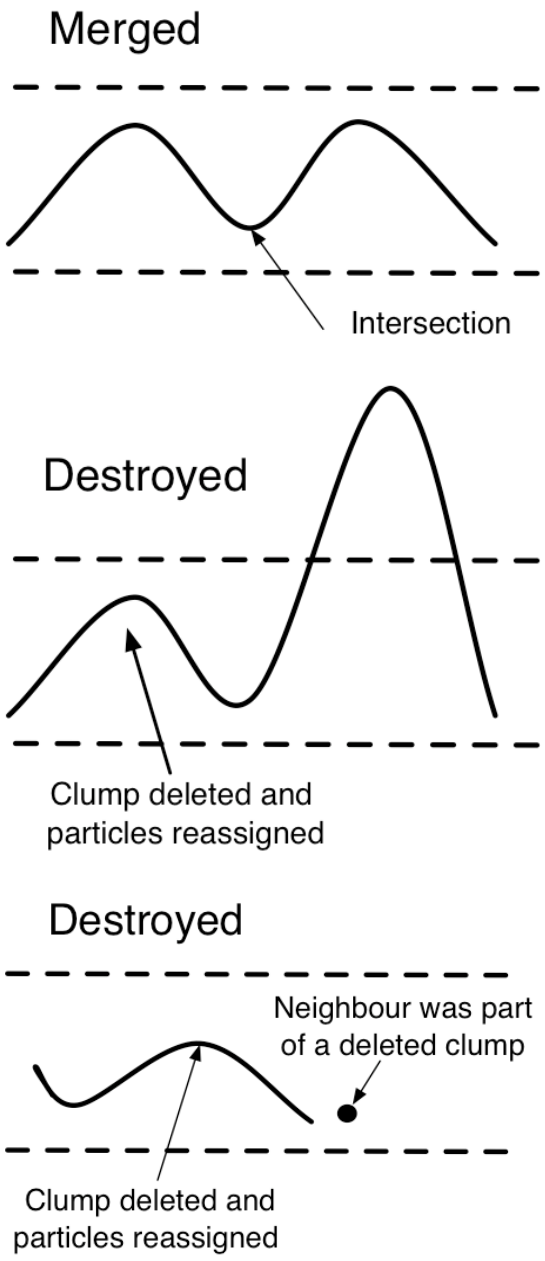

Figure 4.2: The use of contours to merge and destroy clumps.

number of its neighbours belong shall be used. If there is a tie, the clump with the highest density neighbour is used. If none of the neighbours have been assigned then the cell is the head of a new clump.

Contours are also used to make sure that spurious clumps are not identified as shown in Figure 4.2. If the head cells of two neighbouring clumps and the cells at the clump intersection are all on the same density contour the clumps are merged. In the case of two neighbouring

clumps if either clump's head cell is on the same contour as the intersection but the other's head cell is on a higher contour, then the smaller clump is destroyed. If a clump is within a contour from intersection to head and has a neighbour which was part of a deleted clump, then the clump is destroyed. After the spurious clumps have been deleted, the particles which used to belong to them are checked to see if they should be reassigned to a neighbouring clump. A similar technique has been used by other authors (e.g. Klessen & Burkert 2000)

There is one further subtlety. It is common for observational data to have its background subtracted before the CLUMPFIND is carried out. This is in an effort to prevent emission from along the line of sight contaminating the clump and artificially inflating the mass assigned to it. To mimic background subtraction we can apply a 'lowest common contour' definition when assigning the boundaries. Instead of assigning material to a clump down to the minimum contour level, material is only assigned down to the level of the highest density boundary cell (where the clumps intersect). If there are no clumps bounding the clump, material will be assigned to the minimum contour as before.

Clumps are deleted if they contain less than the sph resolution requirement of 100 particles to resolve gravitational collapse (Bate & Burkert, 1997). After the clumps have been merged and destroyed they are re-labeled.

The properties of the assigned clumps can then be calculated using only quantities available to an observer, such as column density, radial velocity and projected size. For example the masses of the clumps are calculated by multiplying the area of the assigned grid cells by their column density, rather than using the sum of the assigned SPH particles.

4.3 3D Clump Finding

For the 3D method we use the SPH particles directly as laid out in the appendix of Klessen & Burkert (2000). Since in SPH a neighbour list is maintained to calculate the density and forces acting on a particle, there is no need to assign particles to a grid. Particles are assigned integer contour levels as before. Since we are now dealing with intrinsic density as opposed to column density, there is a larger dynamic range and so in total more contours are used. Apart from these distinctions the method is the same as above.

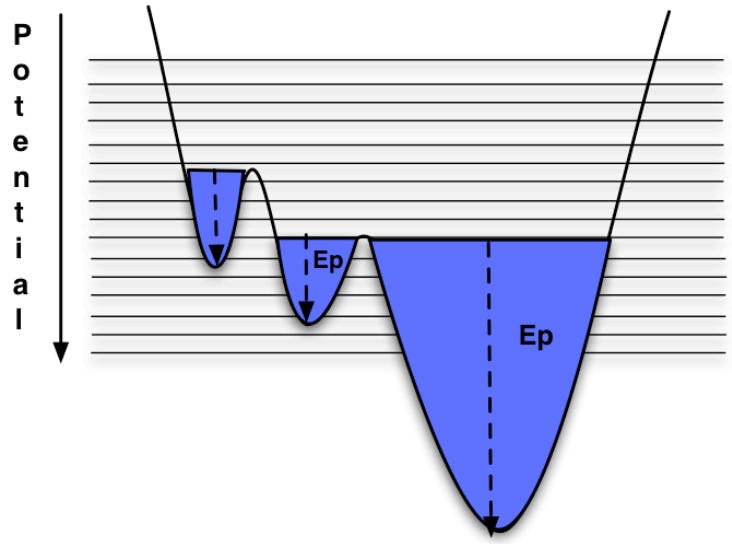

Figure 4.3: A cartoon of the potential **clump finding** process in 1D. For the potential and contours shown, the blue regions contain material which would be assigned to p-cores.

4.4 Potential Clump Finding

The modification of the previous clumpfind method to work on gravitational potential rather than density represents one of the major innovations of this thesis. This resolves many of the difficulties previously encountered. Unlike the density distribution, which has a lot of variation, the distribution of gravitational potential is much smoother, which removes the need to remove spurious clumps. Additionally, as it is the gravitational potential which actually determines how the mass will move, the clumps have a clearer physical interpretation. They are gravitational potential wells, and if the energy of the gas within them is insufficient to balance gravity they will collapse. The objects identified by this algorithm are typically small scale potential wells, with a mass in the core regime. Therefore, to distinguish them from the outputs of the density clump-finds, they shall be referred to as 'p-cores'. Note that there is no intrinsic requirement that a p-core is bound, as it may have sufficient internal energy (both thermal and kinetic) to prevent collapse.

I have modified the previously described algorithm to use gravitational potential to identify clumps rather than emission or density. In this case the SPH particle with the deepest gravitational potential forms the head of a clump, then the particle with the next deepest potential is either assigned to the same clump if it is a neighbour, or forms a new clump if not, and so on. The lowest common contour definition is always used for the boundaries so

the clumps are defined down to either a maximum potential, or the lowest contour which it shares with a neighbouring clump. Unlike the traditional CLUMPFIND algorithm, we use contour levels primarily to define the level at which potential clumps join, rather than to distinguish clumps from noise, and so our contours are numerous and finely spaced. Typically at least a thousand contours are used per magnitude in each clumpfind.

As the p-cores are only defined down to a shared contour level, the background potential is removed. This is necessary as gravity is a long range force, and so is affected by both the mass inside and surrounding the p-core. Hence when calculating an individual p-core's gravitational potential, the contribution from the larger structure that it is embedded within must be removed. This ensures that if all supporting forces are removed, all the gas in a p-core will collapse to the same point.

P-cores, therefore, represent the local potential minimums below the surrounding background. Figure 4.3 shows a simple 1D cartoon of the potential clump finding algorithm where three potential clumps have been identified. The depth of the potential well is taken as the difference between the highest and lowest potential assigned to the clump. This gravitational potential energy can be used with the kinetic and thermal energy of the particles to calculate how bound the clump is. One potential caveat is that when the binding of a p-core is calculated, as shall be discussed further in later chapters, surface terms are not considered. This means that factors such as the pressure balance at the core boundary have not been included in the analysis. However, in practice it is found that all bound p-cores in this work do collapse, so this simple definition of binding is considered sufficient.

In the next chapter the density clumpfind algorithms will be tested in a simulated molecular cloud to see how consistent their results are. In Chapter 6 the potential clump-find algorithm will be used to identify the earliest bound structures in a simulated Giant Molecular Cloud.

5

The Universality of the Clump Mass Function

It is unclear whether the current observations of the clump mass function can unambiguously support the cloud fragmentation picture. Typically, the observations must rely on two-dimensional column density maps (PP), which are limited by resolution and sensitivity, and the observed features in the column density may be contaminated by integrated emission along the line-of-sight. Three-dimensional information is only available by obtaining position-position-velocity (PPV) cubes of the emission from a particular molecular tracer. Converting between emission and column density relies on many assumptions (Pineda et al., 2008) and accounting for the properties of dust is itself challenging (Schnee et al., 2006). Further, the observed emission is itself dependent on the entangled effects of density, temperature, molecular tracer properties, and the observational technique (di Francesco et al., 2007)

In this chapter, I investigate how the differences in the form of the data – whether it be PP, PPV or full three-dimensional PPP – affects the resulting CMF. In particular how the resolution of the data and orientation of the cloud affect the mass function's profile is explored. To allow a comparison of observational style clump-finds to full three dimensional clump-finds,

the data must necessarily be synthetic. As such the results from a high-resolution smoothed particle hydrodynamics (SPH) simulation of driven turbulence are used. A full description of this simulation is presented in Section 6.2. To produce the PP and PPV style clump-finds the SPH data is interpolated to a grid, while for the PPP data the clump-find is done directly on the SPH data. The method used to extract the clumps has been described in the previous chapter.

5.1 The Clump Mass Function

Recent observations (Motte et al., 1998; Johnstone et al., 2000, 2006; Nutter & Ward-Thompson, 2007; Alves et al., 2007; Ward-Thompson et al., 2007) of dense gas cores in molecular clouds have shown that their distribution resembles the stellar initial mass function (IMF). It is hoped that by studying these dense cores the earliest stages of star formation can be probed and the origins of the IMF revealed.

As discussed in the Chapter 1, Motte et al. (1998) have shown that the clump mass function (CMF) in ρ Oph can be described by a similar power-law fit as the IMF. Similar results have been confirmed by a number of authors, although the range of core masses found and the break mass of the power law fit can vary (Johnstone et al., 2000, 2006; Nutter & Ward-Thompson, 2007; Alves et al., 2007; Testi & Sargent, 1998).

One interpretation of the similarity between the CMF and IMF is that the masses of stars are controlled solely by the fragmentation of the cloud. Myers (2008) propose that for cores with a high density contrast to their surroundings, the resulting protostellar mass will be the gas mass whose free-fall time equals the core dispersal time due to outflows. Additionally Swift & Williams (2008) take a slightly different approach and argue that the resulting shape of an IMF formed from a Saltpeter-like CMF is robust against different core evolution scenarios. This chapter shall show that the shape of clump mass function seems to be a ubiquitous feature of molecular clouds, but the identified clumps and their masses are sensitive to the method used to find them.

Molecular cloud (MC) structure as a whole is complex, filamentary and extends through all observable scales (Williams et al. 2000). It can also be thought of as hierarchical: small dense cores are part of small clumps of gas which are themselves part of larger gas clumps. This continues over the full spatial range of observations (Bergin & Tafalla, 2007). MCs also

Table 5.1: All the clump-finding presented in this paper were performed on a single SPH simulation. The initial conditions of the simulation are given here. The mass resolution is the minimum mass gravitational forces can be resolved for and is calculated via $M_{res} \sim 100 M_{total}/N_{part}$. The Jeans mass, free-fall time and sound speed are calculated from the average density of the simulation before collapse using the formulae $M_J = (4\pi\rho/3)^{-1/2}(5kT/(2G\mu))^{3/2}$, $t_{ff} = (3\pi/(32G\rho))^{1/2}$.

Size	2 pc cube
Mass	118.2 $M_\odot$
Particles	5000211
Mass resolution	2.36×10^{-3} $M_\odot$
Jeans mass	5.7 $M_\odot$
Free-fall time	2.1×10^6 yrs
Sound speed	0.18 kms^{-1}

exhibit supersonic turbulence. Larson (1981) showed that the internal velocity dispersion $\sigma(v)$ of a cloud is related to its size L by the relation $\sigma(v) \propto L^{-0.38}$. Such a scale-free relation is a natural outcome of a turbulent cascade, and Brunt & Mac Low (2004) propose that compressible shock dominated Burgers turbulence is highly consistent with observations.

As supersonic flows compress the gas in the molecular cloud they create a complex filamentary density field, suggesting that the observed structure in MCs is a direct consequence of turbulent motions (Klessen & Burkert, 2000; Klessen, 2001). At the smallest scales of the hierarchy, the transonic dense cores formed by the turbulent cascade may be the precursors of star formation (Goodman et al. 1998, Ward-Thompson et al. 2007). Indeed Padoan & Nordlund (2002) have predicted that mass distribution of Jeans unstable clumps created by super-Alvenic turbulence will resemble the IMF, a prediction that is supported by the observations of the CMFs discussed above.

5.2 The Simulation

The initial conditions of the SPH simulation used in this chapter are shown in Table 5.1. The molecular cloud has a mass of 118.2 $M_\odot$, roughly comparable to the masses of the 'cores' in ρ Oph (Motte et al., 1998). The cloud is modelled with $\sim$ 5 million SPH particles, which gives a mass resolution of 2.36×10^{-3} $M_\odot$ (Bate & Burkert, 1997). As such, clumps with masses in the brown dwarf regime can be resolved. The simulation was run on the SUPA Altix computer at the University of St Andrews.

Velocity and density fields of the simulation are ensured to be self-consistent by the following method. A turbulent velocity grid, consistent with a Larson velocity dispersion of $\sigma \propto r^{0.5}$, is generated according to Dubinski et al. (1995) and Myers & Gammie (1999) as discussed

in Chapter 3. After half a free fall time of driving the probability distribution function of the gas has a lognormal shape as is expected for an isothermal gas without self-gravity, (Klessen & Burkert, 2000), and the turbulence has power on all scales. The turbulence has a r.m.s velocity of Mach 4.25 which corresponds to the simulated gas cloud being just kinetically supported (E_k=$|E_p|$).

The self-gravity is then switched on and the turbulent driving switched off, which allows the turbulence to decay. Mac Low et al. (1998) have shown that turbulence typically decays on a crossing time, however, the turbulence in the simulation remains supersonic throughout due to the conversion of potential energy to kinetic energy as the cloud contracts. Star formation, as modelled by the formation of the first sink particle, occurs after one free-fall time (2.1×10^6 yrs). At this point the molecular cloud has the filamentary structure typically seen in observations (e.g. Bergin & Tafalla 2007). The evolution of the cloud is not followed beyond the formation of the first sink (that is, the runaway collapse of the first core). Instead a snapshot of the cloud structure immediately before the formation of the first sink is used as the input data for the clump-finding comparison. Figure 6.1 shows a column density projection of the cloud at this point in the evolution.

A polytropic equation of state is used to mimic the evolution between the optically thin and optically thick regimes. Below densities of 10^{-13} gcm^{-3} the value of the exponent gamma is initially set to $\gamma = 1$ to mimic dust cooling. At gas densities of 10^{-13} gcm^{-3} it changes to $\gamma = 7/5$ where the gas becomes optically thick. Finally at densities greater than 10^{-7} gcm^{-3} it is set back to $\gamma = 1$ to model the dissociation of H_2. It is during this last isothermal regime that sinks are allowed to form.

5.3 Two-dimensional (PP) Clumpfinding

As discussed in Chapter 1, there have been a number of attempts to connect the structure of the gas in dense star-forming regions to the IMF. The majority of the work to date has produced results based on 2D maps of these regions, either using dust continuum emission (e.g Johnstone et al. 2006) or extinction mapping (e.g Lada et al. 2008) to obtain the column density distribution in the plane of the sky. As such, the clump-finding analysis shall first be carried out on position-position column density maps of the simulated molecular cloud. As shown by Pineda et al. (2009), clump-finding routines are very sensitive to the positions and

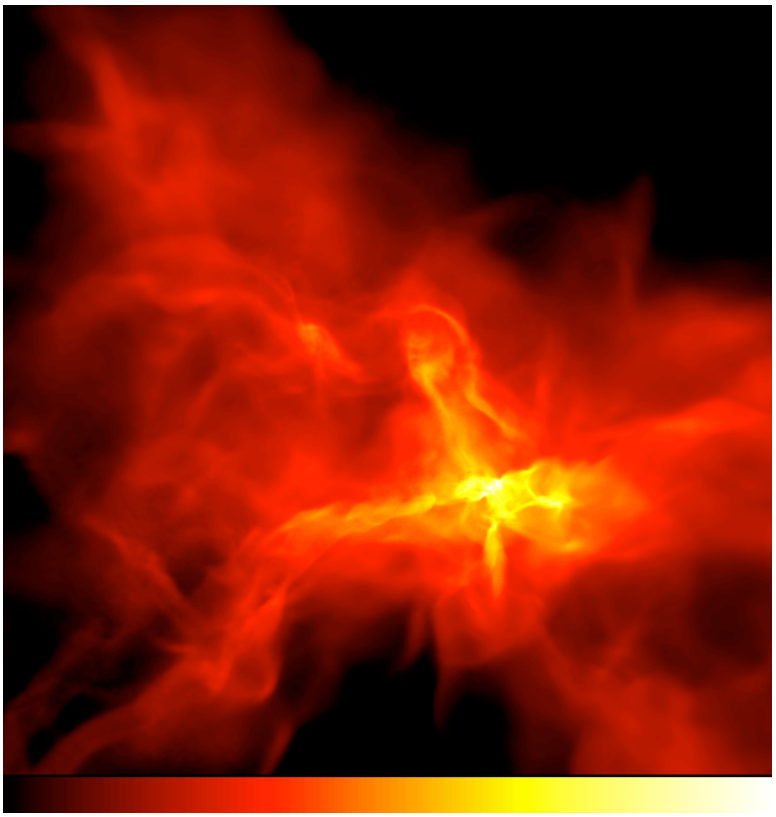

Figure 5.1: The column density of the data file used for the clumpfinding comparison. The density scale is logarithmic and runs from 0.005 gcm^{-2} (black) to 1 gcm^{-2} (white). The region shown is 1 pc by 1 pc large and contains 79.5 $M_{\odot}$.

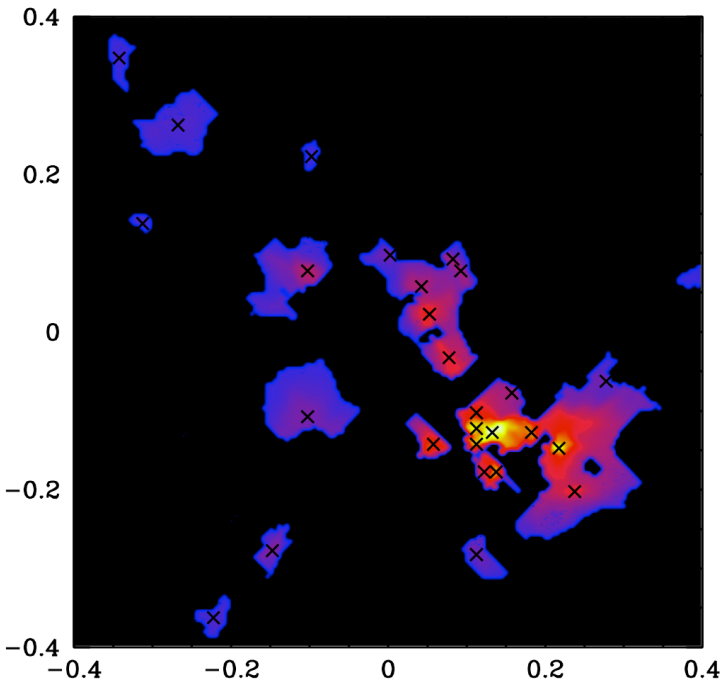

Figure 5.2: The standard PP clump-find projected in the xy plane, crosses denote the centre of the clumps. This clump-find used data from a 200 × 200 grid. The scale is shown in parsecs and the colours represent column densities in the range 0.02 gcm^{-2} (blue) to 1 gcm^{-2} (yellow) at logarithmic intervals.

number of contour levels so contour levels were kept static and a lower density sensitivity of 0.02 gcm^{-2} was set. The effect of varying the minimum density is considered in Section 5.4.

Figure 5.2 shows the PP clumpfind adopted as the standard to which comparisons will be made. The density is shown as a column density projection of the clumps after they have been background subtracted, the same scale is used as in Figure 6.1 for ease of comparison and to allow the clumps to be seen clearly, although no clump has a density lower than the minimum value of 0.02 gcm^{-2}. In the regions where no clump has been assigned the lowest colour on the density scale is used. Table 5.2 shows the parameters used to obtain the PP standard clumpfind.

5.3.1 Orientation

One of the key difficulties in interpreting the results of PP clump-finding is that a three dimensional structure has been arbitrarily projected into two dimensions, hence, it is unclear whether a clump is one object, or a superposition of several objects along the line of sight

Table 5.2: The parameters used to find the standard PP clumpfind shown in Figure 5.2. The resolutions grid cells correspond to a physical length of 1,031 AU.

Minimum Density	0.02 gcm^{-2}
Projection	xy plane
Resolution	200×200 grid cells
Spatial Resolution	1,031 AU
Density Countours	5 per magnitude

(Ballesteros-Paredes & Mac Low 2002). Figure 5.3 shows position along the line of sight and the real 3D density of the material contributing to a typical dense clump in the standard PP clump-find. The material is too widely distributed to be a single core. Moreover, some of this gas lies at densities (3D) which actually sufficiently preclude it belonging to any dense core.

Figure 5.4 shows that line of sight blending causes different clumps to be found if the three dimensional data set is projected along a different axes. In the x-y plane, which I consider in the next sub-section, 28 clumps are found, but in the x-z plane there are only 10. Table 5.3 shows that different orientations result in different clump properties. This is in agreement with previous work by Ostriker et al. (2001). The clumps found in each of my orthogonal projections are essentially independent of each other.

5.3.2 Resolution

The analysis of the PP clump-finding procedure next examines a fundamental difficulty in interpreting the observed clump properties: would the results differ if the observed cloud was further away? This problem is addressed by changing the resolution of the grid onto which the SPH data is interpolated. Perhaps unsurprisingly, it is found that the number of clumps identified in the data varies with the resolution of the grid. When the same physical region of the SPH data is interpolated to a grid with smaller elements, the clump-finding procedure yields more clumps. Figure 5.5 shows the clumps extracted in the x-y plane by the algorithm from four data grids of the following sizes, 50×50, 100×100, 200×200 and 400×400 grid cells . Table 5.4 shows the number of clumps found in each case and the spatial resolutions in physical units. Note that these resolutions are comparable to current observational surveys of nearby star-forming regions. Figure 5.6 shows the clump mass functions. To improve the statistics in Figure 5.6 clumps were found in each orthogonal projection at the relevant resolution and the data combined into one clump-mass function (this is only valid since in Section 5.3.1 it was found that the clumps in each projection were independent of each other).

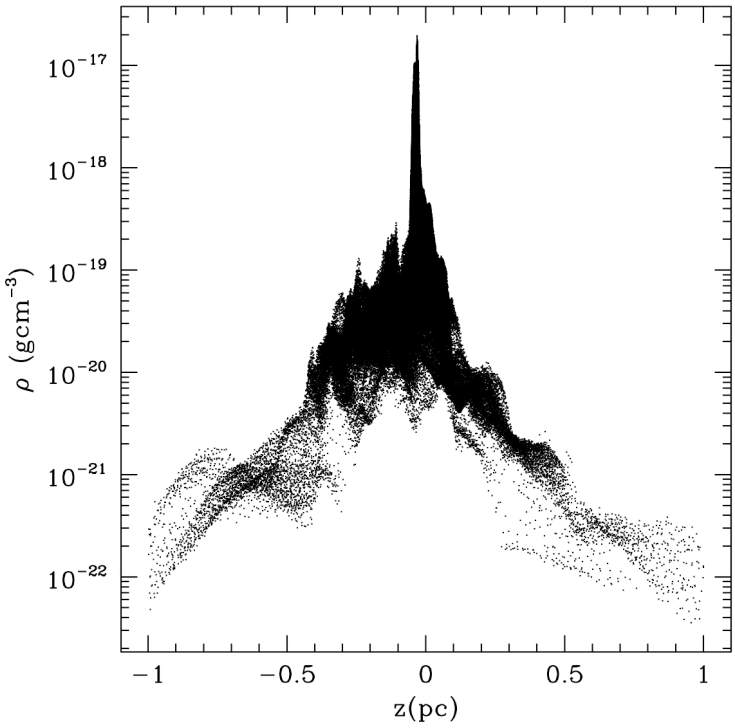

Figure 5.3: The intrinsic 3D density profile along the z axes of the material belonging to a typical clump in the standard PP clump-find. About half the material assigned to the clump is truly at high 3D densities but the rest is contamination from material along the line of sight.

Table 5.3: The properties of the clumps found in different orientations. The starred case corresponds to the standard PP clump-find.

Projection	No. Clumps	Total Mass ($M_\odot$)
xy *	28	16.35
xz	10	27.33

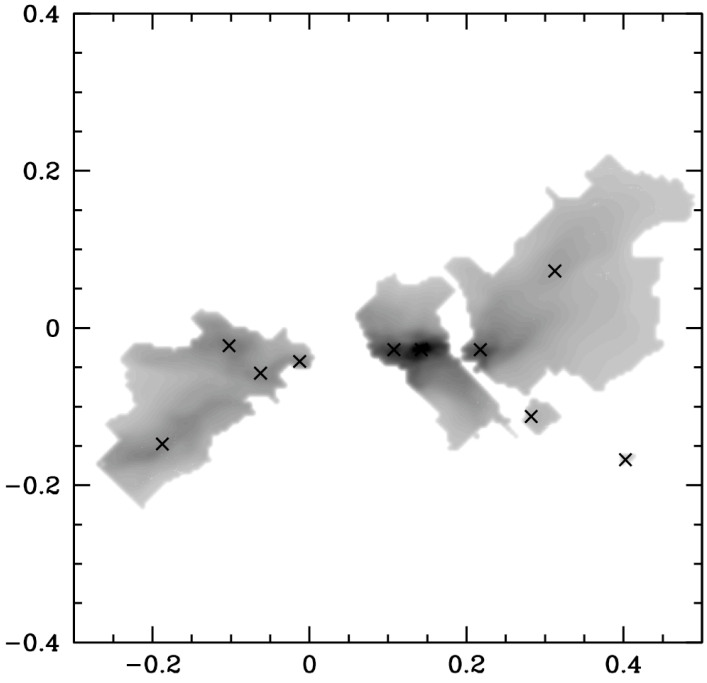

Figure 5.4: A clump-find with identical parameters to the standard PP clump-find carried out on the simulated data projected into the xz plane instead of the xy plane. The scale is shown in parsecs and the grayscale represent column densities in the range 0.02 gcm^{-2} (grey) to 1 gcm^{-2} (black) at logarithmic intervals. Crosses show the centre of the clumps

Table 5.4: The recovered clumps at different resolutions for clump-find on PP data in the x-y plane. The * denotes the fiducial case and the resolution is given in grid cells.

Resolution	Spatial Resolution	No. Clumps	Total Mass
50×50	4,125 AU	12	26.04 $M_\odot$
100×100	2,063 AU	17	18.62 $M_\odot$
200×200 *	1,031 AU	28	16.35 $M_\odot$
400×400	516 AU	31	15.71 $M_\odot$

As the resolution of the clump-finding input increases, more intermediate-mass are found as the biggest objects are broken into smaller units. This decreases the maximum mass in the CMF. Additionally, the break position between the two regimes decreases as the resolution increases due to the average mass of the clumps decreasing . The slope of the low and high mass ends do not appear to change significantly.

The amount of mass found in clumps decreases as the number of clumps and the resolution increases. There are two reasons for this. First, the higher resolution cases allows peaks in the structure that are blended at lower resolution to be resolved. Secondly, clumps are defined down to the lowest contour that is shared with a neighbour. As such, two newly resolved smaller clumps that were previously one larger clump, will have less mass than their larger counterpart. Note that in the standard CLUMPFIND algorithm, the total mass would be the same, since the clumps fill the entire surface/volume of the data grid. However a similar analysis performed with CLUMPFIND on observational data may still yield a similar result to that found here, since the background is usually subtracted before the clump-finding is applied.

5.3.3 Density Cut

The result of a clump-find is also dependent on the density range of the data-set. Figure 5.7 shows clump mass functions obtained from a basic PP data-set in the x-y plane with three different lower-density sensitivities. As the minimum density is lowered, eleven more clumps can be defined and a greater fraction of the structure is probed. With a restricted density range only the high mass end of the CMF is found. Then when the sensitivity is lowered further the CMF resembles two power laws.

If the PP data spans a narrower density range the resulting clumps are more distinct. Due to their decreased size, they contain less mass, in other words only the dense centers of the clumps are now included. The second panel of Figure 5.8 shows what the standard PP

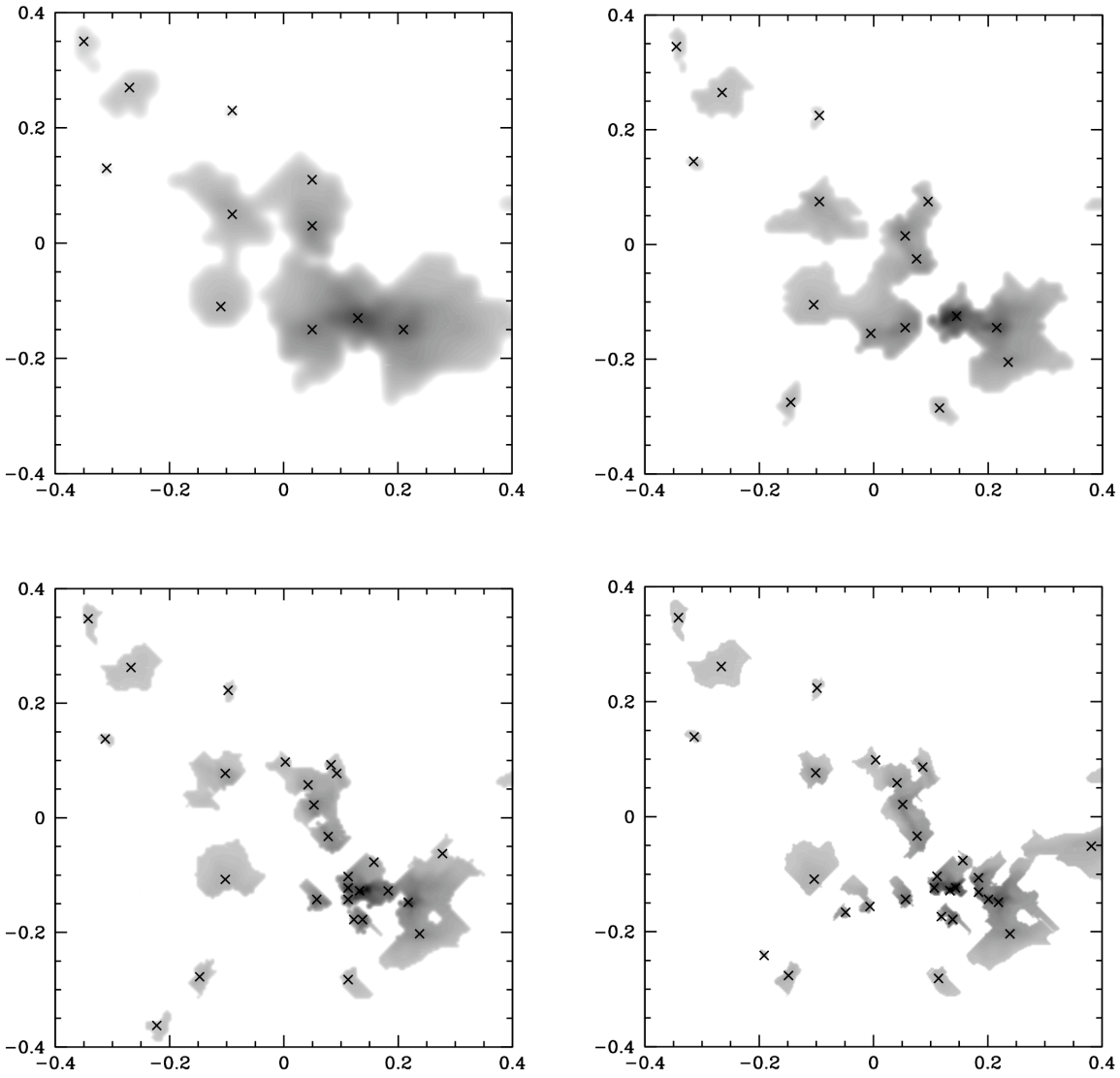

Figure 5.5: Four clumpfinds carried out on the central region where star formation will occur with varying resolution levels. *Top left* A 50×50 grid with a cell width of $4,125$ AU, *top right* a 100×100 grid with a cell width of $2,063$ AU, *bottom left* a 200×200 grid with a cell width of $1,031$ AU and *bottom right* a 400×400 grid with a cell width of 516 AU. The scale is shown in parsecs and the grayscale represent column densities in the range 0.02 gcm^{-2} (grey) to 1 gcm^{-2} (black) at logarithmic intervals. Crosses show the centre of the clumps. Note that in some cases a clump will disapear at higher resolution, this is primarily due to the shifting contours meaning that some clumps no longer meet the resolution criteria.

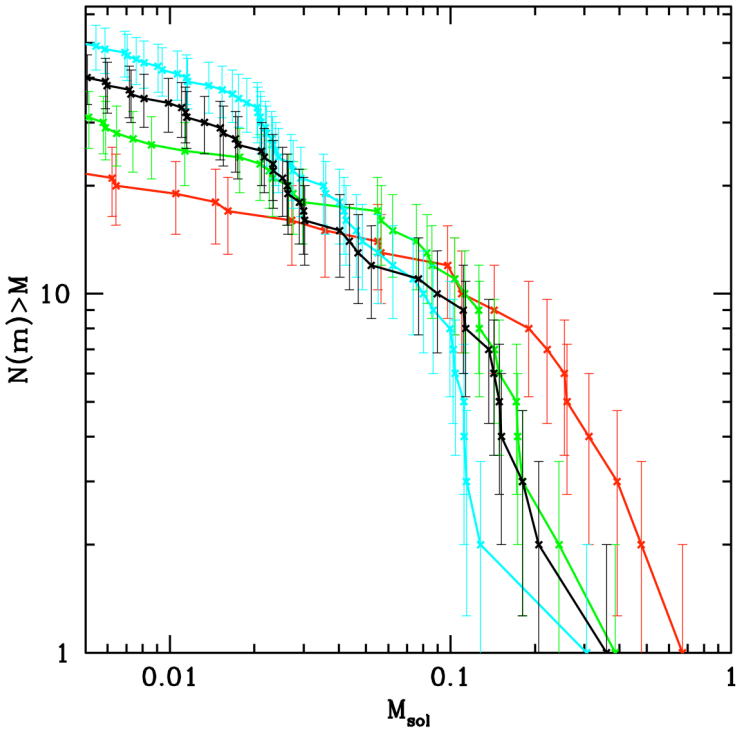

Figure 5.6: The variation of the cumulative number clump mass function with resolution. The clump-finds shown are from the *red* 50×50 grid with a cell width of $4,125$ AU, *green* 100×100 grid with a cell width of $2,063$ AU, the *black* 200×200 grid with a cell width of $1,031$ AU and the *blue* 400×400 grid with a cell width of 516 AU. Error bars depict the uncertainty from Poisson noise. Clumps from each orthogonal projection were included to improve the statistics.

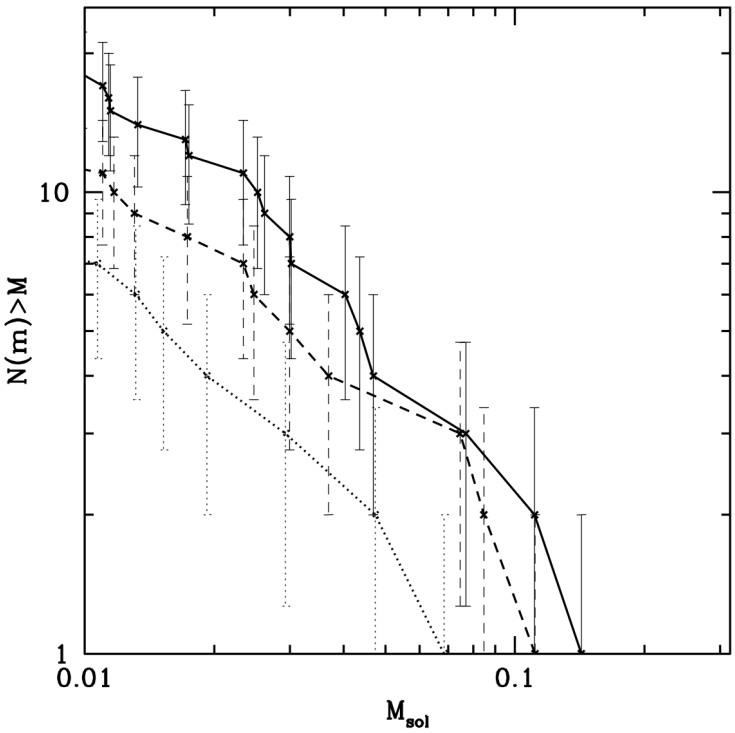

Figure 5.7: The cumulative number clump mass functions found from PP data with three different lower column density limits; *solid line* 0.01 gcm^{-2}, *dashed line* 0.05 gcm^{-2} and *dotted line* 0.1 gcm^{-2}. Error bars depict the uncertainty from Poisson noise.

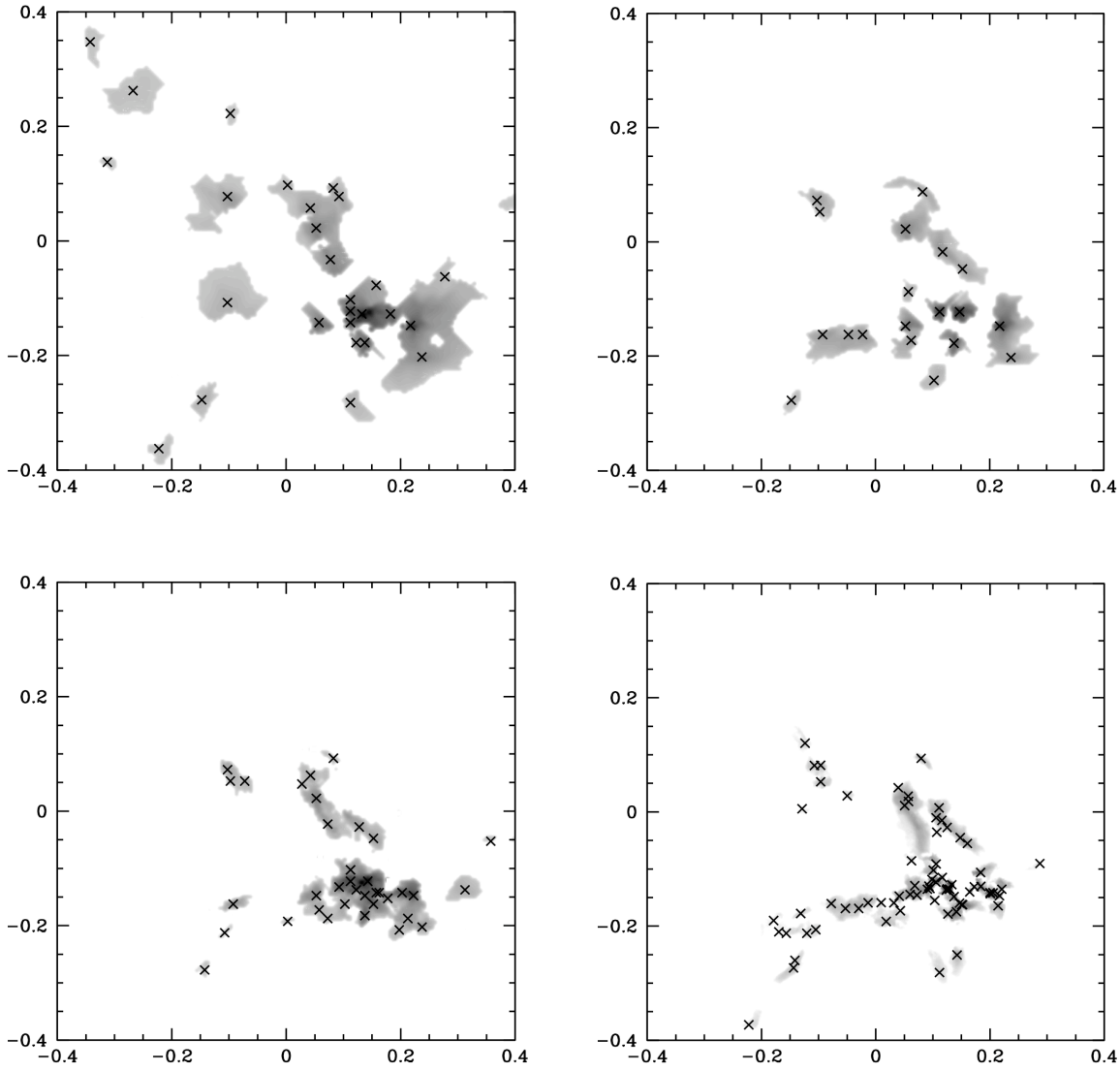

Figure 5.8: Clumpfinds using various data-sets.*Top left* the standard PP clump-find. *Top right* applied to a data set above an intrinsic 3D density of 10^4 cm^{-3}. *Bottom left* using the PPV data-set with 16 velocity bins, corresponding to a velocity resolution of 0.33 kms^{-1}. *Bottom right* the 3D clumpfind on the raw SPH data. The scale is shown in parsecs and the grayscale represent column densities in the range 0.02 gcm^{-2} (grey) to 1 gcm^{-2} (black) at logarithmic intervals. Crosses show the centre of the clumps.

clump-find becomes if applied to gas with a number density above 10^4 cm^2.

5.4 Position-Position-Velocity (PPV) clumpfinding

The second type of data set considered in this analysis is position-position column density maps with the radial velocity used as an additional dimension. This data set should suffer less

Table 5.5: The properties of the clumps using the PPV data-set compared to the standard PP clumpfind. The 16 velocity bins have a width of 0.33 kms^{-1} and the 40 velocity bins a width of 0.13 kms^{-1}

Velocity Bins	Resolution	No. Clumps	Total Mass
0∗	–	30	16.37 $M_\odot$
16	0.33 kms^{-1}	37	8.90 $M_\odot$
40	0.13 kms^{-1}	33	4.50 $M_\odot$

from line of sight blending as it is likely that different clumps will be travelling at different velocities. The width of the velocity channels used determine the velocity resolution of the clumpfind, 16 velocity bins are assigned along the z-axes of the data cube which corresponds to a resolution of 0.33 kms^{-1}. These values are arbitrarily chosen to probe the effect of increased velocity resolution. Due to the increased number of grid cells a PPV clumpfind uses, it has an intrinsically higher resolution than a PP clumpfind. Panel three of Figure 5.8 shows the PPV clumpfind, and Table 5.5 compares its properties to the standard PP case and to an additional PPV case with 40 velocity bins.

In the PPV case, clump masses are reduced as material previously included is rejected due to its velocity. The positions and extent of the clumps also change relative to the PP clumpfind. Changing the size of the velocity bins also changes the mass and number of clumps found. In the case shown here, when the bin size is decreased and hence the resolution is increased, there is less mass assigned to the clumps. A side effect of this process is that some of the clumps masses decrease to the point that they no longer meet the resolution requirement and are therefore not included in the analysis.

As regards blending, for the clumps found using the PP method shown in Figure 5.3, Figure 5.9 shows that more of the mass is now contained in a smaller region. However, the density profile suggests that the clump found still contains spurious material that happens to be moving towards the centre of the region with a similar velocity. Nonetheless, the contribution from material at low density along the line of sight has been reduced.

It should be noted that the analysis presented here for the PPV method is a 'best case scenario' as no molecular tracer can actually probe the entire line of sight from the low density outer layers to the dense core centre. This means that the velocity information is likely to be incomplete. Further, temperature gradients in the core centres will also affect the line profiles. An additional caveat of the PPV method is that if the clump is undergoing collapse or expansion then it could be split into two objects depending on the velocity resolution. However this is still a useful observational technique, particularly when using multiple molecular tracers

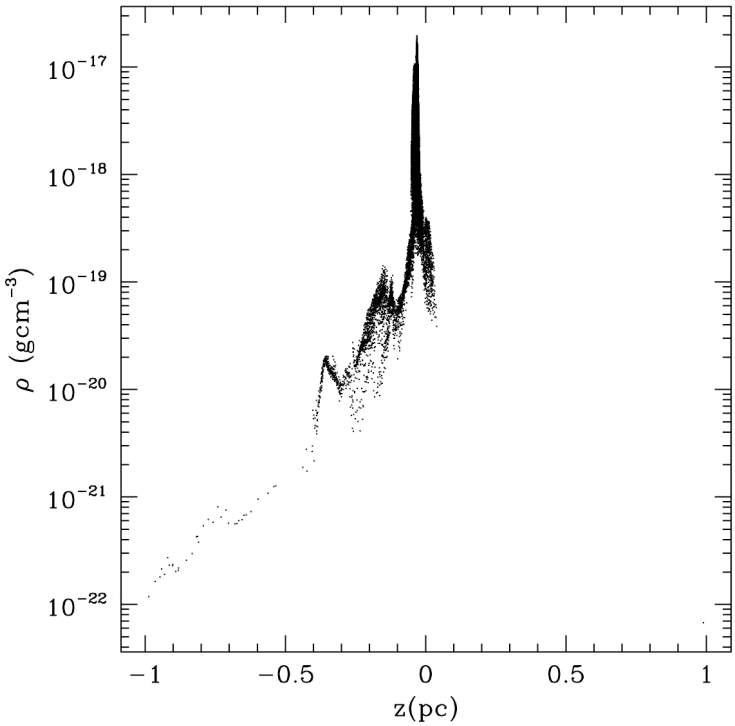

Figure 5.9: A projection of the real 3D density profile of the clump shown in Fig 5.3 when found using PPV data with 16 velocity bins instead of just PP data.

(e.g. André et al. 2007).

5.5 Three-dimensional (PPP/SPH) clumpfinding

The final data set considered is that of the full simulated three-dimensional structure. While this is impossible from observations, it is still a useful comparison as the true structure of star forming regions is, of course, three-dimensional. The same basic method is used to find the clumps as before but it has been modified as shown in Chapter 4.

However, unlike the PP and PPV clump-finds the resolution is no longer simply the size a grid. As Chapter 2 described, in SPH the mass resolution varies spatially, high density regions are better resolved than low ones, therefore the three dimensional clumpfind also shares this property. This effectively results in the SPH run having the highest resolution of all the clumpfinding methods.

The bottom right panel of Fig. 5.8 shows the result of the clump-find on the 3D SPH data. The number of clumps has increased, and the total mass decreased relative to the previous results. There are two reasons for this. First, due to the improved resolution the number

Table 5.6: A comparison of the clump-find results.

Method	No. Clumps	Total Mass ($M_\odot$)
PP	28	16.35
PP high density	19	10.51
PPV 16 bins	37	8.90
sph	72	4.50

of clumps increases as shown in Section 5.3.2. Secondly the use of 3D data eliminates the blending along the line of sight previously encountered in Section 5.3.1 so more clumps are found with smaller masses. Effectively a finer level of structure than in the previous data-sets is now being detected, namely the very dense core centers.

5.6 Discussion of Global Properties

5.6.1 The Clumps

Table 5.6 compares the properties of the clump-finds. Although the general outline of the dense region where the clumps are identified remains constant, the number, masses and assigned boundaries of the clumps varies with extraction method. Generally the number of clumps increases and the total mass found in clumps decreases with the precision of the method.

Applying a density cut to a data-set produces more distinct clumps, but is of course completely arbitrary. The PPV clump distribution is a better match to the high-resolution 3D clumpfind than the PP clumps. The peak positions identified as the heads of clumps from the PPV data correlates well with the highest density structures seen in the sph case. The overall mass distribution and the clump properties, however, differ. Each data-set appears to highlight a different scale of the structure within the simulation.

Defining the clump boundaries is further complicated by arbitrary decisions that have to be made in the clumpfinding process. Is there a minimum density required for a clump? How many density contour levels need to be set? Should some minimum contrast to the background be required? All these issues add to the difficulties presented here in comparing clumps found from different data-sets. These challenges should be kept in mind when comparing the properties of cores recorded in the literature, particularly when contrasting masses and sizes.

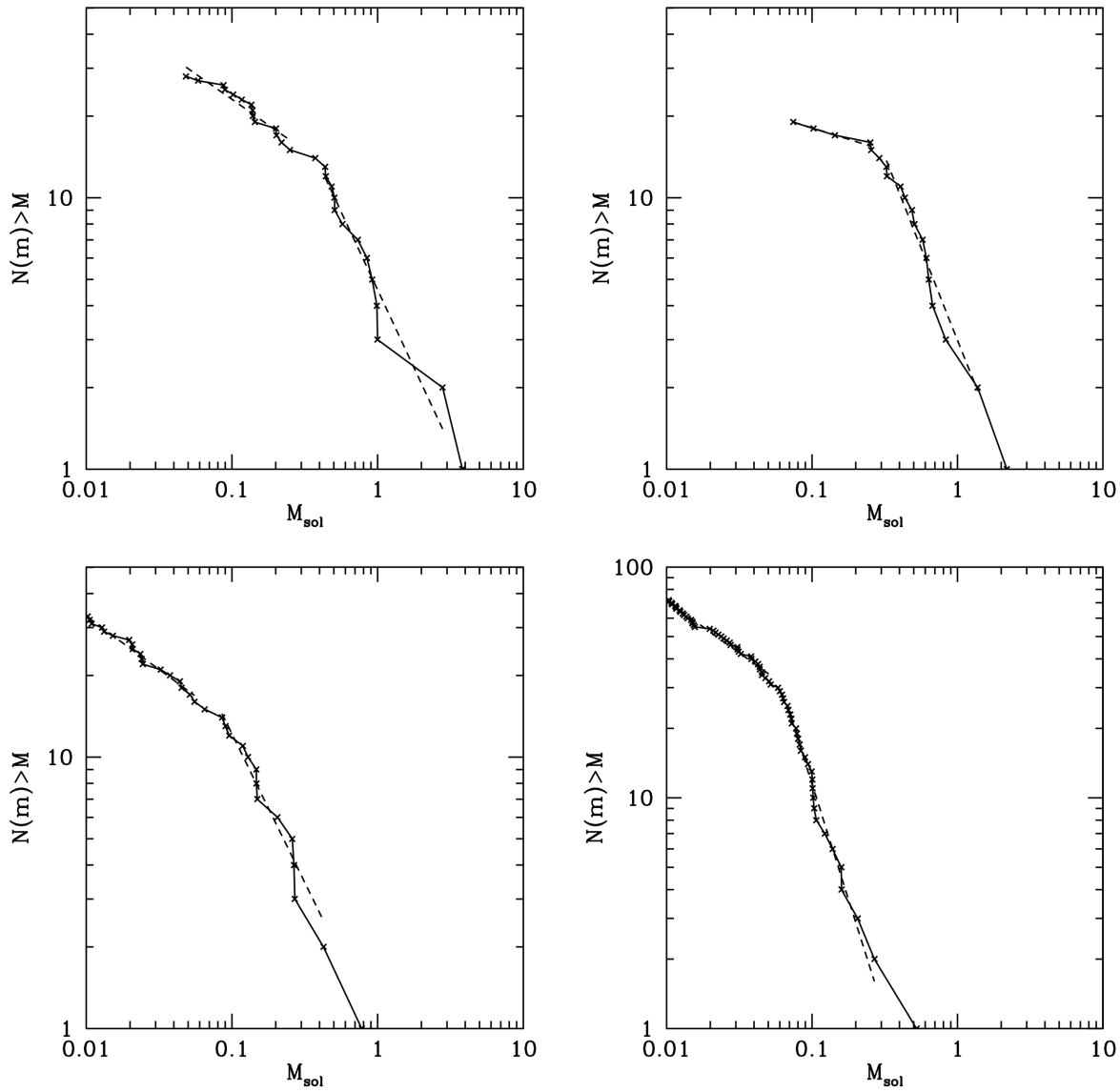

Figure 5.10: The cumulative number clump mass functions from the previous clumpfinds. *Top left* the standard PP clump-find, *top right* high density PP data, *bottom left* the PPV clump-find and *bottom right* the PPP (SPH) method. The dashed lines are power law fits whose gradients are shown in Table 5.7.

5.6.2 The Clump Mass Function

Despite the differences in the clump properties, the clump mass functions have similarities in their shapes, although their absolute values and breakpoints differ. Figure 5.10 shows the cumulative clump mass functions derived from the PP, PP with density cut, PPV and PPP (SPH) clump-finds and Table 5.7 shows the gradients of the power laws which best fit them.

As the clump properties differ each of the CMF's has a different magnitude, size range and break point but the overall shape is always broadly consistent with the stellar initial mass

Table 5.7: The best fit power law gradients for the cumulative CMF's shown in Figure 5.10.

Method	Break Point	Low Mass Gradient	High Mass Gradient
PP	$0.3\,M_\odot$	-0.37	-1.15
PP high density	$0.3\,M_\odot$	-0.16	-1.35
PPV 16 bins	$0.09\,M_\odot$	-0.39	-1.10
sph	$0.06\,M_\odot$	-0.45	-1.99

function (Kroupa, 2002). When plotted logarithmically this corresponds to a Saltpeter slope of $\Gamma = -1.3$ with a break to second power law of $\Gamma = -0.3$ at lower masses.

At the low mass end, with the exception of the PP high density case, all the gradients are within 0.15 of the Kroupa value and within 0.08 of each other. The PP case where the density range was restricted to high values resulted in incomplete sampling of the low-mass end, which leads to a flattening of the low-mass gradient. At the high mass end the two-dimensional methods have gradients within 0.25 of each other, Poisson noise makes these fits more uncertain but the agreement is still good. The best fit to the high mass end of the SPH cumulative clumps mass function, however, is steeper than the two dimensional cases. It is unclear whether this is a genuine consequence of the 3D data set or due to the increasing resolution of the SPH method with density preferentially identifying smaller denser structures.

Further evidence that the CMF may have a universal shape can be seen in the earlier discussions of resolution (Figure 5.6) and density range (Figure 5.7). Once again, although the properties of the clumps are changing, the profile of the CMF remains broadly consistent with the stellar IMF.

These results suggest that the shape of the CMF found in this simulation resulted naturally from breaking up the underlying structure of a molecular cloud in an automated manner. Therefore, the emergence of a rational CMF from a data set is no guarantee that the identified clumps are unique objects. The structure could have been divided up using a differing, perfectly justifiable, method which results in different clump positions and sizes but yields a similar CMF profile. This is reminiscent of the observations discussed in the introduction, all have similar CMFs but the characteristic masses of clumps differ. Indeed, due to difficulties like those discussed here, Rosolowsky et al. (2008) has proposed that dendrograms might ultimately prove a better way to identify structure than the traditional clumps. Still, many of the issues raised here are likely to be relevant using dendrograms or any other clump finding algorithm.

5.6.3 Universality of the CMF

Despite variations in clump properties, the slope of the clump mass function is similar in all the cases investigated here, with the possible exception of the high mass end in the SPH clump mass function. The CMF retains this shape when extracted using different clump-finding methods and parameters.

As many studies have shown (e.g. Vazquez-Semadeni & Gazol 1995; Ballesteros-Paredes et al. 1999b; Klessen 2001), turbulence generates the characteristic multi-scalar structure of molecular clouds. Elmegreen (2002) goes so far as to describe the structure of the interstellar medium as a continuous fractal distribution. Observationally, Padoan et al. (2003) show that the structure of the Taurus and Perseus molecular clouds is hierarchical at scales of $0.3-3$ pc. Given the universality of turbulence (Heyer & Brunt, 2004), it is perhaps unsurprising that the observed CMFs exhibit similarities between different star forming regions, and there exists in the literature a number of models for describing how these clumps can form (Fleck, 1982; Elmegreen, 1993; Padoan, 1995; Padoan, Nordlund, & Jones, 1997; Myers, 2000; Klessen, 2001; Padoan & Nordlund, 2002). The similarities between the CMF and the IMF then naturally leads to the suggestion that the two are related (Motte, Andre, & Neri, 1998; Lada, Muench, Rathborne, Alves, & Lombardi, 2008; Myers, 2008).

However, these findings suggest that the mapping between the CMF and IMF is not straightforward. Analysing fractal-like structure with any clump-finding algorithm will generate a clump mass function. The details of the clump properties, especially the mass, will depend on the type of algorithm and the parameters chosen. Further, the clumps are not uniquely defined. This has also been found observationally. Johnstone et al. (2000) and Motte et al. (1998) both surveyed the ρ Ophiuchi and derived clump mass functions which were in agreement with each other. However, as Johnstone et al. (2000) comment, the masses, numbers and positions of the clumps found do not correspond between the surveys. Due to the variance of clump properties with identification method, it is unclear how best to link star-less cores to protostars in a quantitative manner.

5.7 Conclusions

It has been shown that when a CLUMPFIND style algorithm is applied to different types of data-sets from the same underlying simulation, clump characteristics vary. This is due to a

number of factors. Details of the observational maps or the simulation obviously play their part, particularly parameters such as resolution, orientation and density range. The more levels of structure resolved within a data-set the greater the number of clumps that can be found. Blending of structure along the line of sight decreases the number of clumps found in 2D clumpfinds and increases clumps masses. A significant amount of material which is in reality not connected to a high density core can be artificially included. Applying a high density cut to PP data yields more distinct objects but can bias the resulting mass function.

Using velocity as a third dimension improves accuracy and provides a closer match to the true 3D structure than just using PP data. The clump boundaries, however, still differ and less mass is assigned to clumps.

Qualitatively the profile of the clump mass function always resembles the Stellar IMF, regardless of the data-set used. However, the quantitative values of the CMF are dependent on the extraction method, and therefore causal comparisons to the IMF should be made with caution.

6

The Earliest Fragmentation in Molecular Clouds

In the previous chapter clump properties were found to be unreliable. This makes it difficult to investigate the link between the dense cores of gas and the stars which form from them. In this chapter the potential clumpfinding algorithm introduced in Chapter 4 is used to identify bound pre-stellar cores. These 'p-cores' represent the first bound fragments in molecular clouds, and by tracing their evolution, the link between the core mass function and the stellar IMF can be probed directly. For the rest of this work, the term 'core' represents a small scale object, and the term 'clump' represents a larger scale object, as introduced in Chapter 1

6.1 Fragmentation and the IMF

As outlined in Chapter 1, the origin of the stellar initial mass function (IMF) has been a major question in star formation since it was first measured by Salpeter (1955). The similarities between the IMF and the mass function of clumpy structure in molecular clouds (MC's), has led many to propose a link between the two (e.g. Motte et al., 1998). In this scenario, stars are formed directly from the dense cores of gas observed in molecular clouds (e.g. Johnstone

et al., 2000; Testi & Sargent, 1998; Johnstone et al., 2006; Nutter & Ward-Thompson, 2007; Enoch et al., 2008). A direct link between the core mass and the resulting stellar systems mass is often assumed. For example Alves et al. (2007) propose an efficiency of one third between core mass and stellar system mass.

This fits into the the long-standing idea that fragmentation of molecular cloud structure forms the IMF. This could be simply due to gravity (Larson, 1973a; Elmegreen & Mathieu, 1983), causing successive fragmentation of a larger body as it collapses. Alternatively, it has been shown that the supersonic turbulence observed in MC's produces a hierarchical density structure, the dense peaks of which have a mass distribution similar to the IMF (Henriksen, 1986; Larson, 1992; Elmegreen, 1997; Klessen, 2001; Padoan & Nordlund, 2002; Hennebelle & Chabrier, 2008) .

However, it is unclear how to get to the IMF from the clump mass function. Many assume a direct $1-1$ link between the masses (Motte et al., 1998; Padoan & Nordlund, 2002; Alves et al., 2007), while others include the effects of multiplicity (Goodwin et al., 2008). However, there are many complicating factors in this story of collapse, such as feedback from winds and outflows (Shu et al., 1988; Silk, 1995; Myers, 2008), supporting magnetic fields (Heitsch et al., 2001; Tilley & Pudritz, 2007) and competitive accretion (Zinnecker, 1982; Bonnell & Bate, 2006). All of these processes are involved in the collapse of a fragment to a star and all could vary locally. In fact, Swift & Williams (2008) have shown that when a core mass function is evolved into a stellar IMF, a Salpeter like distribution was found regardless of whether the core-to-star efficiency was constant, variable or included multiplicity. Moreover, under the competitive accretion theory of star formation there is no need for a direct correlation between core masses and stellar masses at all, as the cores can be thought of as 'seeds' from which accretion will build up the future IMF (Clark & Bonnell, 2005).

Resolving the issue of core evolution is further complicated as their lifetimes are not well known. In the classical Shu (1977) picture a quasi-static core supported by its magnetic field will slowly collapse to form a star. However, in the more dynamical view, usually proposed in gravoturbulent fragmentation, cores can collapse quickly when they become unstable, making the process hard to observe. Further, the variation of core free-fall time with density means that the clump mass function observed at a snap shot in time might actually evolve into a steeper IMF (Clark et al., 2007).

Massive star formation poses another question for the evolution of cores. Any core which is large enough to form a massive star directly is likely to fragment without some additional heating mechanism. McKee & Tan (2003) theorize that massive cores could be supported by their internal turbulent energy, although simulations have shown that some fragmentation is unavoidable (Krumholz et al., 2007; Dobbs et al., 2005). Alternatively competitive accretion predicts that there will be no massive cores that do not fragment into smaller structures. It would be one of these smaller cores which would preferentially accrete from its environment to become a massive star (Bonnell et al., 2004). In this case, the link between core mass and stellar mass is destroyed by accretion.

Observationally it is hard to be sure which structures will gravitationally decouple from their environment and are hence 'pre-stellar' in nature (i.e. will form stars in their future). Observations of molecular tracers such as CO produce a core mass function resembling the IMF (e.g. Ikeda et al., 2007). However, these tracers are insensitive to the densest gas. As Lada (1992) has shown, star formation generally takes place above a density of $n > 10^4$ cm^{-3}. Observations of CO cores are typically more massive and on larger scales (e.g. Tachihara et al., 2002) than mm-continuum cores which trace denser gas, (e.g. Motte et al., 1998; Johnstone et al., 2000). Moreover, it is often difficult to define a 'core' from the data, without invoking a somewhat arbitrary boundary (e.g. Padoan et al., 2006; Pineda et al., 2008; Schnee et al., 2008). In the previous chapter it was demonstrated that core properties are extremely sensitive to the core boundaries, which in turn depend on the resolution, density range and dimensionality of the dataset. High resolution observations of dense gas in nearby molecular clouds are the most likely to find pre-stellar objects, for example those identified from a synthesis and re-analysis of the literature in Ophiuchus by Simpson et al. (2008). However, these observations still suffer from a lack of completeness, and of course all observations are necessarily at a snap-shot in time and identify cores in a variety of evolutionary states with no guarantee that they will form stars.

In this chapter I seek to determine the relation between the properties of the cores formed through the fragmentation of molecular clouds and the 'stars' which form from them. In a SPH simulation of a molecular cloud bound pre-stellar cores are identified with well defined boundaries from a complete data-set without time effects. The cores evolution are traced from when first bound through to their early evolution towards stars. Section 6.2 outlines the initial conditions of the simulation, and Section 6.3 discusses how the cores are defined

Table 6.1: Given below are the initial conditions of the simulation analysed in this paper. The mass resolution is the minimum mass gravitational forces can be resolved for and is calculated via $M_{res} \sim 100 M_{total}/N_{part}$.

Size	$3 \times 3 \times 10$ pc
Mass	10^4 $M_\odot$
Particles	5.5×10^6
Mass resolution	0.18 $M_\odot$
Dynamical time	4.74×10^5 yrs

using the potential clumpfinding algorithm introduced in Chapter 4. In Section 6.4 the p-core properties are calculated and compared to observations. The core mass function is also found. In Section 6.5 the p-core masses when they are first bound are linked to the mass which will be accreted by the stars (sink particles). Finally in Section 6.6 the results are discussed.

6.2 The Simulation

The initial conditions of the simulation used for this Chapter, consisted of a cylinder containing 10^4 $M_\odot$ concentrated at one end so the top was over-bound and the bottom under-bound. A turbulent velocity grid, consistent with a Larson velocity dispersion of $\sigma \propto r^{0.5}$, was generated according to Dubinski et al. (1995) and Myers & Gammie (1999) and interpolated onto the SPH particles. The magnitude of the turbulent velocities is chosen such that globally the cloud is initially supported by turbulence, which equates to a r.m.s. velocity of 4.7 kms^{-1}. The turbulence is not driven but additional kinetic energy is released by the gravitational collapse of the MC; when the simulation was terminated the r.m.s. velocity had decayed to 3.65 kms^{-1}.

Table 6.1 shows the properties of the simulation. The cloud is modelled with 5.5×10^6 SPH particles, which gives a mass resolution of 0.18 $M_\odot$ (Bate & Burkert, 1997). The simulation was run on the SUPA Altix computer at the University of St Andrews.

The barotropic equation of state introduced in Chapter 2 is used for basic heating and cooling to ensure that the Jeans mass at the point of fragmentation matches the characteristic stellar mass. This equation of state becomes isothermal again at $\rho_3 = 2 \times 10^{-13}$ gcm^{-3}, to allow sink particles to form, as it is required that the fragments from which they form are both bound and collapsing. Therefore in this simulation, sink particles are not created until at least a density of $\rho_3 = 2 \times 10^{-13}$ gcm^{-3} has been reached. Sink particles will accrete bound material within a radius of 200 AU, and have their mutual gravitational interactions smoothed

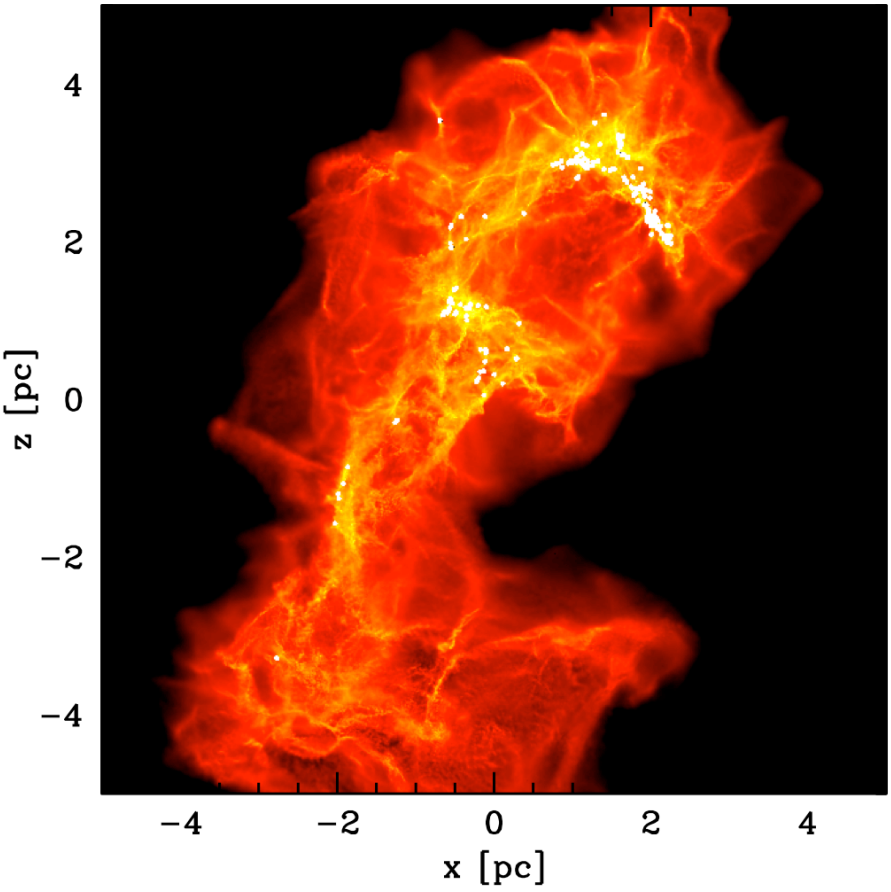

Figure 6.1: The simulated Giant Molecular Cloud at one dynamical time. The colours represent column densities in the range 0.001gcm^{-2} (red) to 10 gcm^{-2} (white). Sink particles are shown as white dots and the cloud is viewed along its long axis.

to 40 AU.

The simulation evolves with self gravity until just after a dynamical time it is as shown in Figure 6.1. The simulation is terminated at 1.4 t_{dyn}, at which point there are 949 sink particles which have a combined mass of 1249 $M_{\odot}$. This equates to a star formation efficiency of 12.5%.

6.3 Clump Finding using Potential

As previously shown in Chapter 5 (Smith et al., 2008), clump mass functions always retain a common shape, but the sizes, masses and positions of cores vary with the method of extraction. This behaviour is also seen in observations. Motte et al. (1998) and Johnstone et al. (2000) in their observations of ρ Ophiuchus find similar clump mass functions but the po-

sitions of their clumps and their masses do not correspond with each other. As the density distribution of molecular clouds is hierarchical with structure on all scales it is unclear which scale is the most relevant for star formation.

In this Chapter, I take a different approach, since I am interested in establishing the connection between the mass of the fragment as it first becomes bound and the final mass of the sink particle that forms from it. Rather than breaking the cloud up into structures defined by density, gravitational potential wells are found instead. There are two advantages to such a method. First, the gravitational potential distribution in the cloud is considerably smoother than the density distribution, since density fluctuations that do not carry sufficient mass cannot significantly contribute to potential field. Second, the strength of the gravitational potential determines whether a clump will collapse and how mass will flow. In a density distribution it is unclear which scale of the structure is important, whereas with potential the scale at which structures are bound is a clear physical quantity. Naturally, there is a disadvantage to this process: it becomes difficult to compare the structures to those observed in molecular clouds. However it is expected that some properties may be comparable between the observed objects and those which are extracted from the simulation in this study. These are discussed in Section 6.4.

Potential cores (p-cores) are identified using the algorithm described in Chapter 4. They represent the local potential minimum below the surrounding background and therefore explicitly include tidal effects. Figure 6.2 shows an example of the potential clumps found from the central region of Figure 6.1. As the structures identified by the potential clump find are typically small, they are called 'p-cores'. Note that there is no intrinsic requirement that a p-core is bound, as it may have sufficient internal energy (both thermal and kinetic) to prevent collapse. Once the p-cores form sinks, only the total sink mass formed from them is traced, because the spike in potential due to the sink particle may distort the boundaries; therefore all the p-cores are starless.

The major aim of this chapter is to investigate the link between pre-stellar p-cores and the stars formed from them. In order to do this two data-sets are used, the first of which is the 'composite' data-set. P-cores are found at 0.1 dynamical time ($t_{dyn} = 4.7 \times 10^5$ yrs) intervals between 0.6 t_{dyn} when star formation had just begun and 1.4 t_{dyn} when the simulation was terminated. Snapshots from each time are combined into one data-set, which removes any

time dependent effects and increases the number of objects within the data-set. The cores in the composite data-set have an average dynamical time of 7.4×10^4 yrs meaning that a few long lived, non-transient cores will be included twice, but at different evolutionary states. In total there are 573 p-cores which should be enough for good statistics. The composite data-set represents the view of cores in a molecular cloud at single points in time. It contains p-cores at different evolutionary states, with different levels of binding, many of which are transient.

The second data-set is the 'bound' data-set, which contains the details of the p-cores at the point they first became bound. The p-cores are traced throughout the lifetime of the simulation, and if more than 80% of the mass belonging to a p-core remains grouped together in the next simulation snapshot, the p-core is said to survive. The binding is traced throughout the p-core lifetime, and at the point where $E_{rat} > 1$ for the first time its properties are recorded. E_{rat} is defined as:

$$E_{rat} = \frac{|E_p|}{E_{therm} + E_k} \tag{6.1}$$

where E_k is the kinetic energy calculated with respect to the center of velocity of the clump, E_{therm} is the thermal energy of the clump and E_p is the potential energy of the clump calculated using the relative depth of the potential well once the background has been subtracted. Hence the clumps identified here are bound with respect to the environment in which they are formed, not merely when considered in isolation. This means that tidal forces from surrounding cores are taken into account when determining whether the p-core is bound. As the bound p-cores are identified throughout the simulation this data-set is also time independent. Due to this data-set being a synthesis over time and the p-cores being identified using a quantity impossible to observe, these objects could not be found observationally. Despite this, the analysis is worthwhile as the bound data-set allows us to identify the fragmentation scale of the molecular cloud. The sink particles form when these bound cores collapse. In total there are 306 bound cores in the simulation which is less than the number in the composite data-set but should still be enough for good statistics.

6.4 Physical Properties of the Potential Cores

Unfortunately, a potential core can only be identified when positions and velocities are known in three dimensions, which is impossible observationally. Therefore, the properties of the p-cores are now calculated to allow a comparison to observational data. The average properties

are shown in Table 6.3.

6.4.1 P-core Shapes

Figure 6.2 shows a close up view of the p-cores identified at a snapshot in time in one of the clustered regions of the molecular cloud. The p-cores are only quasi-spherical and often are elongated due to the filaments they are formed in. Within the p-cores there is still significant density substructure, and further fragmentation is often observed after the p-core is first bound. Due to this substructure, a traditional clumpfinding algorithm would have split them into smaller cores.

In order to quantify the extent of the p-cores, an effective radii, r_{eff} is used, within which 68% of the mass is contained. As the p-cores are not relaxed, the peak in the gravitational potential is used to define the centre rather than the centre of mass, which produces smoother density profiles. Figure 6.3 shows the density of the sph particles assigned to a typical p-core, plotted against their distance, r, from the central potential peak. The large dispersion shown in the density profile is due to the substructure within the core and the effect of the cloud being embedded in a non-uniform medium.

Nonetheless despite the scatter there is a trend towards a flattened density profile in the central region, as has been seen in observations (e.g Ward-Thompson et al., 1994). To get an idea of how centrally concentrated the p-cores were, a power law of the form $\rho \propto r^{-n}$ was fitted to the p-core and the best fit value of n determined. I excluded the radius within which the first 10 % of the mass was contained from the fit due to the aforementioned flattening.

Due to the dispersion from the density substructure and the core's non-spherical nature, there was a large degree of uncertainty, often as large as 50%. Despite this uncertainty, when plotted as a histogram Figure 6.4 (c), it is found that the bound cores have exponents clustered around $n = 1.36 \pm 0.35$. This is intermediate between a shallow density increase ($n = 1$) and that of a free-falling envelope ($n = 1.5$), and is an indication that the p-cores are still being formed when they become bound. Typically exponents of $n \approx 1.6$ are expected for Class 0 and Class 1 YSO's (Young et al., 2003) . Conversely, the profiles of the composite p-cores have a wide range of density exponents with an average value of 1.08.

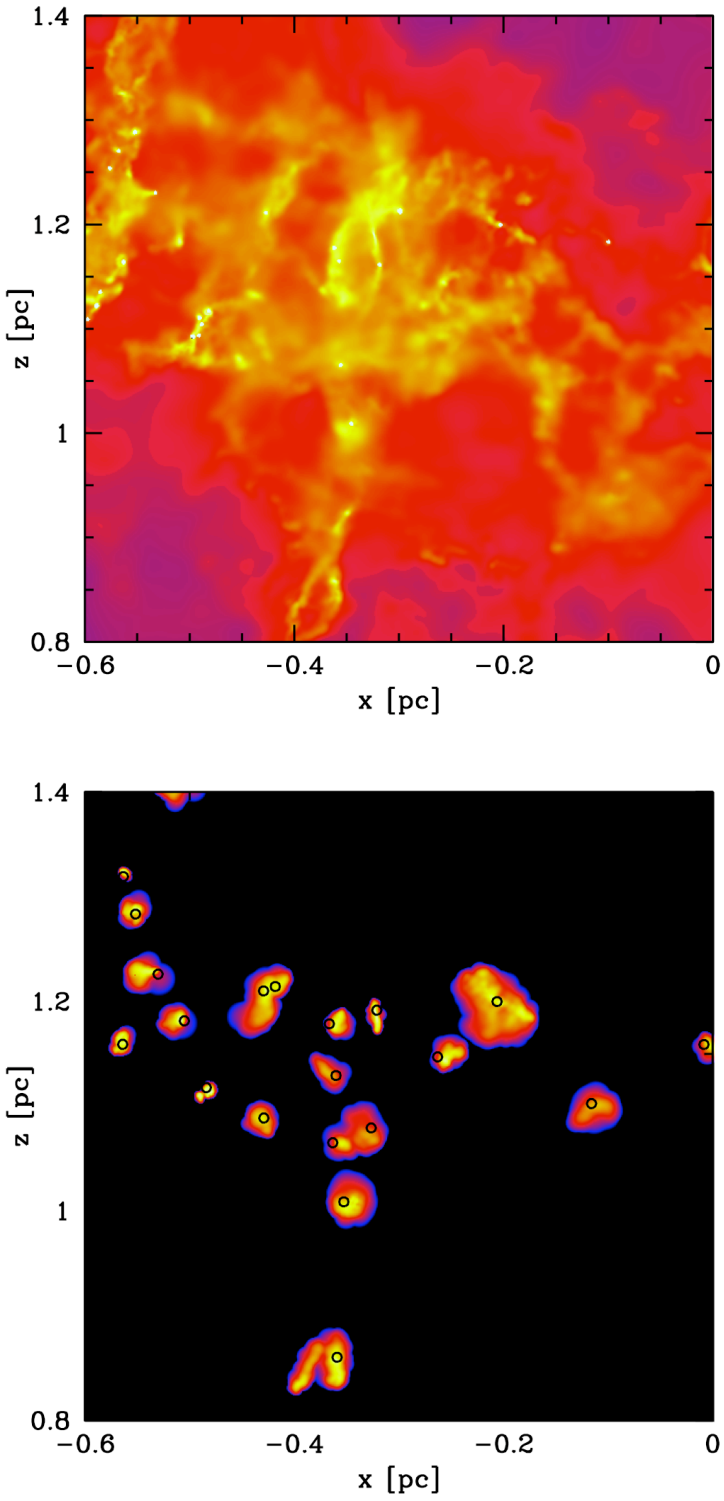

Figure 6.2: A close up view of some of the pre-stellar pcores identified from Figure 6.1. The top panel shows a zoom of a clustered region in column density and the bottom panel shows the pre-stellar p-cores identified in it. Colours depict column density and the scale runs from 0.001 gcm^{-2} (blue) to 10 gcm^{-2} (yellow). The location of the potential peak of the twenty p-cores in this region are shown by hollow circles. The p-cores are only quasi-spherical and exhibit significant substructure.

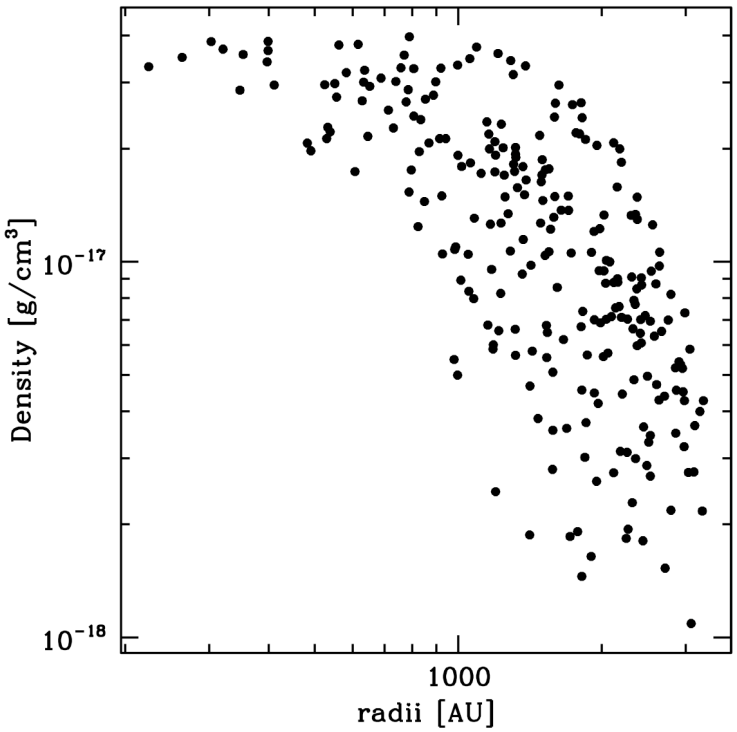

Figure 6.3: The density of the sph particles assigned to a typical p-core plotted radially outward from the peak of gravitational potential. There is considerable dispersion due to substructure, but there is a clear trend showing a flattened central peak and density decreasing outwards.

Table 6.2: The average clump properties of the p-cores in the bound and composite datasets. R_{eff} is the radius within which 68% of the mass is contained. The density profile is the best fit value of n for the profile $\rho \propto r^{-n}$

	Bound	Composite
Mass ($M_\odot$)	0.70	0.78
R_{eff} (AU)	2.4×10^3	3.7×10^3
$\sigma_{3D}(v)$ (kms^{-1})	0.27	0.40
Dynamical Time (yrs)	2.1×10^4	7.4×10^4
Density Profile (n)	1.37	1.08

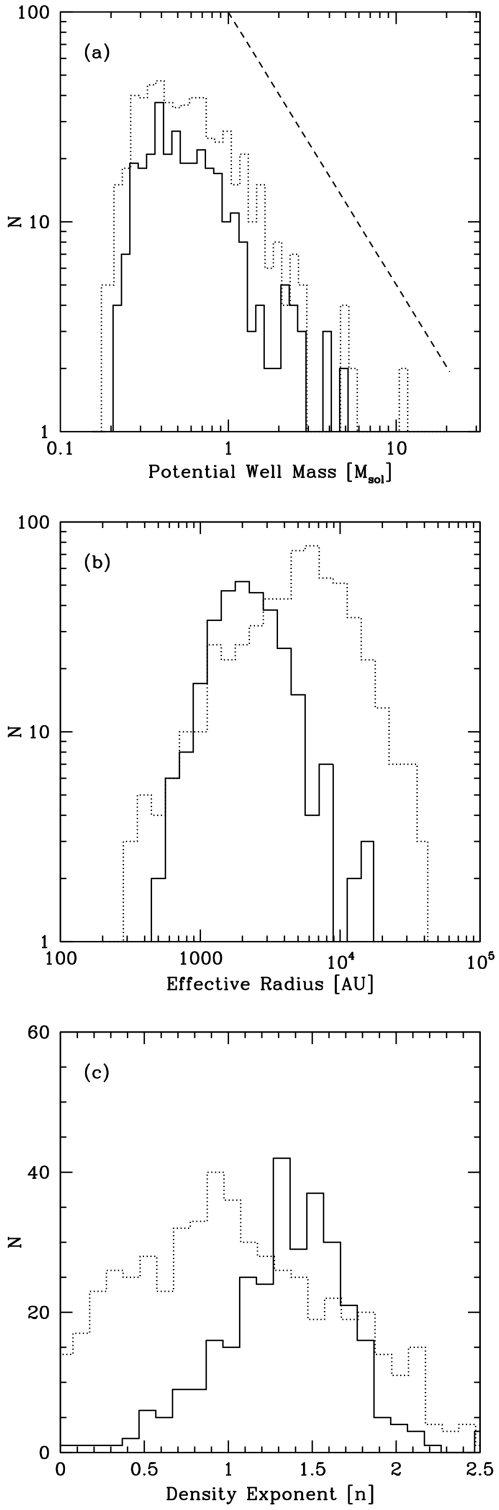

Figure 6.4: Histograms of the masses & sizes of the bound (*solid line*) and composite (*dotted line*) p-cores. Panel (a) shows the clump mass function. Masses above 0.2 $M_\odot$ are resolved and the Saltpeter slope is denoted by a dashed line. Panel (b) shows the effective radii. Panel (c) shows the best fit values of n for the profile $\rho \propto r^{-n}$. The p-core mass function resembles the stellar IMF and the p-cores are typically small, centrally concentrated objects.

6.4.2 Masses and Sizes

Figure 6.4 (a) shows the clump mass function (CMF) of the bound and composite p-cores, in which there is a clear resemblance to the IMF. The previous chapter showed that an IMF-like mass distribution was always obtained from MC structure using the traditional CLUMPFIND algorithm, but it was unclear whether this had any physical meaning. It has now been demonstrated that the bound cores also follow this distribution. This shows that at some level there is a link between molecular cloud structure, the formation of bound cores, and ultimately star formation. The link between p-cores and stars will be examined in Section 6.5

The average p-core masses for the bound and composite data-sets are very similar; 0.70 and 0.78 $M_{\odot}$ respectively. This is broadly consistent with the characteristic stellar mass (Chabrier, 2003). Both data-sets show this distribution, regardless the fact that members of the composite population are often unbound and do not form stars.

The distribution of the radii of the p-cores is shown in Figure 6.4. The bound p-cores have effective radii in the region of 2.4×10^3 AU, and the composite p-cores have radii of about 3.7×10^3 AU. Both distributions resemble a lognormal. Unlike the clump mass function, the distribution of the bound and composite data-sets differs in magnitude, which is due to the composite population containing a large number of unbound diffuse clumps.

6.4.3 Binding

The binding of the composite data-set is shown in Figure 6.5 (a), only 24% of the p-cores are bound ($E_{rat} > 1$). Moreover, for these p-cores, there is a tail which includes highly bound objects. The composite population consists of p-cores in a wide range of evolutionary states, a large fraction of which will not go on to form stars. Figure 6.5 (b) also shows the p-core masses plotted against energy ratio. There is no correlation between binding and mass in the simulation, contrary to some observations where the most massive cores are the most bound (e.g. Lada et al. 2008). This is due to the tendency of the larger cores to be more diffuse. Due to binding being roughly constant with p-core mass, bound cores appear to be selected with a uniform probability from the composite p-core distribution, which explains the resemblance between the composite and bound CMF's.

The density profile of the mass assigned to the core radially outwards, on the other hand, does show a correlation with binding. In Figure 6.5 (b), shallow ($n < 1$), intermediate

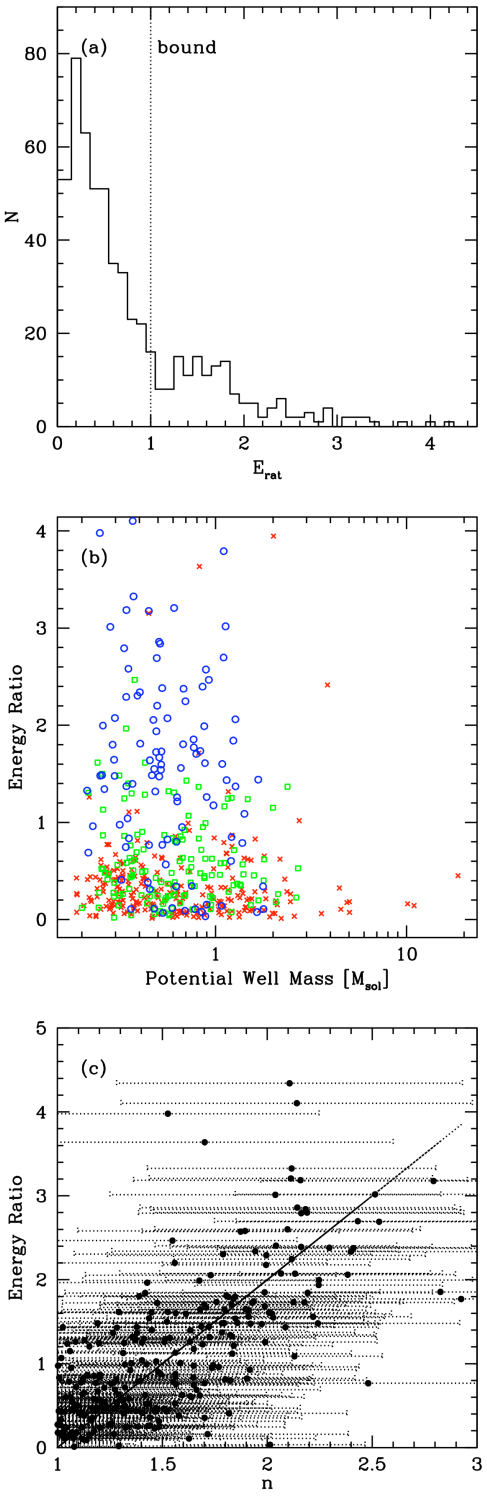

Figure 6.5: The binding of the composite p-cores. Panel (a) shows a histogram of the energy ratio of the cores, $E_{rat} \geq 1$ are bound, where $E_{rat} = |E_p|/E_{therm} + E_k$. Panel (b) shows the p-core masses plotted against energy ratio, blue circles denote cores with a steep $n > 1.5$ density profile, green squares intermediate $1 < n < 1.5$ profiles, and red crosses shallow profiles. Panel (c) shows the density exponent n plotted against energy ratio with error bars due to the poor fit from density substructure and non-spherical core shapes; the straight line has a gradient of two. There is no correlation between binding and mass, but there is a link to central concentration.

($1 < n < 1.5$) and steep ($n > 1.5$) density profiles are denoted by circles, squares and crosses respectively. It is found that the steepest profiles are nearly all bound, and about half of the intermediate profiles are bound. Figure 6.5 (c) shows the density exponents of the p-cores plotted against their energy ratio. When the profiles are shallow, a core is almost never bound, but when the potential well deepens and the core becomes more bound, the density profile steepens as the p-core becomes more centrally concentrated. However, there is a high degree of dispersion in this relation due to the difficulty of obtaining density fits from only quasi-spherical cores which contain substructure. Nonetheless, the steeper density profiles and increased central condensation show the clearest indication of binding from all the observationally visible quantities. This echoes the Bonnor-Ebert (Bonnor, 1956; Ebert, 1955) sphere model often used to model core observations (e.g. Johnstone et al., 2000), in which collapse begins above a critical ratio of maximum central density to mean density. However the p-cores are not generally in equilibrium, but are dynamically evolving in a similar manner to that shown in Ballesteros-Paredes et al. (2003).

Figure 6.6 shows the internal 1D velocity dispersions of the bound and composite p-cores. Originally 3D velocity dispersions were calculated but these have been converted to the 1D for easier comparison to observations. The mean 3D velocity dispersions were 0.27 and 0.4 kms^{-1} respectively, and when converted to a 1D velocity dispersion this becomes 0.16 and 0.23 kms^{-1}. The sound speed of an isothermal gas at 10K is 0.2 kms^{-1}, meaning the potential cores are at the transition between supersonic and subsonic velocities, and are therefore coherent objects (Goodman et al., 1998).

The mean dynamical timescale of a bound cores is calculated using the depth of the potential, rather than the standard practice of using the density, as the gravitational potential is the more clearly defined quantity for the p-cores. The potential and kinetic energies are equated using the virial theorem to obtain a typical velocity which is used to find the dynamical time as shown below, where R_{eff} is the effective radius of the core and ϕ the gravitational potential.

$$t_{dyn} = \frac{R_{eff}}{\sqrt{\phi}} \tag{6.2}$$

The average dynamical time is 2.8×10^4 yrs, and for the composite data-set it is about two times larger. This is more than ten times shorter than the dynamical time of the molecular cloud as a whole; meaning that several generations of cores can form and evolve throughout

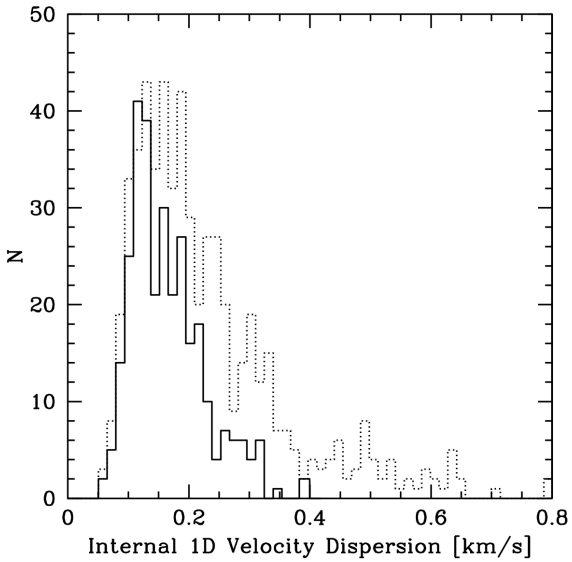

Figure 6.6: The one dimensional internal velocity dispersions of the p-cores in the bound(*solid line*) and composite (*dotted line*) datasets. The sound speed of an isothermal gas at 10K is 0.2 kms^{-1} which means the p-cores are generally subsonic

the lifetime of the simulated molecular cloud.

6.4.4 The Core Mass Function with Time

Figure 6.7 shows the mass functions of the pre-stellar (without sinks) p-core snapshots before they were merged into the composite data-set to integrate out time effects. Snapshots are shown at 0.6 to 1.2 simulation dynamical times ($t_{dyn} = 4.7 \times 10^5$ yrs) at intervals of 0.2 t_{dyn} . The high mass end of the clump mass function gets steeper with time, meaning that more massive cores were formed at the beginning of the simulation than at the end. This is probably due to cores at later times being more likely to form in the vicinity of an existing potential well. This will tidally truncate the size of the core, and hence limit the mass it can accrete. In the simulation the major regions of star formation are formed at the same time, and hence their evolution is artificially synchronous. If this were not the case the steepening of the mass function would not have been visible.

6.5 Clump Masses & Stellar Masses

Since the first observations of dense cores, a direct causal relation between them and stars was proposed (e.g. Motte et al., 1998). Alves et al. (2007) go further, and find that core masses and stellar masses are related with an efficiency of 0.3. However, this neglects the

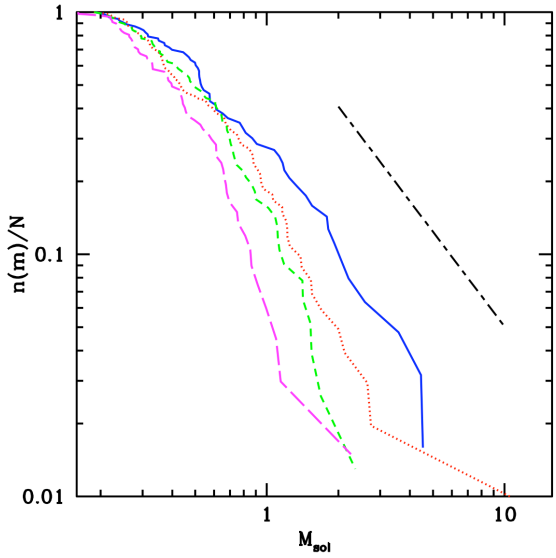

Figure 6.7: The cumulative mass functions from snapshots at *solid* 0.6 t_{dyn}, *dotted* 0.8 t_{dyn},*short dashed* 1 t_{dyn} and *long dashed* 1.2 t_{dyn}. The dot-dashed line shows the Salpeter slope. The mass function gets steeper with time as the high mass p-cores are formed earlier.

influence of environmental factors on the core during the accretion process. Moreover, Swift & Williams (2008) have shown that cores can have variable efficiencies or form multiple stars and still generate the expected IMF.

I now examine the correlation between core masses and their resulting stellar masses. To investigate how much of the p-core mass is available to form stars, the mass of the sink particles formed from them is traced with time. If a p-core forms more than one sink, their masses are added. This means what is actually being traced is the correspondence between p-cores and the stellar systems formed from them. Figure 6.8 shows the masses of the sink particles formed as a function of their p-core masses evaluated at a single snapshot in time. Sink masses are recorded at the end of the simulation and the p-cores in the snapshot population that did not form sinks are neglected.

There is no clear relation between the p-core masses and the sink masses. The sink masses all lie near or well above the p-core mass values showing the importance of subsequent accretion. Note that as feedback is not included and all sinks that form from a core are counted, it would be surprising if the efficiency of sink formation from cores was much less than 100%. Instead it is more than a factor of two higher. The actual stellar mass formed would of course be less than the sink mass, which simply represents the mass which would reach the inner disk of an accreting proto-star. During the accretion process mass will be ejected via a jet,

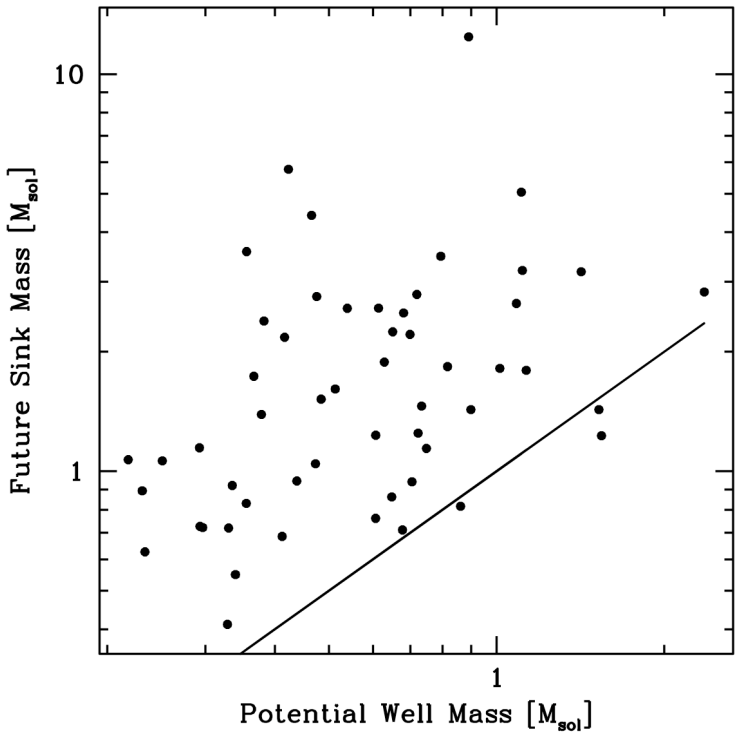

Figure 6.8: The connection between p-core masses at a snapshot in time and their sink mass when the simulation was stopped. The solid line shows a 1-1 correspondence. There is a poor correlation between p-core mass and the total sink mass formed from them.

a process which is not modelled here. However, if there is no correlation between the mass reaching the forming proto-star there is unlikely to be a correlation with the final star either. In fact the correlation is most likely to be further worsened by this process. For instance Matzner & McKee (2000) find a star formation efficiency of between $25\% - 70\%$ in model cores with feedback, depending on geometry. Interestingly, they also find that the stellar IMF formed from the cores is insensitive to core efficiency. Since all observations are necessarily at a snapshot in time this work suggests that the final stellar mass cannot be predicted accurately from the observed core mass even if the p-cores were directly observable.

One complication of Figure 6.8 is that the cores are all at different evolutionary states. This can be addressed by using their properties at the point in time where each is first bound, as this is when fragmentation and collapse begins, and when the best correlation to the p-core mass would be expected. The total mass in sinks formed from these p-cores is recorded at successive core dynamical times after they are first bound. In the simulation there is no mechanism to halt accretion, but as the p-core dynamical times (Equation 6.2) are short, the sink masses are found before this is an issue. Figure 6.9 shows the masses of the sinks after 1, 2, 3 & 5 dynamical times.

When comparing the sink mass at equal evolutionary stages of the bound p-cores, the correspondence is a lot tighter than that in Figure 6.8. At 1 dynamical time after the p-core is bound the sinks are below the 1-1 correspondence line. At 2 dynamical times they are around this level. These two stages, therefore, follow the accretion of the initial bound core, and so it would be surprising if this correlation did not exist! However, there is considerable scatter in this trend, with sink masses being as much as a factor of two away from the trend in either direction. This indicates that some cores are accreting their envelope at a faster rate in these initial stages.

As suspected, therefore, there must be a direct connection between bound cores and star formation. This improved correlation of p-core mass and sink mass is found at a specific point in time, when first bound. This leads us back to the original scheme of star formation proposed by Jeans (1902), as the potential bound cores represent the local Jeans mass at the point of collapse.

At 3 and 5 dynamical times the cores are accreting from their wider environment i.e. material which became bound to the cores subsequent to when $E_{rat} > 1$ for the first time. The

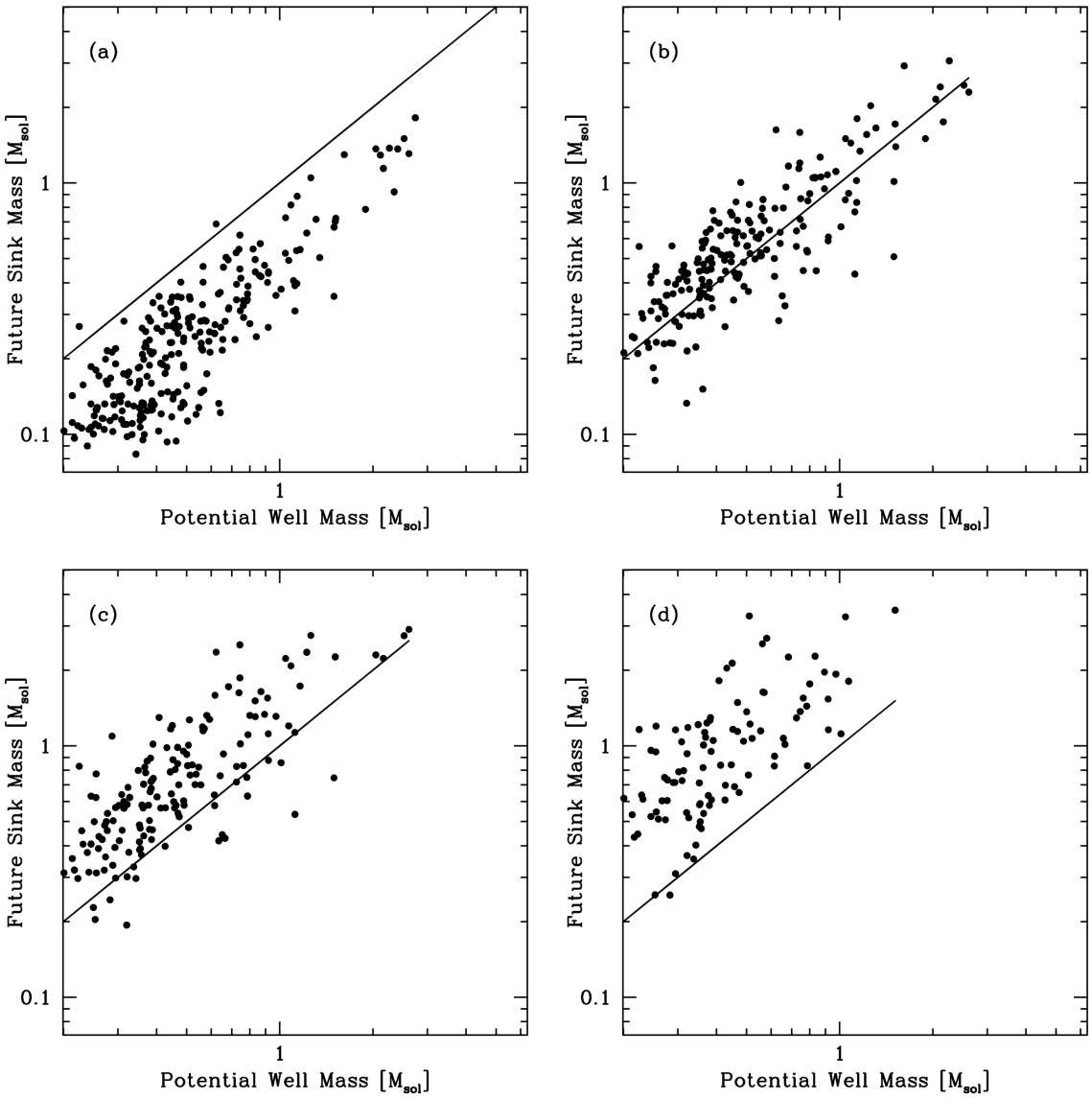

Figure 6.9: The connection between clump mass and sink mass at successive dynamical times. Panel (a) $t_{dyn} = 1$, (b) $t_{dyn} = 2$, (c) $t_{dyn} = 3$, (d) $t_{dyn} = 5$. The solid line shows a 1-1 correspondence. There is now a clear connection between p-core mass and sink mass, but it still shows significant dispersion.

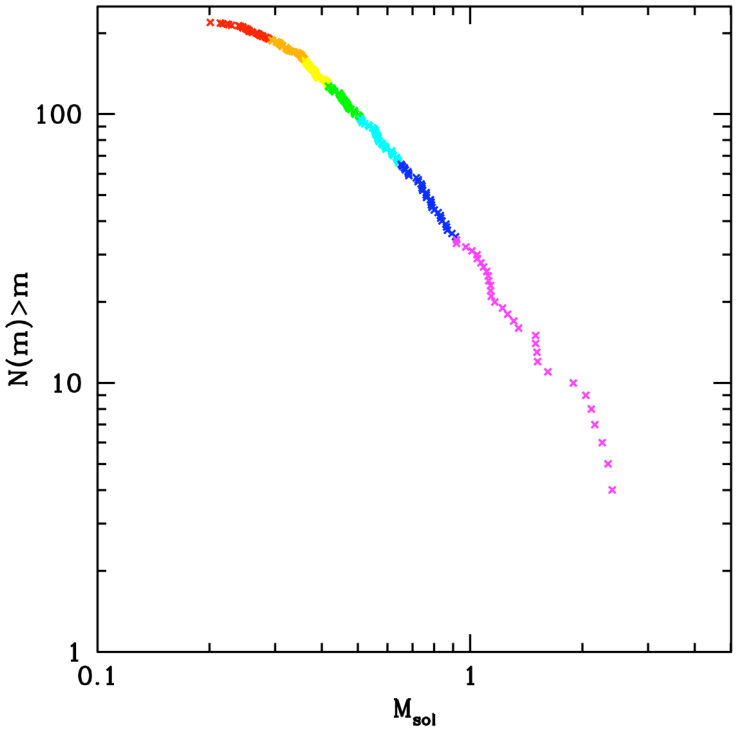

Figure 6.10: The CMF of the p-cores with mass bins denoted by different colours.

correlation between core masses and sink masses becomes increasingly dispersed in log-space as accretion wipes out the direct correspondence and increases the offset as the sink-masses grow with time. Cores surrounded by a plentiful reservoir of gas on all sides will be more successful at these stages than those in a narrow filament for example.

Despite the poor correlation between core mass and sink mass, a Salpeter like mass function is always maintained. This is illustrated graphically in Figure 6.10 which shows the cumulative clump mass function of the bound cores. Each point on the graph represents a p-core mass when first bound (the best case scenario) and different mass ranges are denoted with different colours. I now trace the evolution of these cores into sinks, keeping the colours of the sink the same as its parent core. If there was a perfect $1-1$ correlation, then the colour bands would remain distinct. Figure 6.11 shows the resulting mass functions at subsequent dynamical times. The colours are now well mixed, showing that the p-cores are evolving with variable efficiencies. Nonetheless, the shape of the IMF is maintained throughout, due the the effects of competitive accretion. Therefore, it could be said that for a population of cores there is a high probability that a more massive core will form a more massive star, but for a specific object no reliable predictions of final mass can be made.

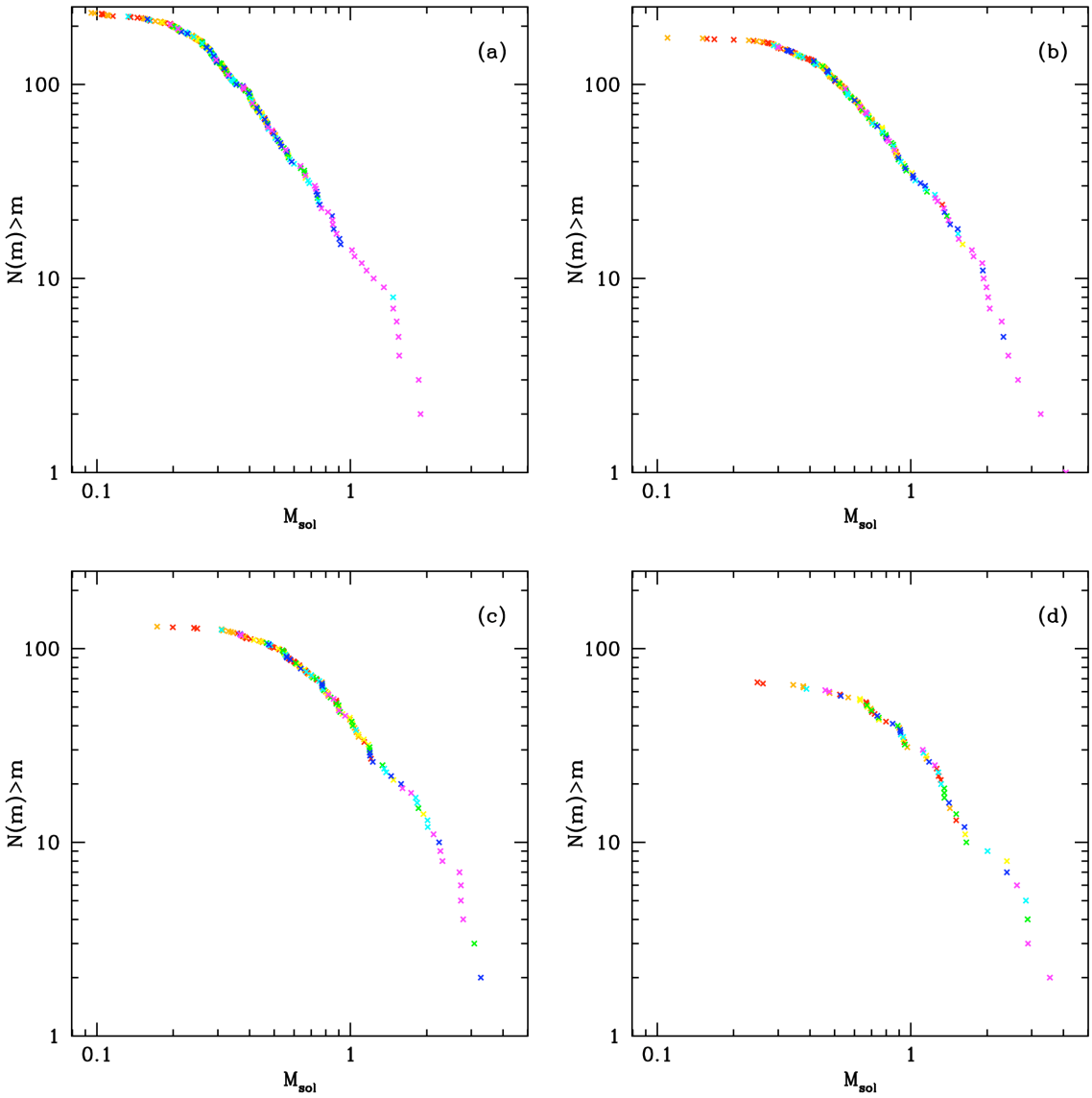

Figure 6.11: The initial mass functions of the sinks formed from bound cores the colours are the same as their parent p-cores shown in Figure 6.10. The IMF's are recorded at intervals of $1, 2, 3$ & 5 p-core dynamical times. The mass bins get mixed up with time, but the shape of the mass function always resembles the stellar mass function despite the inexact correspondence between core mass and sink mass.

In summary, the bound p-cores all form stars, but some are more successful at accreting additional mass than others. This is most likely due to environmental factors, for example, core geometry, surrounding gas reservoir, dynamical interactions or competition from neighbouring proto-stars. This suggests, that in order to understand star-formation, not only the cores of gas must be studied, but also the wider environment in which they form. The correspondence between cores and stars is even more difficult to determine at a snapshot in time when cores are at a variety of evolutionary stages.

6.6 Discussion

It has been theorised that the power law clump mass function is formed as a product of supersonic turbulence (Henriksen, 1986; Larson, 1992; Elmegreen, 1997; Klessen, 2001; Padoan & Nordlund, 2002; Hennebelle & Chabrier, 2008). The core mass function has been observed by many authors (e.g. Motte et al. 1998; Testi & Sargent 1998; Johnstone et al. 2000; Nutter & Ward-Thompson 2007; Ikeda et al. 2007) and bears a remarkable resemblance to the stellar IMF. It is now confirmed that this profile is also observed in the first bound fragments that have been identified in this simulation.

However, the p-cores are not directly comparable to observed cores as they are identified in three dimensions, and use gravitational potential instead of density. Further, it has also been shown that the core properties obtained from applying CLUMPFIND to 2D observations are unreliable (Kainulainen et al., 2009; Smith et al., 2008). The p-cores are more well defined as they are found from a smooth distribution where all structures are significant. Comparisons between observed core properties and p-core properties must therefore be made cautiously. Nonetheless it is useful to contrast the typical sizes of observed cores to identify which objects are on the most similar size scales to the first bound fragments. Table 6.3 summarises observed properties of density cores in different regions and species from a variety of authors.

P-cores are typically smaller than most density cores identified observationally, having average masses of 0.7 $M_\odot$ and radii of 2.4×10^3 AU when first bound. Their internal 1D velocity dispersions are typically just subsonic. The p-cores are most similar to high resolution observations of cores in nearby molecular clouds (e.g. Simpson et al. 2008; Enoch et al. 2008). It is expected that the difference between most observed cores and the potential cores is mainly due scale differences (Table 6.3. Most surveys, particularly of more distant regions

Table 6.3: A comparison to a small selection of core measurements from the literature. Authors are shown, additional velocities are from * Lada et al. (2008), **Rosolowsky et al. (2008) and show the 1D internal velocity dispersion. Simpson et al. (2008) is a re-analyses of mm observations in Ophiuchus from various published works. Note the p-cores found in this work are defined differently, as they use 3D potential rather than 2D column density.

Author	Region	Species	Typical Clump Size [AU]	Clump Mass Range $M_\odot$	Mean Velocity Dispersion kms^1
Ikeda et al. (2007)	OrionA	H13CO+	2.9×10^4	$2.1 - 81$	0.52
Johnstone et al. (2006)	Orion B	mm cont	1.4×10^4	$0.4 - 30$	-
Alves et al. (2007)	Ophiuchus	extinction	$\sim 5 \times 10^4$	$0.5 - 28$	< 0.2*
Simpson et al. (2008)	Ophiuchus	mm 850μ	$\sim 3 \times 10^3$	$0.1 - 10$	-
Enoch et al. (2008)	Oph/Per/Serp	1.1mm cont	$\sim 7 \times 10^3$	$0.2 - 4.8$	0.24**
This work	simulated	potential (bound)	2.4×10^3	$0.2 - 5$	0.16
This work	simulated	potential (composite)	3.7×10^3	$0.2 - 10$	0.23

such as Orion, would not be able to resolve cores of the size found here, and as previously shown coarse resolution observations still produce a Salpeter like mass function, but with systematically higher masses.

Although the clump mass function observed from density fluctuations is shown to resemble the stellar initial mass function, there was no requirement for this to be true for the distribution of masses at which cores first become bound. In fact, in the competitive accretion theory of star formation the seeds of gravitational collapse can follow any distribution and the IMF will still be generated through subsequent accretion (Zinnecker, 1982). That the time integrated bound fragments also follow this distribution further supports the idea that they are sampled from a hierarchical density distribution generated by turbulence.

However, at a snapshot in time the majority (76%) of the p-cores are unbound and may be transitory. This has implications for observational surveys which are necessarily at a snapshot in time, as the vast majority of objects have either not reached the point of collapse or will not form stars at all. The case for a 1-1 correlation between core mass and stellar mass can not hold in these cases. There is also the further complication that the p-cores contain substructure that could be further identified as individual objects if one were performing a density decomposition (depending on the resolution of the data). Naturally, these yet smaller objects are even less bound than their parent p-core. The high value of unbound pre-stellar p-cores in this analysis is surprising because as they are identified using gravitational potential this force must be significant. There is observational evidence for unbound cores. Lada et al. (2008) find that the majority of cores found from dust extinction in the Pipe nebula are unbound, and André et al. (2007) find 25% of their cores in Ophiuchus to be unbound.

The p-cores showed significant density sub-structure, despite being identified from a smooth potential well. If a traditional clump finding algorithm using emission or density had been used to identify them, they would have been split into smaller objects. The p-cores were also only quasi-spherical, and their central peak in potential did not necessarily correspond with their center of mass, as they were not relaxed. This suggests that using smooth symmetrical models to study core collapse (such as Bonnor-Ebert spheres) can at best only be a first approximation.

Unfortunately, the simulation does not include magnetic fields, which can act against collapse on some length scales (Hennebelle & Passot, 2006). Price & Bate (2008) found that

magnetic fields introduce voids into molecular cloud structure and reduce subsequent accretion. Additionally, this simulation does not include radiative transfer. However, as cores are being considered early in their evolution before a protostar is formed, and accretion luminosity only affects scales of less than 1000 AU (Krumholz et al., 2007; Bate, 2009), this should not be a significant issue.

Due to the similarities between the stellar IMF and the clump mass function it has been proposed that the mass of stellar systems is directly related to the clump they formed from (e.g. Motte et al. 1998; Alves et al. 2007). However, when I traced the total mass in sink particles formed from the p-cores at a snapshot in time, as would be visible observationally, the correspondence was effectively non-existent. A stronger correlation between core masses and total sink mass was found when the p-core masses were recorded at the time when they were first bound. Further accretion increases the dispersion in this relation and introduces an offset.

Throughout the simulation the most massive bound core had a mass of only 6.35 $M_{\odot}$, whereas the most massive sink at the end of the simulation had a mass of 27.97 $M_{\odot}$. There was no p-core which could form a massive star simply from its own material when first bound. All the bound cores were at best only marginally supersonic and hence were not supported by turbulence, contrary to the massive turbulent cores predicted by McKee & Tan (2003). Note, however, that the lack of feedback and magnetic fields in these simulations may limit the ability to sustain turbulence in cores.

In most cases gas from outside the region initially bound was accreted by the sinks formed from the p-core after only 6×10^4 yrs. This subsequent accretion means that the environment surrounding the p-core is also important for its future evolution, for example whether it is surrounded by a large gas reservoir or is in a narrow filament.

There is a higher probability that a more massive p-core will form a larger total sink mass, but for an individual p-core no accurate prediction can be made. The link between core mass and sink mass is poor because there are a number of additional environmental factors beyond the bound mass which will affect the evolution of the core, for example the shape of the core and the distribution of gas it is embedded within. Despite the poor correspondence between p-core masses and sinks, the shape of the mass function obtained from the p-cores as they evolve into sinks always resembles the stellar IMF.

6.7 Conclusions

The earliest fragmentation in a simulated molecular cloud has been identified using the distribution of gravitational potential rather than density. This is a smoother distribution, due to gravity being a long range force, and it allows us to assign boundaries with clearer physical meanings. The fragment's evolution is traced with times. If they became bound, their masses were identified when ($E_p > E_k + E_{therm}$) for the first time, and this is related to the mass in sink particles formed from them. This allows the scale of the initial fragmentation to be identified and traced as it evolves into a stellar IMF. The main conclusions are as follows:

1. The time-integrated mass function of just-bound gravitational potential 'p-cores' resembles the stellar initial mass function in a similar manner to that of gas density cores
2. The bound p-cores are most similar to the very smallest density cores currently observable (an average of 0.7 $M_\odot$ with a radius of 2300 AU).
3. P-cores exhibit significant density substructure.
4. There is a poor correlation between p-core mass and the total mass in sinks formed from them. This is particularly true when the p-cores are recorded at a snap-shot in time, but still holds when the mass is recorded when they are first bound.
5. The sink particles formed from the p-cores accrete from beyond the region initially bound. This means that the surrounding environment of the core also has an effect on the star formation in the simulation.
6. Despite the poor correlation between p-core mass and sink masses the sink IMF always resembles the stellar IMF.

7

The Simultaneous Formation of Massive Stars and Stellar Clusters

In the previous chapter it was found that the final mass of sink particles depended at least in part on their environment. Of particular interest is the evolution of massive stars, as no evidence of massive pre-stellar cores was found in the simulations used in Chapter 6. It has already been noted by Bonnell et al. (2004) that massive stars are formed within clusters and that the number of stars formed in the cluster correlates well with the growth of the massive stars. In this chapter the formation of massive stars within a forming stellar cluster is examined in more detail.

7.1 The Formation of Massive Stars

Massive stars are almost universally formed in star clusters (Lada & Lada, 2003) and so the physical processes involved in forming clusters must be intrinsically linked to high mass star formation. Recent observations of infra-red dark clouds (IRDC's) (Egan et al., 1998; Carey

Table 7.1: Typical properties of clouds, clumps and cores (adapted from Bergin & Tafalla 2007.)

	Cloud	Clump	Core
Size (pc)	$2-15$	$0.3-3$	$0.03-0.2$
Mass ($M_\odot$)	10^3-10^4	$50-500$	$0.5-5$
Mean density (cm^{-3})	$50-500$	10^3-10^4	10^4-10^5
Velocity Extent (kms^{-1})	$2-5$	$0.3-3$	$0.1-0.3$
Gas Temperature (K)	~ 10	$10-20$	$8-12$

et al., 1998, 2000; Simon et al., 2006; Rathborne et al., 2006) and high-mass proto-stellar objects (HMPO's) (Beuther et al., 2002; Sridharan et al., 2002; Williams et al., 2004; Faúndez et al., 2004) have begun to probe the earliest stages of the massive clumps from which star clusters are formed.

So how does high mass star formation proceed within the complicated environment of of a forming cluster? Is the mass that forms the massive star gathered before, during or after the cluster formation? This is particularly relevant as regards the evolution and interactions of the pre-stellar gas cores thought to be the precursors of star formation.

A reminder of the properties of clumps and cores, as defined in Chapter 1, is shown in Table 7.1. Effectively the terms are used to simply denote different scales of structure. Clumps are regions of enhanced density within a molecular cloud, which will typically form stellar clusters. Cores are density condensations smaller than a clump which have a gravitational potential distinct from their environment and do not contain any smaller scale structure which is already bound.

Motte et al. (2007) carried out an unbiased survey of Cygnus X to identify the earliest high mass star forming complexes. They found evidence of star formation in all their embedded cores, and were unable to find a massive pre-stellar clump, leading to the conclusion that these objects were either extremely short lived ($< 10^3$ years), or did not exist. Similarly, observations of massive cores (e.g. Rathborne et al., 2005; Pillai et al., 2006; André et al., 2008) have always found signatures that star formation was already underway. Marseille et al. (2008) find a possible pre-stellar massive core, but any mid-IR emission from it is confused by a nearby source. In conclusion, true pre-stellar massive cores remain elusive.

Due to the lack of pre-stellar massive cores, Motte et al. (2007) proposed that the precursors of Class 0 massive proto-stars must be the larger starless clumps which would form them by collapsing supersonically. Dynamic collapse of HMPO's to form stars was also proposed by Beuther et al. (2002) to explain their observed line-widths. Further, Peretto et al. (2006,

2007) found that the massive cluster forming clump NGC 264-C was collapsing along its axis on its dynamical timescale, and therefore channelling mass towards the Class 0 object at its centre.

This dynamical collapse of clumps during the star-formation process is in agreement with the proposal of Elmegreen (2000) that star formation basically takes place in a crossing time and that cloud lifetimes are short. Tan et al. (2006) present a contrasting view where clusters form quasistatically, although this is partially based on a large estimate for the age of the Orion nebula cluster. Hillenbrand (1997), however, found that the mean stellar age within the Orion nebula was below 1 Myr albeit with a few older outliers in the range $1 - 10$ Myr. Hartmann (2003) argue that these outliers are accounted for by a combination of uncertainties in the stellar birth line where stars appear on the H-R diagram and foreground contamination.

Additionally, observations of a velocity gradient within the Orion nebula by Fűrész et al. (2008) and Tobin et al. (2009) suggest that the cluster may currently be in a state of sub-virial collapse, and due to the kinematic correlation between stellar and gaseous components must be young. The focussing power of gravity to produce structures has been further highlighted by Hartmann & Burkert (2007), who suggest that the Orion Nebula Cluster itself could have been produced from the large scale collapse of the Orion A cloud.

There are two main theories of massive star formation; the first of which is basically a scaled up version of low mass star formation, where massive stars form from well defined massive cores supported by turbulence (McKee & Tan, 2003). The difficulty with this model is that it presupposes the existence of massive prestellar cores that have somehow evaded fragmentation during their formation stages (Dobbs et al., 2005). Krumholz (2006) suggest that radiative feedback can limit the fragmentations but as this chapter shall show, radiative feedback does not result in the formation of massive prestellar cores.

Alternatively, in the competitive accretion scenario (Zinnecker, 1982; Bonnell et al., 2001, 2004) cores are the 'seeds' of star formation, the most massive of which have a larger gravitational radius, and are thus more successful at accreting additional mass, and so grow into massive stars. There are a few common misapprehensions about this theory. Firstly, the protostars which become massive do not generally have high velocities with respect to the cloud they inhabit. They tend to stay at the centre of gravitational potential of the forming star cluster which they help define. Secondly, they accrete material via two mechanisms. There is

a contribution from Bondi-Hoyle accretion, but when the velocity relative to the system is low the accretion is mainly regulated by the tidal field. Thirdly, there is no requirement for stellar mergers (Bonnell et al., 1998).

At later evolutionary stages, Keto (2007) has shown that accretion can continue to form massive stars, even when they have begun to ionise their surroundings. In this model a hypercompact HII region is formed around the massive stars as they grow by accretion. As the star grows in mass, outflows form and their opening angle increases, however even when the star is extremely massive, accretion still proceeds around an equatorial disk.

This chapter describes how massive stars are formed within a dynamic clump which is forming a stellar cluster, with particular attention to the cores within it. In Section 7.2 the numerical simulation is outlined and a simple approximation for radiative heating is described. Section 7.3.1 illustrates how dynamic collapse causes a star forming clump to evolve from a diffuse filamentary structure to a more massive concentrated structure which is brighter in dust continuum emission. Simulated interferometry images are generated from the data and compared to observations. The results are discussed in the context of global collapse and accretion in Section 7.4, where it is shown that the clump potential channels mass onto its centre, where the proto-stars with the greatest gravitational radius accrete it. This means that the global evolution of the forming star cluster as a whole has a direct link to the massive stars it forms. It is shown that low mass cores close to the central massive star are unaffected by this process. Finally in Section 7.5 the conclusions are presented.

7.2 The Simulation

The smoothed particle hydrodynamics (SPH) method is used to follow the evolution of a 10^4 $M_\odot$ cloud over 1.02 free-fall times or $\approx 6.6 \times 10^5$ years. The initial conditions are the same as those used in Chapter 6 but have been re-simulated at increased resolution by Bonnell et al. (2008). The cloud is cylindrical in form, with a length of 10 pc and a radius of 3 pc. The cloud contains a local density gradient causing the ends of the cylinder to have initial gas densities that are 33% higher/lower than the average density. The gas has internal turbulence following a Larson-type $P(k) \sim k^{-4}$ power law and is normalised so that the total kinetic energy balances the total gravitational energy in the cloud. The density gradient then results in one end of the cloud being more than bound (still super virial) while the other end of the

cloud is unbound.

The cloud is made up of 15.5 million SPH particles on two levels to maximise the numerical resolution in regions of interest. The regions of interest are determined from the low resolution run used in Chapter 6 which consisted of 5 million SPH particles with mass resolution of 0.15 $M_\odot$. Regions requiring high resolution were identified from the SPH particles that underwent star formation and formed sink particles (see below) or were subsequently accreted by these sink particles. These particles were replaced in the initial conditions with 9 lower-mass particles, conserving the mass and kinetic energy of the initial conditions, but now with a mass resolution of $0.0167M_\odot$. The simulation was re-run from the initial conditions with this higher resolution.

The simulation treats the thermal content of the cloud through the barotropic equation of state introduced in Chapter 2. However in addition to this equation of state, radiative feedback is approximated from the newly formed stars by way of a grid of previously computed Monte Carlo radiative transfer models of young stars (Robitaille et al., 2006). A one-dimensional temperature profile was derived from the youngest of these models as a function of stellar mass and distance from the star by Ian Bonnell. This gives a very rough estimate of the radiative feedback which, if anything, should overestimate the gas temperatures. Nevertheless, it gives an estimate of the emission expected in regions of massive star formation. From these models the temperature due to the radiative feedback is set as

$$\begin{aligned} T(r) &= 100. \left(\frac{m}{10_\odot}\right)^{0.35} \left(\frac{r}{1000AU}\right)^{-0.45} K; \qquad m < 10M_\odot, \\ T(r) &= 100. \left(\frac{m}{10_\odot}\right)^{1.11} \left(\frac{r}{1000AU}\right)^{-0.5} K; \qquad m > 10M_\odot \end{aligned} \tag{7.1}$$

The gas temperature around the young stars is set to be the maximum of the temperature from either the the dust/line cooling equation of state or the radiative feedback. This ensures a maximal effect from the radiation.

7.3 Massive Clump Evolution

7.3.1 Time Evolution

Three regions of star formation are considered, each of which resembles a single clump at some point when viewed at a low resolution. The global properties of these regions are calculated by simply including all the material within a radius of 1 pc from the largest sink.

Table 7.2: The massive clump properties recorded at the beginning (3.53×10^5 yrs) and end (5.9×10^5 yrs) of the analysed period. The first mass M is that found within a 1 pc radius of the central sink. The second is that within a cylindrical column of radius 1pc centered on the same sink. The mean gas density is denoted by $\bar{\rho_g}$, and max. M_s and tot. M_s represent the maximum sink mass within the clump and the total sink mass respectively.

Clump	M [$M_\odot$]	M_{2D} [$M_\odot$]	$\bar{\rho_g}$ [gcm^{-3}]	max. M_s [$M_\odot$]	tot. M_s [$M_\odot$]
beginning					
Alpha	893	1528	1.1×10^{-18}	0.85	3.10
Beta	882	1516	4.0×10^{-19}	1.11	2.24
Gamma	1034	1985	7.6×10^{-19}	0.58	1.84
end					
Alpha	987	1412	8.0×10^{-18}	29.2	361.4
Beta	995	1882	8.8×10^{-18}	11.3	189.2
Gamma	1127	1993	5.0×10^{-18}	12.6	243.9

Table 7.3: The binding energy of the three clumps at the beginning (3.53×10^5 yrs) and end (5.9×10^5 yrs) of the analysed period. The average radial velocity of the sph gas particles is given by $\bar{v_r}$, where negative values show inward motion. The binding of the clumps is given by E_{rat}=E_p/E_{kin}+E_{therm}, and the absolute magnitude of the potential energy is shown by E_p. For E_{rat2}, the kinetic energy was calculated without including any inward velocities.

Clump	$\bar{v_r}$ [kms^{-1}]	E_{rat}	E_{rat2}	E_p [erg]
beginning				
Alpha	-0.45	3.4	18.8	1.26×10^{-47}
Beta	-0.62	0.8	4.6	8.64×10^{-46}
Gamma	-0.44	1.8	11.1	1.08×10^{-47}
end				
Alpha	-1.62	1.09	3.0	4.78×10^{-47}
Beta	-1.16	0.57	3.0	2.49×10^{-47}
Gamma	-0.19	1.61	4.5	2.64×10^{-47}

Although this is a simplistic definition, it is preferred to a clump-finding approach for several reasons. Firstly, the boundaries found from clump-finding are extremely subjective (Smith et al., 2008; Kainulainen et al., 2009) and secondly, defining an absolute spatial scale allows an unambiguous comparison of the physical properties of the studied regions. These 'clumps' are labeled, Alpha, Beta and Gamma and Table 7.2 shows their properties.

The mass in the clumps is high in all cases. This is partly due to the decision to use a large clump radius, so that the analysis is not complicated by additional mass entering the region at later times, but also due to the requirement that to form a large cluster you need a lot of mass. A 2D projected measurement increases the clump masses by $50-100\%$ compared to the 3D case due to contamination from along the line of sight. This highlights the problems of determining masses from only 2D information. In every case the mean gas density in the clumps increases with time due to collapse. The most massive sink is formed in clump Alpha despite the fact that it is not the most massive clump. However this clump does contain the largest total mass in sinks and has the deepest potential well.

Table 7.3 outlines the in-fall velocities and binding energies of the clumps at the beginning and end of the simulation. All of the studied regions exhibit significant supersonic in-fall motions, with the exception of clump Gamma at the end of the simulation, which is roughly sonic, ($c \approx 0.2$ kms^{-1}). This is in agreement with the observation of Motte et al. (2007) that rapid supersonic inward motions are required to enhance clump densities to the values seen in massive proto-stellar cores. Typical in-fall here is a few times the sound speed, which equates to lifetimes of the order of a million years.

The relative binding of the clumps provides an explanation for the location of the most massive sinks. At the beginning of the analysis; clump Alpha is bound (it has 3.4 times more gravitational potential energy that kinetic and thermal energy), clump Beta appears unbound, and clump Gamma is bound (it 1.8 times more potential energy than kinetic and thermal energy). The binding decreases at the end of the studied period due to the large increase in kinetic energy from randomised gas motions during the collapse process, and heating from the sinks. It is surprising that clump Beta appears unbound, yet is collapsing. This was due to the absolute magnitude of the gas velocities being used to calculate the kinetic energy, despite the fact that in-fall velocities are not supportive. To address this a second energy ratio, E_{rat2}, was calculated where the inward velocities were excluded (Vazques-Semadeni,

private communication). Using this measure of binding all of the clumps are significantly bound, particularly clump Alpha (which contains the largest sink) which is now 18.8 times over-bound at the beginning of the studied period.

When the magnitude of the potential energy of the clumps is considered directly it is seen that once again Clump Alpha has the greatest potential, followed by Gamma and then Beta. This is the same order as the clumps which contain the most massive sinks, and for the clumps with the greatest total mass in sinks. This suggests that the star formation process is most efficient where the potential energy of the clump as a whole is highest, and this is reflected both in the efficiency of forming a stellar cluster and in the efficiency of forming a massive star. This provides a natural explanation for the link between total stellar mass and the most massive star outlined in Bonnell et al. (2004).

In Figures 7.1, 7.2, & 7.3, the column density of gas within the clumps is shown at three snapshots in their evolution. For clarity, sink particles denoting sites of star formation are not shown. The central region of clump Alpha is shown in Figure 7.1 at 0.75, 1, and 1.25 dynamical times ($t_{dyn} = 4.7 \times 10^5$ yrs). It has a filamentary geometry and the self gravity of the ends of the filament is strong enough for them to collapse independently. However, both objects have inward velocities and are collapsing towards the centre. Notice how the later structure is less filamentary and contains less substructure. Each of the large condensations along the filament is forming at least one substantial star and could perhaps be thought of as a proto-stellar massive star forming core, however as shall be discuss later, there are also smaller cores within them, forming lower mass stars.

Figures 7.2 and 7.3, show the central region of clumps Beta and Gamma. These clumps have been formed by several shock fronts intersecting to form a region of high density. Again, over time the extended structure collapses to form a more compact object. The density peaks, where the stars are forming, are carried along with this collapse. In effect the clump is formed at the same time as the stars are formed. As before, the clump evolves from a diffuse filamentary distribution to a more centrally condensed distribution.

To describe more quantitatively the evolution of the clumps as a whole, two quantities are calculated from the full 3D data at each simulated time-step. Firstly, the absolute mass contained within a parsec radius of the most massive sink particle is recorded. Secondly, the

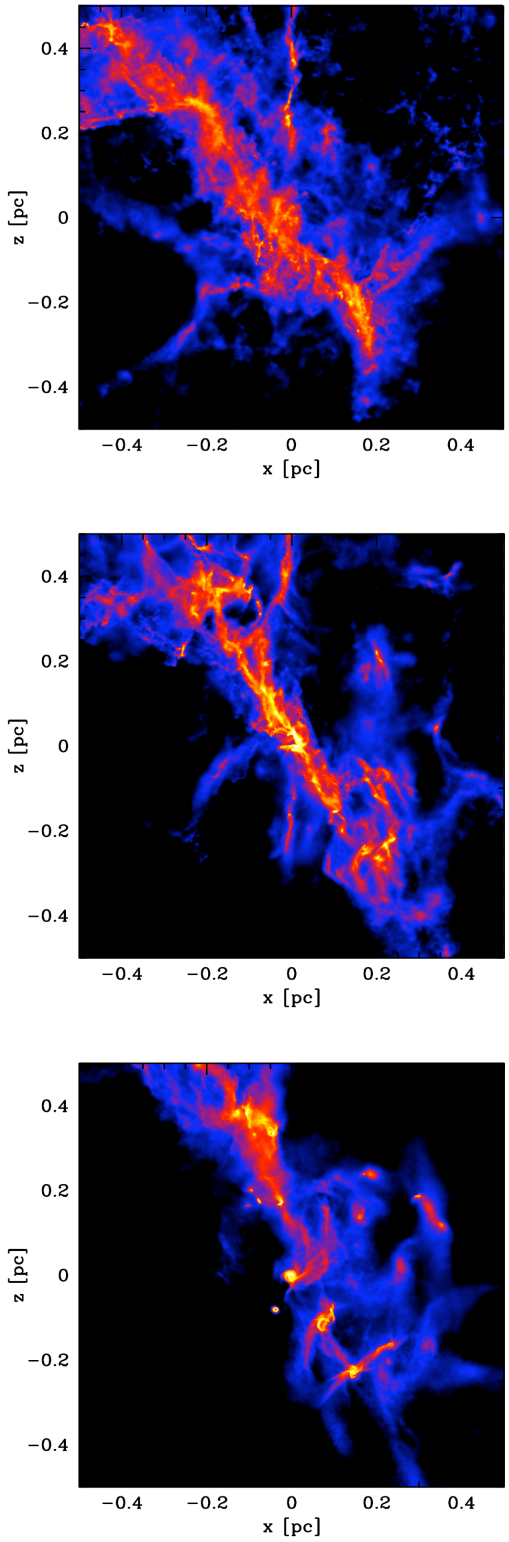

Figure 7.1: The evolution of the centre of clump Alpha *top*. The snapshots shown are at *left* 0.75 t_{dyn} (3.53×10^5 yrs), *middle* 1 t_{dyn} ($\sim 4.7 \times 10^5$ yrs) and *right* 1.25 t_{dyn} (5.9×10^5 yrs) respectively. The colour scale denotes column densities from 0.05 $g\,cm^{-2}$ to 5 $g\,cm^{-2}$. The structure becomes more compact with time, and decreases in substructure.

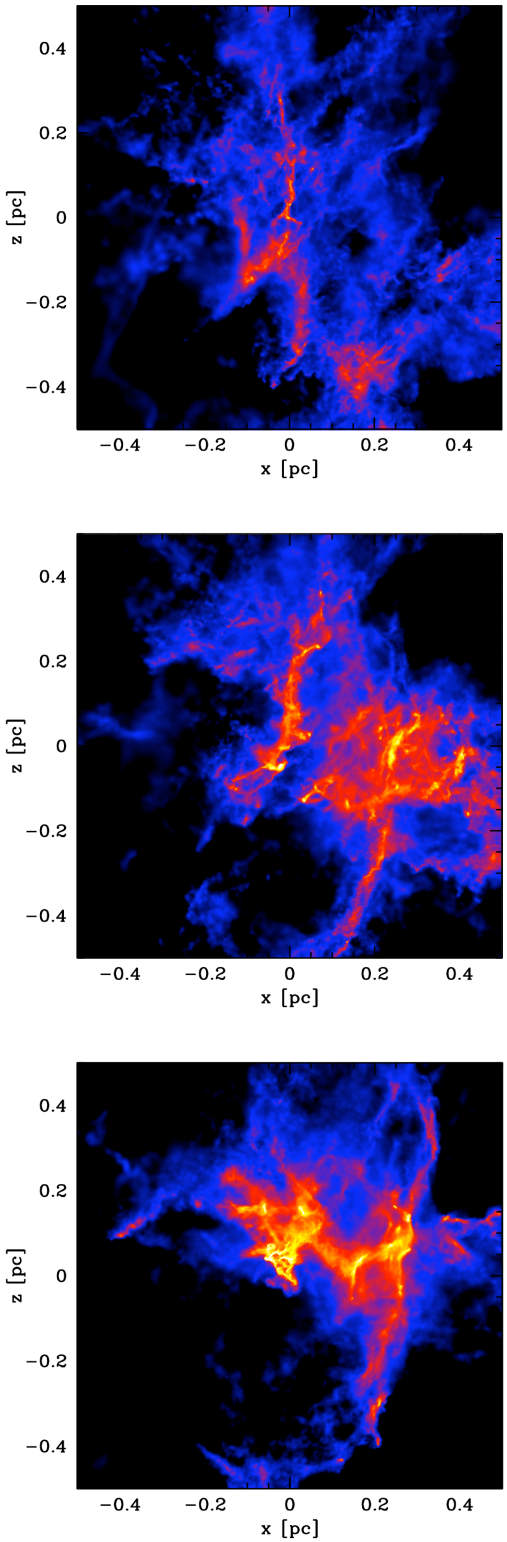

Figure 7.2: The evolution of the centre of clump Beta *middle*. The snapshots shown are at *left* 0.75 t_{dyn} (3.53×10^5 yrs), *middle* 1 t_{dyn} ($\sim 4.7 \times 10^5$ yrs) and *right* 1.25 t_{dyn} (5.9×10^5 yrs) respectively. The colour scale denotes column densities from 0.05 g cm^{-2} to 5 g cm^{-2}. The structure becomes more compact with time.

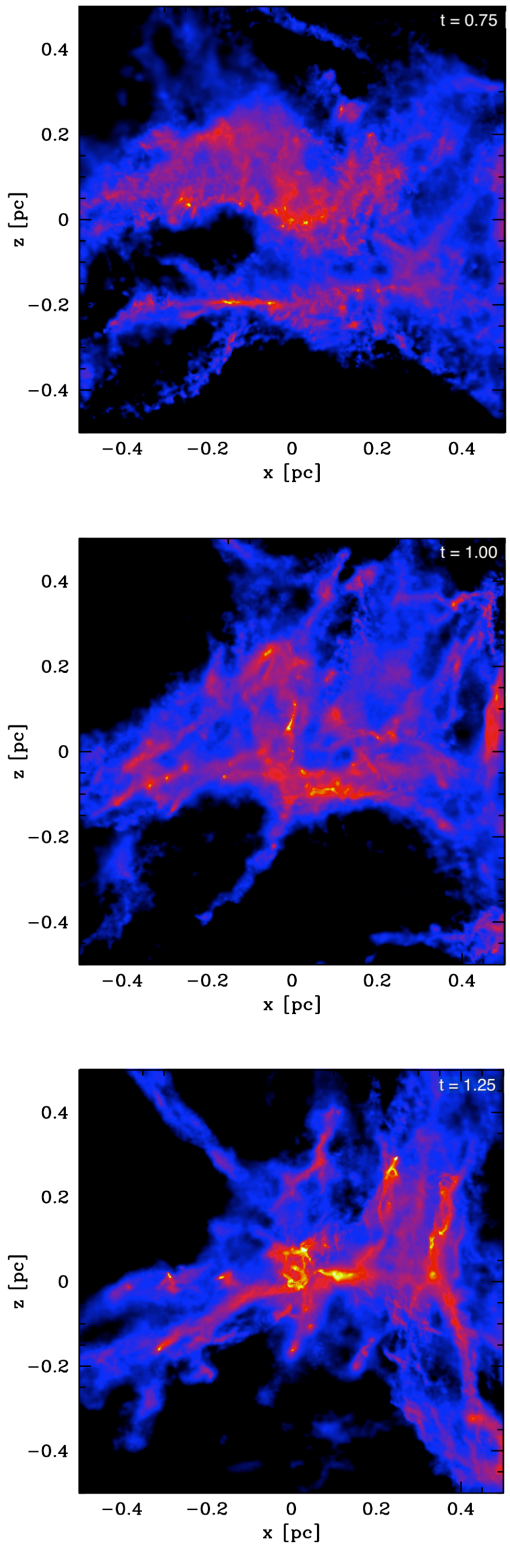

Figure 7.3: The evolution of the centre of clump Gamma *bottom*. The snapshots shown are at *left* 0.75 t_{dyn} (3.53×10^5 yrs), *middle* 1 t_{dyn} ($\sim 4.7 \times 10^5$ yrs) and *right* 1.25 t_{dyn} (5.9×10^5 yrs) respectively. The colour scale denotes column densities from 0.05 $g\,cm^{-2}$ to 5 $g\,cm^{-2}$. The structure becomes more compact with time.

dispersion of the surrounding mass is calculated using,

$$\sigma(r)_{3D} = \sqrt{\frac{\sum m_i (r_i - \bar{r})^2}{\sum m_i}} \tag{7.2}$$

where m_i is the mass of the i'th SPH particle, and $r_i - \bar{r}$ is its distance from the central sink. Both gas masses and sink masses are included in this calculation. Figure 7.4 shows the results. The mass in the locality of the massive sinks generally increases with time. The exception to this was clump Beta where not all of the mass entering the region was bound and some escaped again. Moreover, the continuously decreasing dispersions show that the clump is collapsing and therefore continually channeling mass inwards.

Krumholz & McKee (2008) found that a minimum gas column density of 1 gcm^{-2} was required for there to be sufficient feedback to avoid fragmentation and form a massive star. In Figure 7.1 all regions coloured in yellow have column densities above 1 gcm^{-2}, and this is where the majority of star formation is taking place. To illustrate this further, in Figure 7.5 the column density around the most massive sink in each clump is traced with time.

The column density around the central sink is calculated within a 0.15 pc box, which is taken as a reasonably typical size for a massive proto-stellar core. The column densities are calculated from material within the 3D clump radius, as anything outwith this region cannot be affected by the forming star. However, as shown in Table 7.2 contamination from material along the line of sight could increase these values by up to a factor of two. On the same plot as the column density the growth of the central sink is shown. In all cases it increases to form a massive star. The column densities surrounding the sinks are consistently above the 1 gcm^{-2} limit in the calculated region. However, the average column density of the clump as a whole is an order of magnitude below this value. Although the column density surrounding the star was above the threshold proposed by Krumholz, in Section 7.4.2 it will be shown that the massive stars were not formed from a single massive thermally supported fragment, but instead from a smaller core which accreted additional material channeled towards it by the potential of the forming stellar cluster. The high column densities, in this instance, seem mainly an indication of there being a large gas reservoir available for accretion.

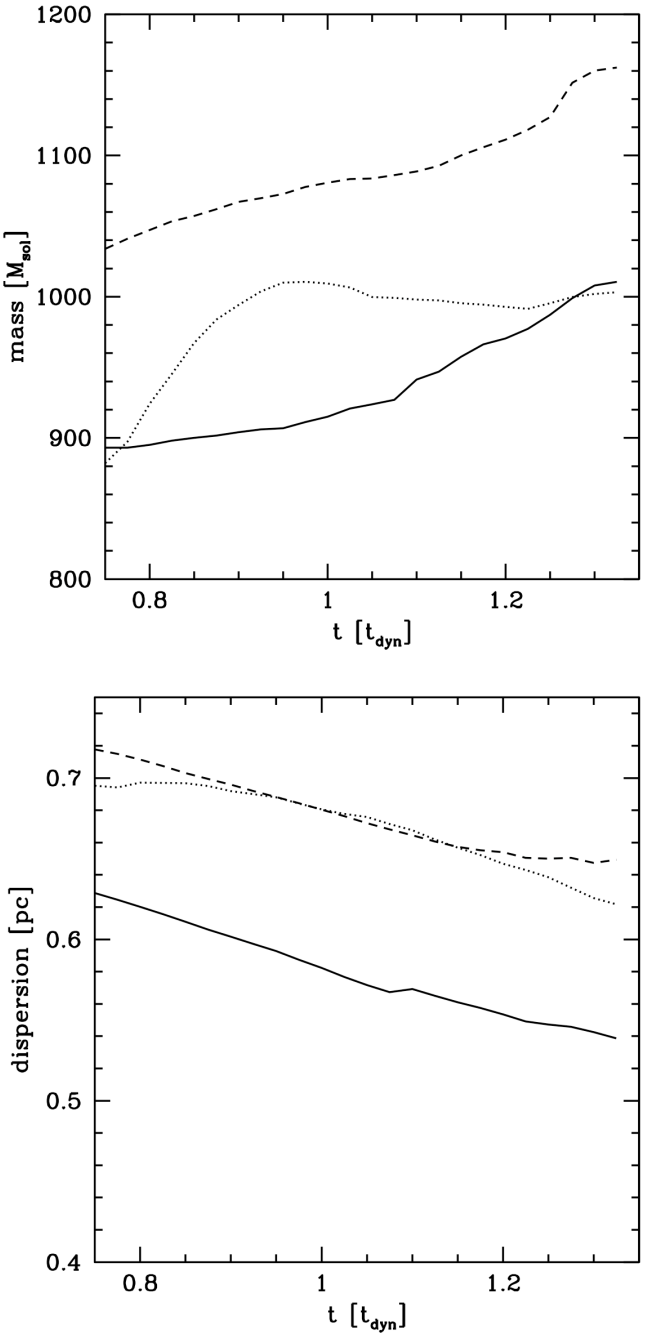

Figure 7.4: The global properties of the mass within 1 pc of the most massive sink for clumps Alpha *(solid line)*, Beta *(dotted line)* and Gamma *(dashed line)* . *Top*, the total mass and *bottom*, the mass weighted dispersion of matter plotted against the simulation dynamical time ($t_{dyn} \sim 4.7 \times 10^5$ yrs). The clump mass increases with time and becomes more concentrated.

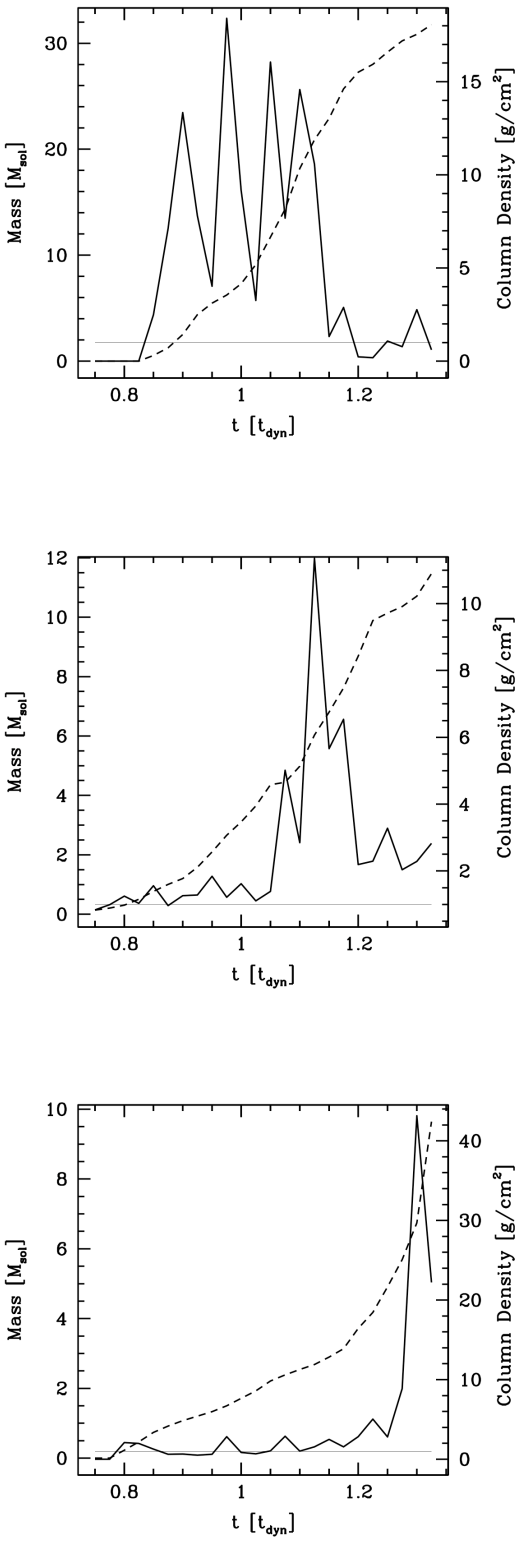

Figure 7.5: The masses and column densities around the central sink in clumps Alpha *top*, Beta *middle* and Gamma *bottom* plotted against the simulation dynamical time ($t_{dyn} \sim 4.7 \times 10^5$ yrs). The dashed line shows the sink mass and the solid line the column density calculated in a 0.15 pc box centered on the sink.

7.3.2 Observable Properties

The above analysis uses the full 3D data-set. However, a better comparison to observations can be made by generating and analysing synthetic dust continuum emission images. To create an observers' version of Figure 7.4 the simulated data is interpolated (including all material along the column) to a 2D grid of 66×66 grid cells, with a spatial resolution of 0.03 pc, comparable to recent observations (e.g. Zhang et al., 2009; Longmore, 2009). The flux is then calculated from each grid cell using the relationship

$$F(\nu) = \sum_{i=1,n} \frac{m_i g \kappa_\nu B_\nu(T_i)}{d^2} \tag{7.3}$$

where $F(\nu)$ is the flux in Jy, m_i is the mass of the SPH particle, g is the dust to gas ratio, κ_ν is the dust opacity, B_ν is the intrinsic emission of the SPH particle at temperature T_i according to the Planck equation and d is the distance at which the cloud is observed. The standard value of 0.01 is taken for the dust to gas ratio (Kauffmann et al., 2008) and a value of 0.1 m^2/kg for the dust opacity (Ossenkopf & Henning, 1994). The flux is calculated at a frequency of 230 GHz (1.3 mm) and distance of 5 kpc but these values do not affect the dispersion trends discussed below. Emission directly from sink particles is neglected, but they still contribute to their surrounding gas particles emission due to the heating described in Section 7.2. Figure 7.6 shows the emission in mJy from Clump Alpha at early and late times. The emission increases with time, particularly in the centre of the clump where the massive star is forming.

As before, a dispersion is calculated from the grid cells weighted by emission as shown in Eq. 7.4.

$$\sigma_{2D}(r) = \sqrt{\frac{\sum \xi_i (r_i - \bar{r})^2}{\sum \xi_i}} \tag{7.4}$$

where ξ_i is the emission from the grid cell i, and $r_i - \bar{r}$ is the distance from the grid cell where the largest sink is located. Figure 7.7 shows the total emission and dispersion of the clumps with time.

The total emission from the clumps roughly doubles over the time considered here (2.35×10^5 yrs). This is partially due to the increased mass of the clumps, but also due to increased emission from warmer dense gas where star formation is occurring. As in the three dimensional case a decreasing trend is seen in the dispersion. However, it is slightly less marked in emission due to the decreased resolution and the fact that only collapse along one plane is

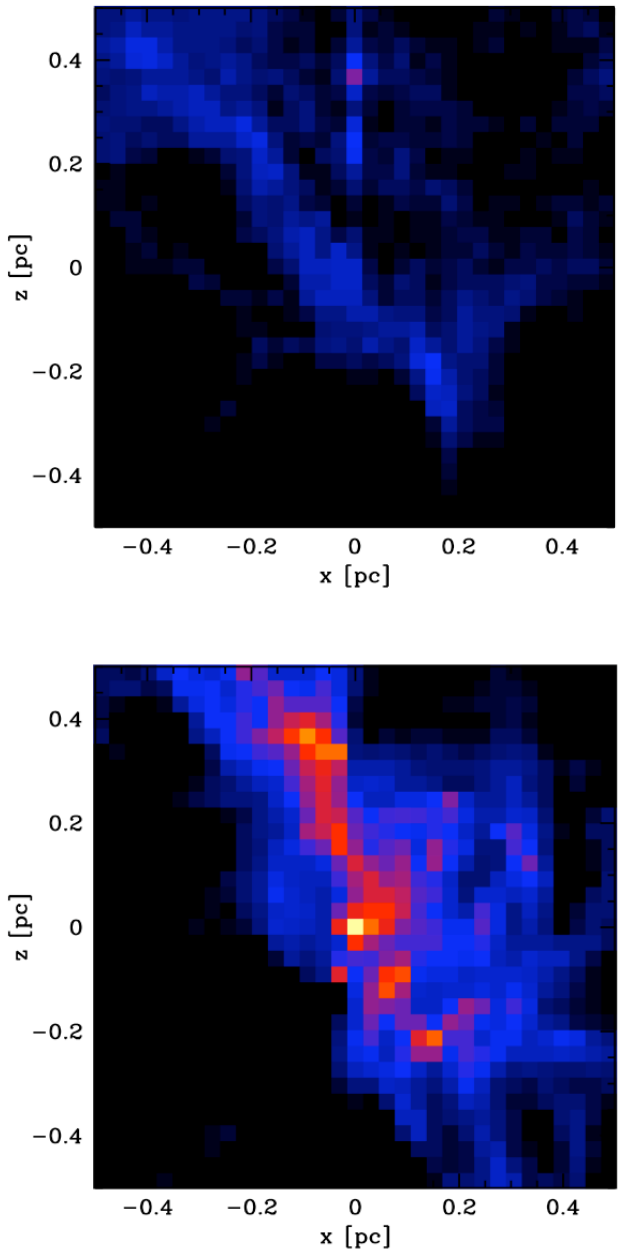

Figure 7.6: The dust continuum emission at 230 GHz from clump Alpha at *top* 0.75 t_{dyn} (3.53×10^5 yrs), and *bottom* 1.25 t_{dyn} (5.9×10^5 yrs). The colour scale denotes emission from 0.5 mJy (dark blue) to 500 mJy (yellow). As the clump becomes more evolved the emission from its centre, where the massive stars are forming, increases.

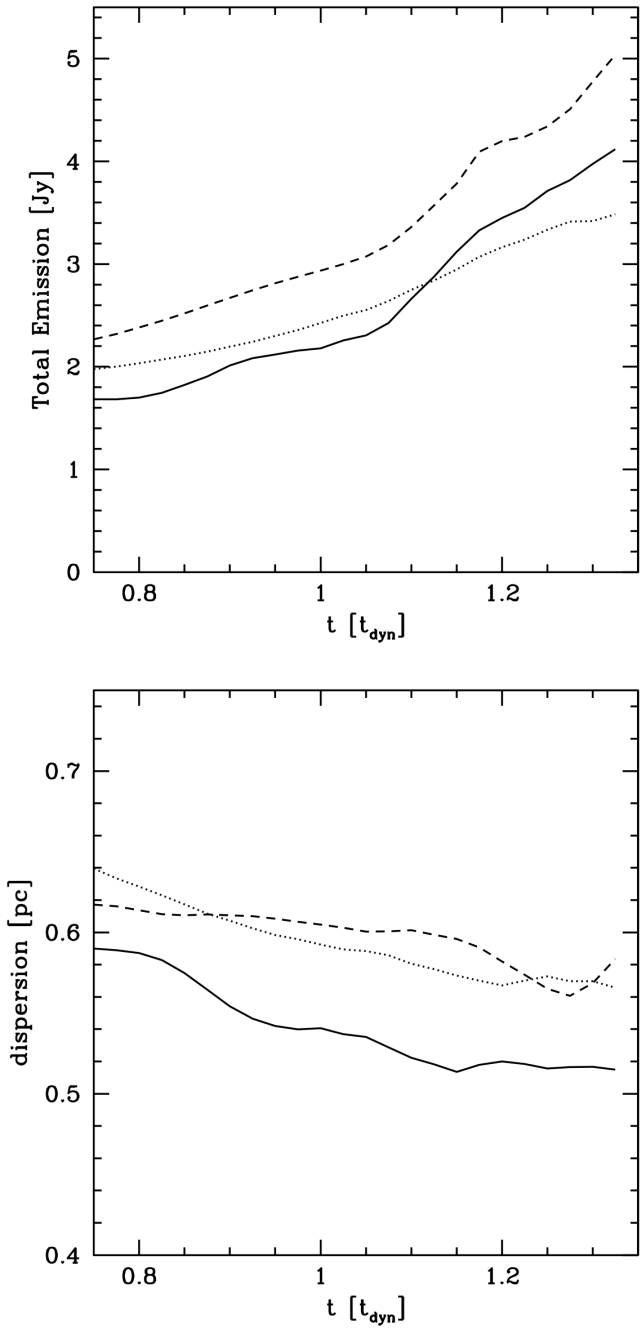

Figure 7.7: The observable properties of the mass within 1 pc of the most massive sink calculated from a 2D grid with a size resolution of 0.03 pc, plotted against the simulation dynamical time (t_{dyn} $\sim 4.7 \times 10^5$ yrs). The clumps are denoted by the following lines; Alpha *(solid line)*, Beta *(dotted line)* and Gamma *(dashed line)*. The panels show: *top*, the total emission from the clump and *bottom*, the emission weighted dispersion.

visible.

7.3.3 Direct Comparison to Observations

Now the evolution of molecular gas structure predicted above shall be directly compared to observations. This section was principally carried out by Steven Longmore.

Longmore et. al 2009 (L09) recently observed 6 massive star formation regions at 3 different evolutionary stages prior to UCHII region formation using the Submillimeter Array at 230GHz to image the thermal dust continuum emission. They found the dust continuum emission to be weaker and more spatially extended at early stages and becoming more centrally concentrated with time. As the global properties of the L09 regions are similar to those of Alpha, Beta and Gamma, this dataset offers an excellent opportunity for comparison with the simulations.

The synthetic flux image was generated from the numerical simulation in the same way described above. To take account of the spatial filtering inherent in the interferometric observations, the simulated image was then sampled with the same uv-coverage as the L09 observations. The resulting synthetic 230GHz flux distributions towards Alpha, Beta and Gamma (at the same time steps as Figure 7.1) are shown in Figures 7.8, 7.9 and 7.10.

The difference in source structure compared to Figures 7.1, 7.2 and 7.3 is striking. All of the largest scale extended emission has been filtered-out and the images are instead dominated by the regions of highest density contrast. The much coarser resolution cannot distinguish most of the fine detail, which is instead convolved into a smaller number of unresolved or partially-resolved sources.

The flux scale in each image, in units of Jy, is given by the colour bar. In all three regions the emission is a lot weaker at earlier times as the gas is more dispersed and cooler. Significantly more structure is seen at these earlier times down to the L09 sensitivity limit ($\sim$1 mJy) However, sensitivity is clearly an issue here – more shallow observations would miss the weaker sources.

The contours in Figure 7.8 show the flux levels in the images in 10% steps of the peak value. In all three regions, at early times the many sources in the field have similar flux densities. As the clump collapses its density decreases in its outer regions and increases at its centre. Moreover, the collapse feeds massive star formation at the centre of the clump, which

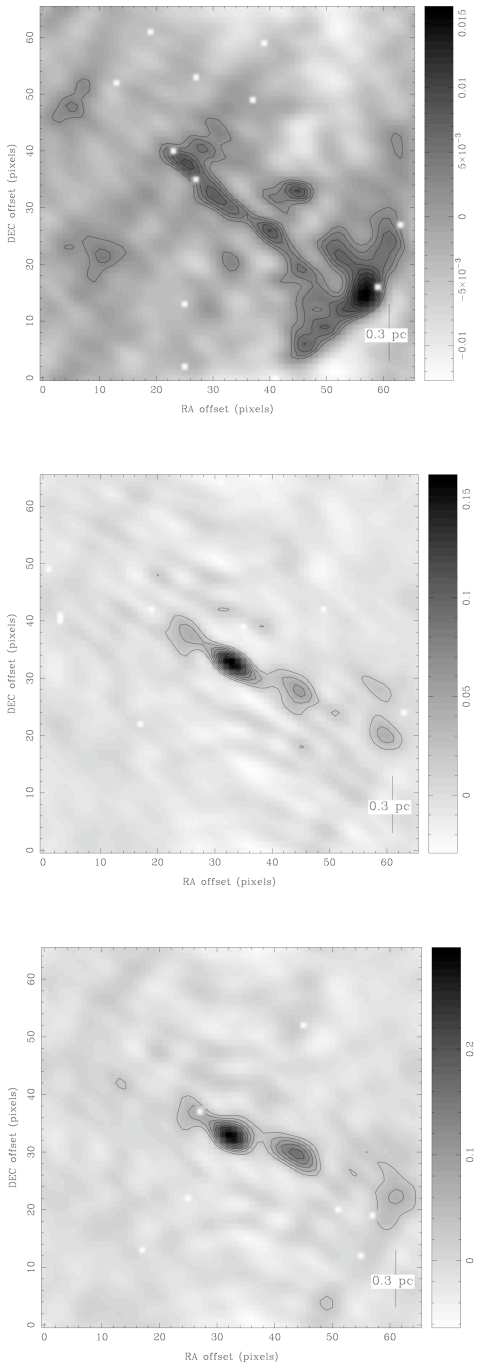

Figure 7.8: Simulated interferometry observations of clump Alpha *top* at the same time intervals as shown in Figure 7.1.

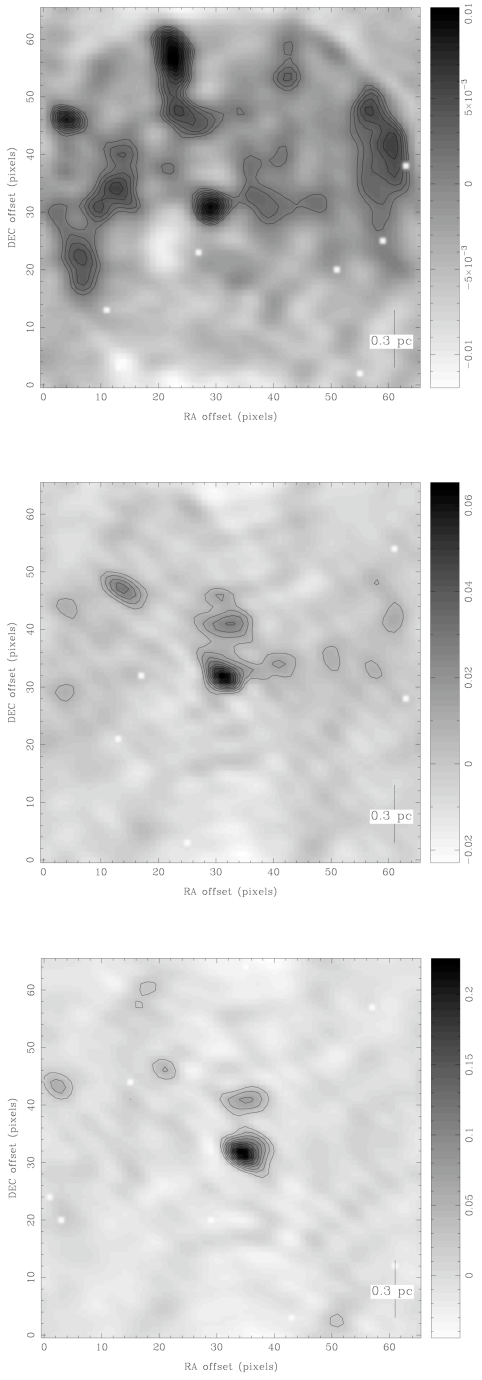

Figure 7.9: Simulated interferometry observations of clump Beta *middle* at the same time intervals as shown in Figure 7.2.

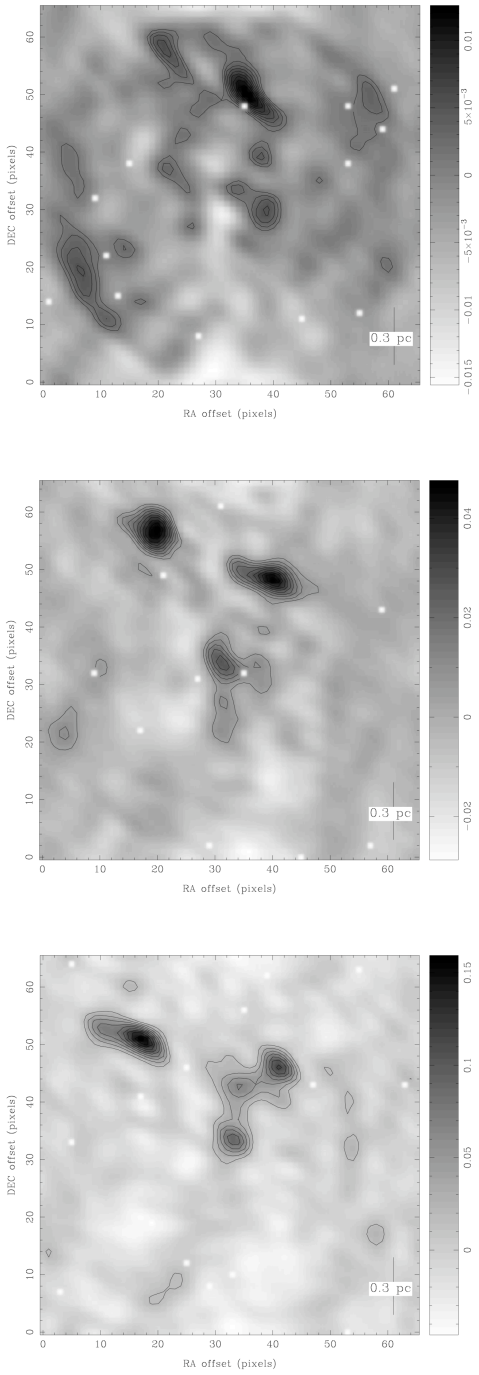

Figure 7.10: Simulated interferometry observations of clump Gamma *bottom* at the same time intervals as shown in Figure 7.3.

heats the surrounding gas. This leads to the emission becoming dominated by one or two sources which are significantly hotter/denser than the surrounding cores. In real observations this may lead to dynamic range problems – typical submm and mm interferometer images are limited to dynamic ranges of few hundred at best.

7.4 Discussion

7.4.1 Collapse and Accretion

The evolution of the stellar cluster and the massive stars are intrinsically linked by the overall cluster potential and the accretion it induces. As the clump of gas evolves towards a stellar cluster it goes through several evolutionary stages. First, the clump becomes bound due to dissipation of turbulent energy, and the density enhancements within it begin to form bound cores. Secondly, as the clump becomes over-bound it undergoes global collapse which channels mass towards its centre, creating a large reservoir of gas. Thirdly, this gas will be accreted by the proto-stars with the largest accretion radii. Bonnell et al. (2001) showed that for a collapsing system where the gas velocities and proto-stellar velocities are similar, the tidal radius is the most appropriate accretion radius. From analogy with the Roche Lobe formalism the tidal radius is,

$$R_{acc} = C_{tidal} \left(\frac{M_*}{M_{enc}} \right)^{1/3} r_* \tag{7.5}$$

where M_* is the stellar mass, M_{enc} is the mass enclosed within the cluster at the star's position r_* and $C = 0.5$ from the Roche Lobe approximation (Eggleton, 1983). This gives a mass accretion rate of

$$\dot{M}_* \approx \pi \rho v_{rel} R_{acc}^2 \tag{7.6}$$

where $\dot{M}_*$ is the accretion rate and v_{rel} is the relative velocity between the proto-star and the gas. So the most massive star in a region is the most effective at gaining additional mass. There is also an additional boost to the accretion rate of the massive stars at the centre of the cluster from the enhancement of the local density by global in-fall.

The above analysis considers the initial evolution of the cluster when the gas and stellar velocities are well correlated. However, once the cluster becomes virialised and the gas and stellar velocities are no longer correlated, the massive stars will become even more efficient

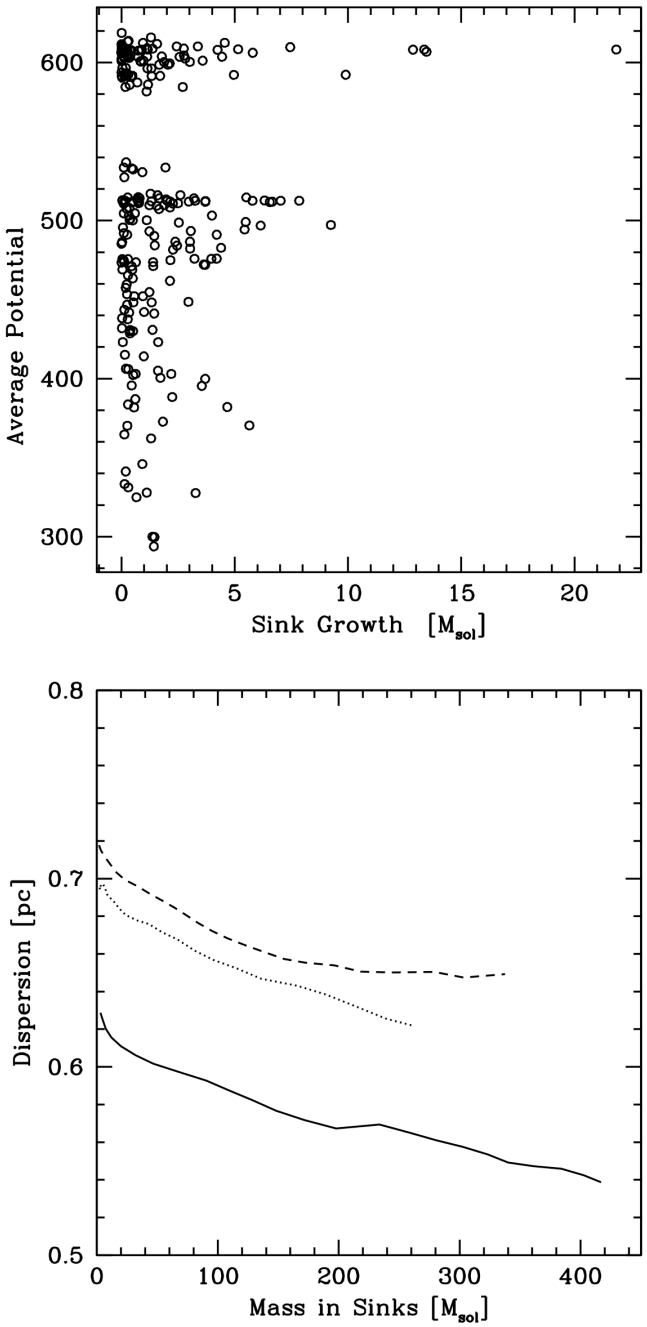

Figure 7.11: The connection between clumps and sink masses during accretion. *Top* the growth in sink mass over a period of 0.25 t_{dyn} plotted against the average potential in code units of the mass within a pc radius of the sink. The sinks in the deepest potential well grow the most significantly. *Bottom* the mass in sinks within regions Alpha *solid line*, Beta *dotted line* and Gamma *dashed line* plotted against their dispersion. The mass in sinks grows as the clump becomes more concentrated.

accretors (Zinnecker, 1982; Bonnell et al., 2001).

Figure 7.11 illustrates the connection between the clump collapse and accretion in the simulation. The top panel shows the growth in sink mass over a period of 0.25 t_{dyn} (t_{dyn} $\sim 4.7 \times 10^5$ yrs) plotted against the average eventual gravitational potential of the mass within a parsec radius of the most massive sink. Clump Alpha can be seen as a horizontal line of equi-potential along the top of the graph. The greatest growth in sink mass occurs in clump Alpha which has the deepest potential well. The greater potential shows that more mass has been concentrated in the centre, which acts to focus additional mass towards the massive sinks. This effect is not just due to limited numbers: there are 99 sinks whose environment has an average potential above 550 code units and 157 below this value, but the three sinks which grow the most are all contained in the upper subset. This shows that the mass of the massive stars are linked to their environment. It is also worth noting that most of the stars in clump Alpha do remain as low-mass objects, and that these constitute the bulk of the stars within the stellar cluster formed from this clump.

The bottom panel of Figure 7.11 shows the total mass converted to sink particles in the three clumps plotted against their dispersion. The total mass in sinks increases as the clumps become more concentrated. In other words, the clump contracts and changes its distribution as it forms a stellar cluster. This evolution happens simultaneously with the evolution of the massive stars and affects their accretion.

7.4.2 Clump-Core Interaction

Let us next consider how the clump and cores interact during global collapse. Chapter 6 demonstrated that the mass function of bound cores was indeed similar to the IMF, but the mapping between individual cores and their final stellar mass was poor. It was concluded that this was mainly due to environmental factors. To investigate this further in Figure 7.12, the fate of the mass within clump Alpha is shown at $1t_{dyn}$. Clump Alpha is used for illustration here as it has the simplest structure and contains the most massive sinks. The figure is colour coded to indicate the eventual fate of all the SPH mass particles at the end of the simulation. Green material will be accreted by the central massive sink (red dot). Black dots show the position of other sinks and blue regions show the location of material in gas cores. The cores are the 'p-cores' introduced in Chapter 4. In figure 7.12 the blue cores will contain a black dot denoting a sink if they are proto-stellar, a hollow black dot if they are pre-stellar, and none if

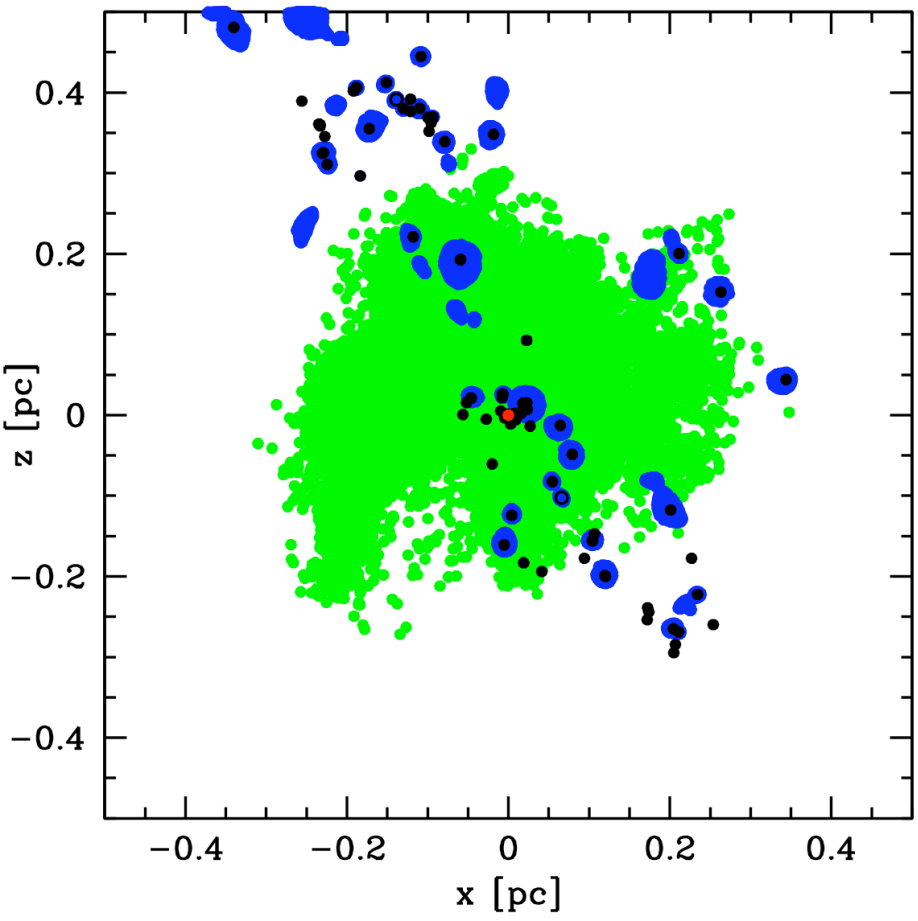

Figure 7.12: The final fate of the mass within clump Alpha shown at 1 t_{dyn}. The green dots show the positions of gas which will eventually be accreted by the massive sink (red dot). Black dots show the position of sinks and blue dots show the location of material in cores. The gas which will be accreted by the massive sinks is well distributed throughout the clumps, and generally cores within this region will not be disrupted by the massive sink.

they are unbound.

The gas which will be accreted by the massive sink is well distributed throughout the clump, and it comes from a larger area than the typical size of a p-core. The p-cores sit within the volume from which mass will be accreted by the central massive sink, but are largely unaffected by this. Only the proto-stellar core directly to the left of the massive central sink gets disrupted due to heating. Additionally, an unbound core above the massive sinks is also destroyed and then accreted by the central sink before it can become bound. To illustrate why most of the low mass proto-stellar cores are unaffected by accretion from the central sink, their respective densities are plotted in Figure 7.13.

The top panel of Figure 7.13 shows at $t_{dyn} = 1$, the densities of SPH particles which will

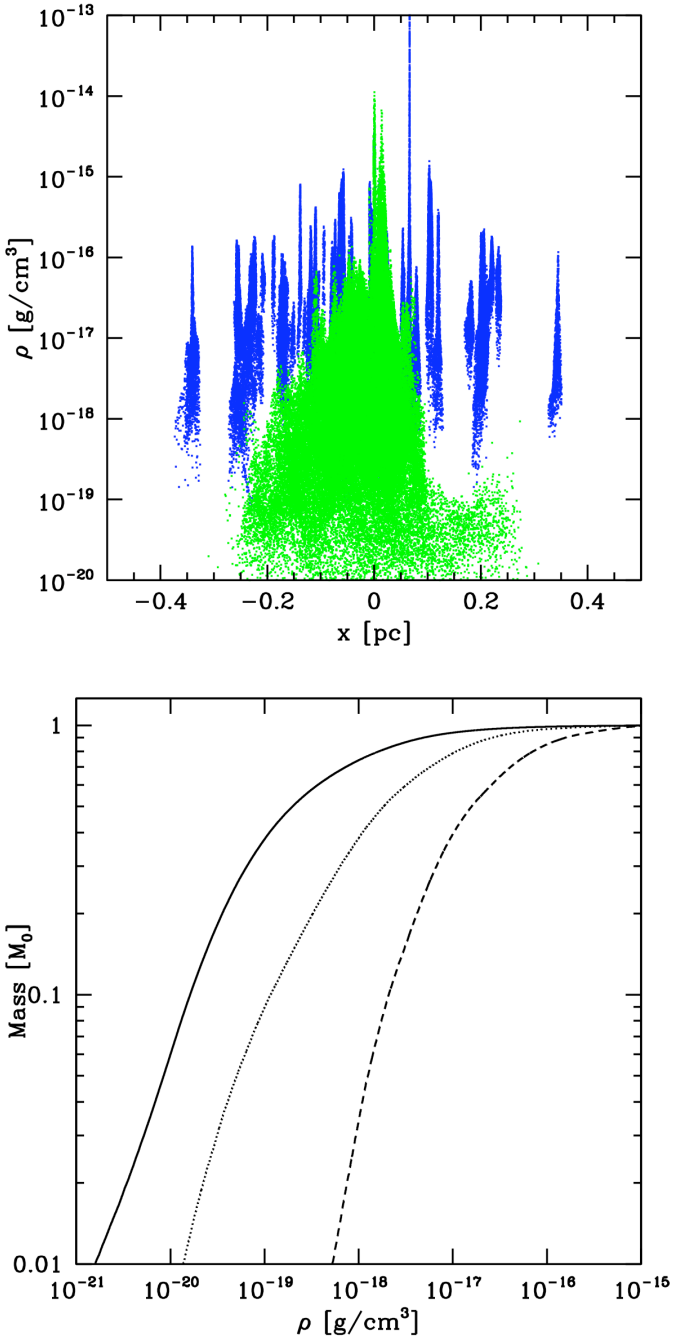

Figure 7.13: *Top* The density distribution of the material which will be accreted by the central sink in clump A (green), compared to that of the material in cores at $t_{dyn} = 1$ (blue). *Bottom* The cumulative density distribution of the entire clump (solid), material which will be accreted by the central sink (long dashed) and material in cores (short dashed). The masses have been normalised to magnitude one, to ease comparison. The material identified in cores contains mainly high density gas, whereas the material which will be accreted by the central sink contains significant amounts of low density gas.

later be accreted by the central sink in green, and the densities of the particles in cores in blue. The accreted material extends to low densities, whereas the gas in cores is confined to higher densities. As the free fall time of the gas is proportional to density as $t_{ff} \propto \rho^{-1/2}$, the cores have short dynamical times and can collapse before they can be accreted. The lower density gas between the cores has a longer free fall time and therefore can be accreted by the central sink. This can be seen in the way that the density of accreted gas decreases with distance from the massive sink, as it needs to have a longer free fall time in order to successfully reach the sink.

The bottom panel of Figure 7.13 shows the gas density plotted against cumulative mass for clump Alpha as a whole, the accreted material, and the cores. The material in cores has characteristic densities, $\rho_c \sim 10^{-17}$ gcm^{-3}, the accreted material has $\rho_c \sim 10^{-18}$ gcm^{-3}, and the clump as a whole has $\rho_c \sim 10^{-19}$ gcm^{-3}. Once again, this shows that the accreted material has a wider initial density distribution range than the cores. It also shows that if the respective distributions were observed above a density threshold, the mass available for accretion would be underestimated. For instance, over 20% of the mass accreted by the central sink has a density below the minimum seen in cores.

A major difference between this and other models of high mass star formation is that within a typical massive star forming clump, there are smaller proto-stellar cores forming low mass stars close to where the high mass star is forming ($r < 0.15$ pc), and within the region which it accretes from. This would be most apparent at early times in the evolution of the clump when it is still diffuse, before the cores have become concentrated at the centre, and the emission becomes dominated by the central source.

7.4.3 Massive Star Progenitors

When the original progenitor of the massive sink was searched for using the p-core routine, it was found to be a bound core containing 0.67 $M_\odot$. This is very close to the mean bound p-core mass of 0.7 $M_\odot$, and is an order of magnitude lower than the final mass of 29.2 $M_\odot$ the sink achieved by the end of the simulation. Similarly, for the other clumps studied here, their most massive sinks are found to originate from intermediate-mass pre-stellar cores which become massive proto-stars via accretion. Therefore, the mass which forms the massive star comes mainly from the larger clump, rather than from a well defined massive pre-stellar core. In this scenario initially there is a low-to-intermediate pre-stellar core at the centre of the potential

which grows to a massive condensation (YSO) as the clump collapses. It does not matter if smaller fragments form around this object, as the evolving clump continues to channel mass towards it.

7.5 Conclusions

I have carried out SPH simulations of a giant molecular cloud with a simplified radiative feedback model. From this simulation three gas clumps of radius 1 pc were identified which are the progenitors of stellar clusters. It was found that the formation of a stellar cluster occurs simultaneously with massive star formation. The evolution of the two are therefore intrinsically linked. This leads to the following predictions.

1. Massive clump structure is originally diffuse and filamentary, but evolves into a more concentrated structure by means of gravitational contraction.

2. The models presented here are in good agreement to the interferometry observations of Longmore et al. (in preparation). Simulated interferometry images show more structure at early times, and less at later times when the emission is dominated by hot, dense central sources.

3. Both the most massive stars and the most massive stellar cluster are formed within the most bound clump. This is despite it being the least massive of the three clumps studied.

4. The gravitational potential of the gas clumps causes global collapse, which continuously channels mass from large radii towards the centre of the cluster, where it is accreted by the progenitors of the massive stars.

5. The original pre-stellar core of the most massive sink formed was only of intermediate mass. Most of the mass which goes into the sink originally came from the less dense clump gas between the surrounding low mass cores.

8

Conclusions

Since the local observations of Salpeter (1955), it has been found that the initial mass distribution of newly formed stars has a characteristic profile (Kroupa, 2002). Thus, explaining the origins of the initial mass function is a key requirement of any theory of star formation. The observations of Motte et al. (1998), that the mass function of cores of gas within molecular clouds also exhibits this profile, has lead to suggestions (eg. Alves et al., 2007) that there might be a direct correspondence between core masses and the stellar masses formed from them. Stars are formed in cores due to their high densities and low Jeans masses, however to what extent their masses correlate is unknown.

One of the first difficulties is simply defining a core, as unlike stars, they are not discrete objects, but instead join smoothly on to a continuous hierarchy of structure within a molecular cloud. Core boundary definitions, and therefore their masses, are at least to some extent arbitrary as they are influenced by effects such as resolution, noise, orientation and the properties of the observable used to trace them. This makes it difficult to clearly link the properties of cores and stellar systems. Moreover, while a core is collapsing to form a stellar system it is

still evolving within a larger clump of gas where other stars are forming. The forming star may be influenced by this environment through dynamic interactions or competitive accretion (Bonnell et al., 2004).

A further problem in forming stars entirely from well defined cores with no outside influences is the difficulty of forming massive stars. Massive core are liable to further fragmentation, which would instead form several smaller stars instead of one massive star. It has been contended that support from turbulence (McKee & Tan, 2003), or radiative feedback (Krumholz, 2006) may prevent fragmentation, although simulations by Dobbs et al. (2005) have thrown doubt on this.

In this thesis the link between the earliest fragmentation in molecular clouds and the stars formed from them has been probed through SPH simulations of molecular clouds. By using large scale simulation we are able to study star formation across all the masses seen in the IMF, and to study the interactions of the first bound cores with their larger environments.

In addition to using the standard CLUMPFIND method (Williams et al., 1994) which has been modified for SPH data by Paul Clark, a new method of clump-finding using gravitational potential was introduced. This allowed gravitational potential wells to be found, and bound structures to be identified with respect to their environments. The major results from this thesis will now be outlined below.

8.1 The Universality of the Clump Mass Function

In Chapter 5 the clump-finding algorithm was tested to determine how consistent the results were when applied to differing data-sets and at differing resolutions. By using a simulation of a star-forming region in a molecular cloud as a standard reference, it was shown that the emergence of a clump mass function resembling the stellar initial mass function is a ubiquitous feature of molecular cloud structure. Three different techniques were used to extract the clumps used for this comparison. In the first two, the SPH particle data was interpolated to 2 and 3 dimensional grids before performing the clump-find, using position-position (PP) and position-position-velocity (PPV) information respectively. In the third technique, the clump-finding is performed on the SPH data directly, making use of the full 3 dimensional position information. Although the CMF is typically similar to that observed in regions of nearby star formation, the individual clumps and their masses are found to be unreliable since they

depend strongly on the parameters and the method of the clump-finding. In particular it was found that the resolution and orientation of the data make a significant difference to the resulting properties of the identified clumps in the PP and PPV cases. In conclusion, comparisons between a CMF and the stellar IMF should be made with caution, since the definition of a clump boundary, and hence the number of clumps and their properties, are arbitrary in the extraction method. This is especially true if molecular clouds are truly scale free.

8.2 The Earliest Fragmentation in Molecular Clouds

Having ascertained that core boundaries are unreliable, the next step was to determine a more consistent and reliable method of identifying cores. As outlined in Chapter 4, a clumpfind using gravitational potential instead of density has several advantages. Gravitational potential has a smoother distribution and clearer boundaries than density. Additionally, the depth of the identified potential well gives an indication of future collapse, as bound potential cores (p-cores) represent the earliest stages of fragmentation in molecular clouds.

In Chapter 6 the potential clump-finding routine was used to identify star-forming gas cores in an SPH simulation of a Giant Molecular Cloud. It was found that the mass function of the p-cores genuinely resembles the stellar IMF and the observed clump mass function, although p-core masses (~ 0.7 $M_\odot$) are smaller than typical density cores. The bound p-cores are generally subsonic, have internal substructure, and are only quasi-spherical. There was no evidence of massive bound cores supported by turbulence. The evolution of the p-cores was traced forward in time which enabled the connection between the original p-core mass and the stellar mass that formed from it to be investigated. Although there was a trend of increasing stellar mass with core mass, the correlation was poor and there was considerable scatter. This suggests that accretion onto the forming proto-star is dependent on more factors than just the initial core mass. During the accretion process the p-cores accrete from beyond the region first bound, highlighting the importance of the core environment to its subsequent evolution.

8.3 Massive Stars and Stellar Clusters

Finally in Chapter 7 the role of accretion onto cores from their environment was studied in more detail. As no massive pre-stellar cores were found in Chapter 6 this is particularly relevant for massive star formation. Using the same simulation as in the previous chapter it was shown that massive stars and stellar clusters are formed simultaneously, and it is the global evolution of the forming cluster that allows the central stars to become massive.

It is predicted that massive star forming clumps, such as those observed in Motte et al. (2007), contract and grow in mass, leading to the formation of both stellar clusters and massive stars. This occurs as mass is continually channeled from large radii onto the central proto-stars, which can become massive through accretion. In the simulated GMC, clumps are initially diffuse and filamentary, and become more concentrated as they collapse. Simulated interferometry observations of the clumps provide an explanation as to why young massive star forming regions show more substructure than older ones. The most massive stars in the simulation are found within the most bound cluster. Most of the mass accreted by the massive stars was originally distributed throughout the clump at low densities, and was later funneled to the star due to global in-fall. Even with radiative feedback no massive pre-stellar cores were formed. The original cores were of intermediate mass and gain their additional mass in the proto-stellar stage. It was also found that cores which form low mass stars exist within the volume from which the high mass stars accrete, but are largely unaffected by this process.

8.4 Summary

In summary, observed core boundaries can be arbitrary and great care should be used when deducing core masses. However the underlying mass function of bound cores in our simulations did resemble the IMF. The first bound fragments identified were subsonic and have masses similar to stellar masses. These fragments collapsed to form stars. The connection between the cores and the stellar systems formed from them is complex and depends in part on the environment of the core. Although there was a trend for increasingly massive cores to form more massive stars, for individual cores there was too much variability to predict the mass of the stellar system formed. The role of accretion from the environment was particularly significant for the formation of massive stars. In this case, the global collapse of the surrounding clump directly affects the evolution of the massive star. The overall binding of

the larger clump as a whole appeared to increase efficiency of the star formation as regards both the number of stars formed and the most massive stars formed.

In conclusion there is a connection between the IMF and the core mass function. However, in the dynamic clustered environment of molecular clouds, this connection cannot be solely determined from the original core mass. The cores will indeed collapse to form stars, but there is often an additional contribution to the stellar masses from subsequent accretion after the initial core has become bound. Therefore the stellar masses formed from cores depends both on the initial core mass and the surrounding environment of the core.

Bibliography

Agertz, O. et al. 2007, MNRAS, 380, 963, arXiv:astro-ph/0610051

Alves, J., Lombardi, M., & Lada, C. J. 2007, A&A, 462, L17, arXiv:astro-ph/0612126

André, P., Belloche, A., Motte, F., & Peretto, N. 2007, A&A, 472, 519, arXiv:0706.1535

André, P. et al. 2008, A&A, 490, L27, 0809.3968

Andre, P., Ward-Thompson, D., & Barsony, M. 2000, Protostars and Planets IV, 59, arXiv:astro-ph/9903284

Ballesteros-Paredes, J. 2004, Astrophysics & Space Science, 289, 243, arXiv:astro-ph/0212580

Ballesteros-Paredes, J., Hartmann, L., & Vázquez-Semadeni, E. 1999a, The Astrophysical Journal, 527, 285, astro-ph/9907053

Ballesteros-Paredes, J., Klessen, R. S., & Vázquez-Semadeni, E. 2003, ApJ, 592, 188, arXiv:astro-ph/0304008

Ballesteros-Paredes, J., & Mac Low, M.-M. 2002, ApJ, 570, 734, arXiv:astro-ph/0108136

Ballesteros-Paredes, J., Vázquez-Semadeni, E., & Scalo, J. 1999b, ApJ, 515, 286, arXiv:astro-ph/9806059

Bate, M. R. 1995, Ph.D Thesis, 68

——. 2009, MNRAS, 392, 1363, 0811.1035

Bate, M. R., & Bonnell, I. A. 2005, MNRAS, 356, 1201, arXiv:astro-ph/0411084

Bate, M. R., Bonnell, I. A., & Price, N. M. 1995, MNRAS, 277, 362, arXiv:astro-ph/9510149

Bate, M. R., & Burkert, A. 1997, MNRAS, 288, 1060

Benz, W. 1990, in Numerical Modelling of Nonlinear Stellar Pulsations Problems and Prospects, ed. J. R. Buchler (Dordrecht, The Netherlands: Kluwer Academic Publishers), 269–+

Bergin, E. A., & Tafalla, M. 2007, ARA&A, 45, 339, arXiv:0705.3765

Beuther, H., Schilke, P., Menten, K. M., Motte, F., Sridharan, T. K., & Wyrowski, F. 2002, ApJ, 566, 945, arXiv:astro-ph/0110370

Binney, J., & Tremaine, S. 1987, Galactic dynamics (Princeton, NJ, Princeton University Press, 1987, 747 p.)

Blitz, L. 1993, in Protostars and Planets III, ed. E. H. Levy & J. I. Lunine, 125–161

Blitz, L., & Shu, F. H. 1980, The Astrophysical Journal, 238, 148

Bok, B. J., & Reilly, E. F. 1947, ApJ, 105, 255

Bonnell, I. A., & Bate, M. R. 2006, MNRAS, 370, 488, arXiv:astro-ph/0604615

Bonnell, I. A., Bate, M. R., Clarke, C. J., & Pringle, J. E. 1997, MNRAS, 285, 201

——. 2001, MNRAS, 323, 785, arXiv:astro-ph/0102074

Bonnell, I. A., Bate, M. R., & Zinnecker, H. 1998, MNRAS, 298, 93, arXiv:astro-ph/9802332

Bonnell, I. A., Clark, P., & Bate, M. R. 2008, MNRAS, 389, 1556, 0807.0460

Bonnell, I. A., Vine, S. G., & Bate, M. R. 2004, MNRAS, 349, 735, arXiv:astro-ph/0401059

Bonnor, W. B. 1956, MNRAS, 116, 351

Bourke, T. L., Myers, P. C., Robinson, G., & Hyland, A. R. 2001, The Astrophysical Journal, 554, 916, astro-ph/0102469

Brunt, C. M., & Mac Low, M.-M. 2004, ApJ, 604, 196, arXiv:astro-ph/0311461

Carey, S. J., Clark, F. O., Egan, M. P., Price, S. D., Shipman, R. F., & Kuchar, T. A. 1998, ApJ, 508, 721

Carey, S. J., Feldman, P. A., Redman, R. O., Egan, M. P., MacLeod, J. M., & Price, S. D. 2000, ApJL, 543, L157

Chabrier, G. 2002, ApJ, 567, 304, arXiv:astro-ph/0110024

——. 2003, PASP, 115, 763, arXiv:astro-ph/0304382

Clark, P. C., & Bonnell, I. A. 2005, MNRAS, 361, 2

Clark, P. C., Klessen, R. S., & Bonnell, I. A. 2007, MNRAS, 379, 57, arXiv:0704.2837

Crutcher, R. M. 1999, The Astrophysical Journal, 520, 706

Crutcher, R. M., Hakobian, N., & Troland, T. H. 2009, ApJ, 692, 844, 0807.2862

Crutcher, R. M., Troland, T. H., Goodman, A. A., Heiles, C., Kazes, I., & Myers, P. C. 1993, ApJ, 407, 175

Dale, J. E., & Bonnell, I. A. 2008, MNRAS, 391, 2, 0808.1510

di Francesco, J., Evans, II, N. J., Caselli, P., Myers, P. C., Shirley, Y., Aikawa, Y., & Tafalla, M. 2007, in Protostars and Planets V, ed. B. Reipurth, D. Jewitt, & K. Keil (Tucson: University of Arizona Press), 17–32

Dobbs, C. L. 2006, Ph.D Thesis, 20

Dobbs, C. L., & Bonnell, I. A. 2007, Monthly Notices of the Royal Astronomical Society, 376, 1747

Dobbs, C. L., Bonnell, I. A., & Clark, P. C. 2005, MNRAS, 360, 2, arXiv:astro-ph/0502479

Dubinski, J., Narayan, R., & Phillips, T. G. 1995, ApJ, 448, 226, arXiv:astro-ph/9501032

Ebert, R. 1955, Zeitschrift fur Astrophysik, 37, 217

Egan, M. P., Shipman, R. F., Price, S. D., Carey, S. J., Clark, F. O., & Cohen, M. 1998, ApJL, 494, L199+

Eggleton, P. P. 1983, ApJ, 268, 368

Elmegreen, B. G. 1993, ApJL, 419, L29+

——. 1997, ApJ, 486, 944

——. 2000, ApJ, 530, 277, arXiv:astro-ph/9911172

——. 2002, ApJ, 564, 773, arXiv:astro-ph/0112528

Elmegreen, B. G., Klessen, R. S., & Wilson, C. D. 2008, ApJ, 681, 365, 0803.4411

Elmegreen, B. G., & Mathieu, R. D. 1983, MNRAS, 203, 305

Enoch, M. L., Evans, II, N. J., Sargent, A. I., Glenn, J., Rosolowsky, E., & Myers, P. 2008, ApJ, 684, 1240, 0805.1075

Enoch, M. L. et al. 2006, The Astrophysical Journal, 638, 293, astro-ph/0510202

Faúndez, S., Bronfman, L., Garay, G., Chini, R., Nyman, L.-Å., & May, J. 2004, A&A, 426, 97

Fűrész, G., Hartmann, L. W., Megeath, S. T., Szentgyorgyi, A. H., & Hamden, E. T. 2008, ApJ, 676, 1109, 0711.0391

Fleck, Jr., R. C. 1982, MNRAS, 201, 551

Foster, P. N., & Chevalier, R. A. 1993, ApJ, 416, 303

Gingold, R. A., & Monaghan, J. J. 1977, MNRAS, 181, 375

Goldsmith, P. F., & Langer, W. D. 1978, The Astrophysical Journal, 222, 881

Goodman, A. A., Barranco, J. A., Wilner, D. J., & Heyer, M. H. 1998, ApJ, 504, 223

Goodman, A. A., Benson, P. J., Fuller, G. A., & Myers, P. C. 1993, ApJ, 406, 528

Goodwin, S. P., Nutter, D., Kroupa, P., Ward-Thompson, D., & Whitworth, A. P. 2008, A&A, 477, 823, 0711.1749

Gotoh, T., & Kraichnan, R. H. 1993, Physics of Fluids, 5, 445

Hartmann, L. 2003, ApJ, 585, 398, arXiv:astro-ph/0211021

Hartmann, L., & Burkert, A. 2007, ApJ, 654, 988, arXiv:astro-ph/0609679

Hatchell, J., & Fuller, G. A. 2008, A&A, 482, 855, 0803.1064

Heitsch, F., Mac Low, M.-M., & Klessen, R. S. 2001, ApJ, 547, 280, arXiv:astro-ph/0009227

Heitsch, F., Slyz, A. D., Devriendt, J. E. G., Hartmann, L. W., & Burkert, A. 2006, ApJ, 648, 1052, arXiv:astro-ph/0605435

Hennebelle, P., & Chabrier, G. 2008, ArXiv e-prints, 805, 0805.0691

Hennebelle, P., & Passot, T. 2006, A&A, 448, 1083, arXiv:astro-ph/0510425

Henriksen, R. N. 1986, ApJ, 310, 189

Heyer, M. H., & Brunt, C. M. 2004, ApJL, 615, L45, arXiv:astro-ph/0409420

Hillenbrand, L. A. 1997, AJ, 113, 1733

Hunter, C. 1977, ApJ, 218, 834

Ikeda, N., Sunada, K., & Kitamura, Y. 2007, ApJ, 665, 1194

Jappsen, A.-K., Klessen, R. S., Larson, R. B., Li, Y., & Mac Low, M.-M. 2005, A&A, 435, 611, arXiv:astro-ph/0410351

Jeans, J. H. 1902, Philosophical Transactions of the Royal Society of London. Series A, Containing Papers of a Mathematical or Physical Character, 199, 1

Johnstone, D., Di Francesco, J., & Kirk, H. 2004, ApJL, 611, L45, arXiv:astro-ph/0406640

Johnstone, D., Matthews, H., & Mitchell, G. F. 2006, ApJ, 639, 259, arXiv:astro-ph/0512382

Johnstone, D., Wilson, C. D., Moriarty-Schieven, G., Joncas, G., Smith, G., Gregersen, E., & Fich, M. 2000, ApJ, 545, 327

Kainulainen, J., Lada, C. J., Rathborne, J. M., & Alves, J. F. 2009, ArXiv e-prints, 0901.4207

Kauffmann, J., Bertoldi, F., Bourke, T. L., Evans, II, N. J., & Lee, C. W. 2008, A&A, 487, 993, 0805.4205

Keto, E. 2007, ApJ, 666, 976, arXiv:astro-ph/0603856

Klessen, R. S. 2001, ApJ, 556, 837, arXiv:astro-ph/0104127

Klessen, R. S., & Burkert, A. 2000, ApJS, 128, 287, arXiv:astro-ph/9904090

Kramer, C., Stutzki, J., Rohrig, R., & Corneliussen, U. 1998, A&A, 329, 249

Kroupa, P. 2002, Science, 295, 82, arXiv:astro-ph/0201098

Krumholz, M. R. 2006, ApJL, 641, L45, arXiv:astro-ph/0603026

Krumholz, M. R., Klein, R. I., & McKee, C. F. 2007, ApJ, 656, 959, arXiv:astro-ph/0609798

Krumholz, M. R., & McKee, C. F. 2008, Nature, 451, 1082, 0801.0442

Lada, C. J., & Lada, E. A. 2003, ARA&A, 41, 57, arXiv:astro-ph/0301540

Lada, C. J., Lada, E. A., Clemens, D. P., & Bally, J. 1994, ApJ, 429, 694

Lada, C. J., Muench, A. A., Rathborne, J., Alves, J. F., & Lombardi, M. 2008, ApJ, 672, 410, arXiv:0709.1164

Lada, E. A. 1992, ApJL, 393, L25

Larson, R. B. 1969, MNRAS, 145, 271

——. 1973a, MNRAS, 161, 133

——. 1973b, ARA&A, 11, 219

——. 1978, MNRAS, 184, 69

——. 1981, MNRAS, 194, 809

——. 1992, MNRAS, 256, 641

——. 2003, Reports of Progress in Physics, 66, 1651, arXiv:astro-ph/0306595

——. 2005, MNRAS, 359, 211, arXiv:astro-ph/0412357

Lee, C. W., Myers, P. C., & Tafalla, M. 1999, ApJ, 526, 788, arXiv:astro-ph/9906468

Lilley, A. E. 1955, ApJ, 121, 559

Lombardi, M., & Alves, J. 2001, A&A, 377, 1023, arXiv:astro-ph/0109135

Lombardi, M., Alves, J., & Lada, C. J. 2006, A&A, 454, 781, arXiv:astro-ph/0606670

Longmore, S. N. 2009, in preparation

Lucy, L. B. 1977, AJ, 82, 1013

Mac Low, M.-M. 1999, ApJ, 524, 169, arXiv:astro-ph/9809177

Mac Low, M.-M., Balsara, D. S., Kim, J., & de Avillez, M. A. 2005, The Astrophysical Journal, 626, 864, arXiv:astro-ph/0410734

Mac Low, M.-M., Klessen, R. S., Burkert, A., & Smith, M. D. 1998, Physical Review Letters, 80, 2754, arXiv:astro-ph/9712013

Marseille, M., Bontemps, S., Herpin, F., van der Tak, F. F. S., & Purcell, C. R. 2008, A&A, 488, 579, 0806.1195

Masunaga, H., & Inutsuka, S.-i. 2000, ApJ, 531, 350

Mathis, J. S., Mezger, P. G., & Panagia, N. 1983, A&A, 128, 212

Matzner, C. D., & McKee, C. F. 2000, ApJ, 545, 364, arXiv:astro-ph/0007383

McKee, C. F., Storey, J. W. V., Watson, D. M., & Green, S. 1982, ApJ, 259, 647

McKee, C. F., & Tan, J. C. 2003, ApJ, 585, 850, arXiv:astro-ph/0206037

McKee, C. F., & Williams, J. P. 1997, ApJ, 476, 144

Miller, G. E., & Scalo, J. M. 1979, ApJS, 41, 513

Monaghan, J. J. 1992, ARA&A, 30, 543

Monaghan, J. J., & Gingold, R. A. 1983, Journal of Computational Physics, 52, 374

Monaghan, J. J., & Lattanzio, J. C. 1985, A&A, 149, 135

Motte, F., Andre, P., & Neri, R. 1998, A&A, 336, 150

Motte, F., Bontemps, S., Schilke, P., Schneider, N., Menten, K. M., & Broguière, D. 2007, A&A, 476, 1243, 0708.2774

Myers, P. C. 1983, ApJ, 270, 105

——. 2000, ApJL, 530, L119

——. 2008, ArXiv e-prints, 0807.1270

Myers, P. C., Fuller, G. A., Goodman, A. A., & Benson, P. J. 1991, ApJ, 376, 561

Myers, P. C., & Gammie, C. F. 1999, The Astrophysical Journal, 522, L141

Nutter, D., & Ward-Thompson, D. 2007, MNRAS, 374, 1413, arXiv:astro-ph/0611164

Ossenkopf, V., & Henning, T. 1994, A&A, 291, 943

Ostriker, E. C., Stone, J. M., & Gammie, C. F. 2001, ApJ, 546, 980, arXiv:astro-ph/0008454

Padoan, P. 1995, MNRAS, 277, 377

Padoan, P., Boldyrev, S., Langer, W., & Nordlund, Å. 2003, ApJ, 583, 308, arXiv:astro-ph/0207568

Padoan, P., Cambrésy, L., Juvela, M., Kritsuk, A., Langer, W. D., & Norman, M. L. 2006, ApJ, 649, 807, arXiv:astro-ph/0607028

Padoan, P., & Nordlund, Å. 2002, ApJ, 576, 870, arXiv:astro-ph/0011465

Padoan, P., Nordlund, A., & Jones, B. J. T. 1997, MNRAS, 288, 145

Passot, T., Pouquet, A., & Woodward, P. 1988, The Astrophysical Journal, 197, 228

Penston, M. V. 1969, MNRAS, 144, 425

Peretto, N., André, P., & Belloche, A. 2006, A&A, 445, 979, arXiv:astro-ph/0508619

Peretto, N., Hennebelle, P., & André, P. 2007, A&A, 464, 983, arXiv:astro-ph/0611277

Pillai, T., Wyrowski, F., Menten, K. M., & Krügel, E. 2006, A&A, 447, 929, arXiv:astro-ph/0510622

Pineda, J. E., Caselli, P., & Goodman, A. A. 2008, ApJ, 679, 481, 0802.0708

Pineda, J. E., Rosolowsky, E. W., & Goodman, A. A. 2009, ApJL, 699, L134, 0906.0331

Price, D. J. 2008, Journal of Computational Physics, 227, 10040, 0709.2772

Price, D. J., & Bate, M. R. 2008, MNRAS, 385, 1820, 0801.3293

Rathborne, J. M., Jackson, J. M., Chambers, E. T., Simon, R., Shipman, R., & Frieswijk, W. 2005, ApJL, 630, L181, arXiv:astro-ph/0508458

Rathborne, J. M., Jackson, J. M., & Simon, R. 2006, ApJ, 641, 389, arXiv:astro-ph/0602246

Ridge, N. A. et al. 2006, AJ, 131, 2921, arXiv:astro-ph/0602542

Roberts, W. W. 1969, The Astrophysical Journal, 158, 123

Robitaille, T. P., Whitney, B. A., Indebetouw, R., Wood, K., & Denzmore, P. 2006, ApJS, 167, 256, arXiv:astro-ph/0608234

Rosolowsky, E. W., Pineda, J. E., Kauffmann, J., & Goodman, A. A. 2008, ApJ, 679, 1338, 0802.2944

Salpeter, E. E. 1955, ApJ, 121, 161

Scalo, J., Vazquez-Semadeni, E., Chappell, D., & Passot, T. 1998, The Astrophysical Journal, 504, 835, arXiv:astro-ph/9710075

Schnee, S., Bethell, T., & Goodman, A. 2006, ApJL, 640, L47, arXiv:astro-ph/0602286

Schnee, S., Li, J., Goodman, A. A., & Sargent, A. I. 2008, ApJ, 684, 1228, 0805.4215

Shu, F. H. 1977, ApJ, 214, 488

Shu, F. H., Adams, F. C., & Lizano, S. 1987, ARA&A, 25, 23

Shu, F. H., Lizano, S., Ruden, S. P., & Najita, J. 1988, ApJL, 328, L19

Silk, J. 1985, ApJL, 292, L71

——. 1995, ApJL, 438, L41

Simon, R., Rathborne, J. M., Shah, R. Y., Jackson, J. M., & Chambers, E. T. 2006, ApJ, 653, 1325

Simpson, R. J., Nutter, D., & Ward-Thompson, D. 2008, ArXiv e-prints, 0807.4382

Smith, R. J., Clark, P. C., & Bonnell, I. A. 2008, MNRAS, 391, 1091, 0809.2702

Sridharan, T. K., Beuther, H., Schilke, P., Menten, K. M., & Wyrowski, F. 2002, ApJ, 566, 931, arXiv:astro-ph/0110363

Stamatellos, D., Whitworth, A. P., Bisbas, T., & Goodwin, S. 2007, A&A, 475, 37, 0705.0127

Stone, J. M., Ostriker, E. C., & Gammie, C. F. 1998, ApJL, 508, L99, arXiv:astro-ph/9809357

Stutzki, J., & Guesten, R. 1990, ApJ, 356, 513

Swift, J. J., & Williams, J. P. 2008, ApJ, 679, 552, 0802.2099

Tachihara, K., Onishi, T., Mizuno, A., & Fukui, Y. 2002, A&A, 385, 909

Tafalla, M., Myers, P. C., Caselli, P., & Walmsley, C. M. 2004, Astrophysics & Space Science, 292, 347, arXiv:astro-ph/0401148

Tan, J. C., Krumholz, M. R., & McKee, C. F. 2006, ApJL, 641, L121, arXiv:astro-ph/0603278

Testi, L., & Sargent, A. I. 1998, ApJL, 508, L91, arXiv:astro-ph/9809323

Tilley, D. A., & Pudritz, R. E. 2007, MNRAS, 382, 73, arXiv:astro-ph/0508562

Tobin, J. J., Hartmann, L., Furesz, G., Mateo, M., & Megeath, S. T. 2009, ApJ, 697, 1103, 0903.2775

Tohline, J. E. 1982, Fundamentals of Cosmic Physics, 8, 1

Vazquez-Semadeni, E. 1994, ApJ, 423, 681

Vazquez-Semadeni, E., & Gazol, A. 1995, A&A, 303, 204

Ward-Thompson, D., André, P., Crutcher, R., Johnstone, D., Onishi, T., & Wilson, C. 2007, in Protostars and Planets V, ed. B. Reipurth, D. Jewitt, & K. Keil, 33–46

Ward-Thompson, D., André, P., & Kirk, J. M. 2002, MNRAS, 329, 257, arXiv:astro-ph/0109173

Ward-Thompson, D., Scott, P. F., Hills, R. E., & Andre, P. 1994, MNRAS, 268, 276

Whitworth, A. P., & Ward-Thompson, D. 2001, ApJ, 547, 317, arXiv:astro-ph/0009325

Wilcox, D. C. 1998, Turbulence Modeling for CFD, 2nd Edition (DCW Industries, 1998)

Williams, J. P., Blitz, L., & McKee, C. F. 2000, Protostars and Planets IV, 97, arXiv:astro-ph/9902246

Williams, J. P., de Geus, E. J., & Blitz, L. 1994, ApJ, 428, 693

Williams, S. J., Fuller, G. A., & Sridharan, T. K. 2004, A&A, 417, 115, arXiv:astro-ph/0401633

Young, C. H., Shirley, Y. L., Evans, II, N. J., & Rawlings, J. M. C. 2003, ApJS, 145, 111, arXiv:astro-ph/0210182

Zhang, Q., Wang, Y., Pillai, T., & Rathborne, J. 2009, ApJ, 696, 268, 0902.0647

Zinnecker, H. 1982, New York Academy Sciences Annals, 395, 226

Zuckerman, B., & Evans, II, N. J. 1974, ApJL, 192, L149